SEARCH FOR DARK MATTER PRODUCED IN ASSOCIATION WITH A HIGGS BOSON DECAYING TO TWO PHOTONS IN PROTON-PROTON COLLISIONS AT 13 TEV WITH THE CMS DETECTOR

A Dissertation

Presented to the Faculty of the Graduate School

of Cornell University

in Partial Fulfillment of the Requirements for the Degree of

Doctor of Philosophy

by

Margaret Eldridge Zientek

May 2019

SEARCH FOR DARK MATTER PRODUCED IN ASSOCIATION WITH A HIGGS BOSON DECAYING TO TWO PHOTONS IN PROTON-PROTON COLLISIONS AT 13 TEV WITH THE CMS DETECTOR

Margaret Eldridge Zientek, Ph.D.

Cornell University 2019

Results are presented from a search for dark matter particles produced in association with a Higgs boson decaying to two photons in proton-proton collision data collected at a center-of-mass energy of 13 TeV. The search is based on data collected in 2015 and 2016 by the CMS experiment at the CERN Large Hadron Collider. The analyzed data correspond to an integrated luminosity of 2.2 fb^{-1} and 35.9 fb^{-1}, respectively. No significant excess over the standard model background expectation is observed. The results are used to constrain at the 95% confidence level dark matter production cross section in the context of two simplified models. A Z′ mediator in a Z′-two-Higgs-doublet model with mass between 550 and 860 GeV is excluded for dark matter masses below 100 GeV. Additionally, in a baryonic Z′ model, Z′ masses below 574 GeV are excluded, for a dark matter mass of 1 GeV.

The thesis also explores some of the challenges associated with the upgraded High-Luminosity Large Hadron Collider. One important challenge will be integrating real-time charged particle track finding and reconstruction into a hardware data selection system. A proposed FPGA-based solution that reconstructs tracks within 4 μs is discussed.

BIOGRAPHICAL SKETCH

Margaret Zientek was born in Seattle, Washington. She moved with her family to New Jersey when she was 10 years old. Margaret got interested in physics in high school, even coming in early in the morning to go over additional physics material with her teacher. She graduated from Howell High School in Farmingdale, New Jersey in June 2009.

Margaret started her undergraduate studies at Rutgers University in New Brunswick, New Jersey in September 2009. She worked with Professor John Paul Chou as an undergraduate researcher on the Compact Muon Solenoid (CMS) experiment and spent her free time playing ultimate frisbee. Margaret completed her Bachelor of Science in physics in May 2013.

Margaret has been a graduate student in physics at Cornell University in Ithaca, New York since August 2013. She has been working with Professor Peter Wittich and conducting research with the CMS experiment at the Large Hadron Collider (LHC) at the European Organization for Nuclear Research (CERN) in Geneva, Switzerland. Margaret was based at CERN from 2015 until 2018 where she was involved in the operation of the silicon tracker detector and alpine skiing. Margaret received a Master of Science in physics from Cornell University in May 2016. She defended her doctoral thesis in March 2019 and will graduate with her doctoral degree from Cornell University in May 2019.

To my family and friends
who fill my life with joy,
love, and quarkiness.

ACKNOWLEDGEMENTS

First, I would like to thank my advisor, Peter Wittich, for his guidance throughout my time at Cornell. I have truly enjoyed working with and learning from you. Through countless discussions, I have learned what questions are important and become a better physicist. Thank you for all of the advice and support over the years.

I would also like to thank postdoc Livia Soffi for being a great mentor and teammate on the Mono-h analysis. Thank you for teaching me how to do an analysis and your dedication to this search. Thank you to my colleagues on the various Mono-h searches who shared interesting discussions on these dark matter signatures. Thanks to Chiara Rovelli and Chiara Amendola for their work in our first iteration of this analysis. Also, thank you to the CMS teams working on the search for the standard model Higgs decaying to two photons and the high mass diphoton search for useful software, tools, and feedback.

The tracklet project is possible because of the work of a small group of physicists and engineers. I want to thank all of my collaborators at Cornell, Rutgers, Ohio State, Notre Dame, Colorado State, and Northwestern Universities. I would especially like to thank Professor Anders Ryd and postdoc Louise Skinnari who are great sources of knowledge regarding the tracklet algorithm. Thanks to engineer Charlie Strohman who developed the YUGE board and has provided extensive insight into writing FPGA firmware. And thanks to my fellow graduate students on the project who have put in the leg work to get the firmware running, especially Jorge Chaves and Zhengcheng Tao.

I have genuinely enjoyed being part of the Cornell CMS group and would like to thank my friends and colleagues in the group. I appreciate the friendly environment which has fostered exciting research. Thank you especially to my

fellow graduate students Abhisek Datta, Andre Sterenberg Frankenthal, Dan Quack, Derek Cranshaw, Divya Gadkari, Jennifer Chu, Jorge Chaves, Kevin McDermott, Nathan Mirman, Shao Min Tan, Shaun Hogan, Susan Dittmer, Tres Reid, and Zhengcheng Tao. I have had many fun times at Cornell and CERN with all of you over the last six years.

I would like to thank the Cornell physics department for providing a supportive place for research and study. I want to acknowledge my colleagues in the CERN accelerator department for the excellent performance of the LHC, and the entire CMS Collaboration for the success of the CMS physics program. A special thanks to the conveners and committees who thoroughly critiqued and reviewed my work over the years. And thanks to my committee, Professors Peter Wittich, Julia Thom-Levy, and Yuval Grossman, for reviewing this thesis.

I would also like to thank my family because without their love and support I would not be here. My parents, Susie and Jan, deserve tremendous credit for developing my curiosity and love of learning. Thank you for all of the immeasurable things you have done to get me to this point. My brother, Joe, thank you for always bringing joy to the world. You have been a wonderful friend my whole life. Thank you to my biggest cheer leaders, my grandparents, Joe and Ellen, who were always excited to hear about my adventures. And thank you to all of my friends who make my life happier.

Lastly, I would like to thank Kevin McDermott. Sharing this experience with you has been an incredible journey. Your science enthusiasm is irresistible and I appreciate all that I have learned from you. Your friendship, love, and support over the last six years have defined my graduate school experience.

This work has been supported by the National Science Foundation.

TABLE OF CONTENTS

LIST OF TABLES

LIST OF FIGURES

CHAPTER 1

INTRODUCTION

The goal of particle physics is to understand the fundamental building blocks of matter and their interactions. These interactions, in turn, provide clues as to how the universe formed. The standard model (SM) of particle physics is an extensive theory which has been remarkably successful in describing the interactions of the elementary particles. It is a model that has been well-tested through various experiments over the last few decades. In fact, there is excellent agreement between the predictions of the SM and the observed values [1]. For example, the SM predicted the existence of the W, Z, and Higgs bosons and the top quark. Furthermore, numerous properties observed for these particles, including the Higgs boson cross section and branching fractions, are accurately predicted by the SM.

To study the smallest pieces of matter, particle physicists try to convert energy into new massive particles. To do this, particles are accelerated and then collided. This has historically been an extremely successful method of probing the SM, and has provided a lot of information over the last few decades about fundamental particles. This method of probing particles has also been fruitful at the CERN Large Hadron Collider (LHC). In 2012 at the LHC, the SM was completed with the discovery of the Higgs boson by both the ATLAS and CMS Collaborations [2, 3]. This discovery has offered a new probe of the SM and beyond the SM theories.

There are still several questions in particle physics that remain unanswered within the SM framework. These questions span from how to include the gravitational force in the framework, to why is there a large matter-antimatter asym-

metry in the universe, to how do neutrinos have mass. The particle composition of dark matter (DM) is another mystery. Astrophysical evidence has strongly suggested the existence of DM in the universe. However, any particle nature of DM is not predicted by the SM and remains completely unknown.

Several beyond the SM theories predict DM particles that interact with SM particles. One way to look for DM-SM particle interactions is at collider experiments by looking for events (particle collisions) where SM and DM particles are produced and recoil away from each other. Since any DM produced at the LHC is unlikely to interact with the detector, these recoiling events are characterized by large imbalances in the recorded momentum transverse, or perpendicular, to the beam. In effect, there is a large amount of missing transverse momentum ($\vec{p}_{\mathrm{T}}^{\,\mathrm{miss}}$) nearly back-to-back with a SM particle. The signature exploited in this thesis, are events where DM is produced in association with a Higgs boson. More specifically, the case where the Higgs boson decays to two photons is examined.

This thesis will explore the details of this search, starting with the theoretical models that motivate the search. Next the apparatus for generating and collecting data, the LHC accelerator and the CMS detector, respectively, will be described. The reconstruction of various physics objects that are used in the analysis will be presented. Given next are the specifics of the event selection and background estimation. This will include a discussion of the statistical treatment of the data and the systematic uncertainties affecting the analysis. Finally, the results will be presented along with their interpretation in the context of two benchmark signal models.

The LHC, which is currently operating at a center-of-mass energy $\sqrt{\mathrm{s}}$ of

13 TeV, will continue running for many years. Various upgrades are planned over the next decade to ensure that CERN will further expand its physics reach. In 2025, the LHC will begin its next phase, the High-Luminosity LHC (HL-LHC). Because of the increase in the peak luminosity to be delivered by the HL-LHC, the CMS detector will be subjected to a greater number of simultaneous proton-proton interactions (pileup). To deal with the many challenges that are associated with high pileup, the CMS detector will undergo "Phase II" upgrades. In addition to the above mentioned dark matter search, this thesis will also explore several developments related to these upgrades.

Of particular interest are the changes to the hardware trigger (data selection) system. For the first time, this trigger will include charged particle track reconstruction. This provides an important new handle for selecting interesting physics events in this intense environment. In order to make tracks out of detector hits within the $4\,\mu$s latency budget, CMS will use field-programmable gate array (FPGA) technology which can preform calculations at speeds of roughly 300 MHz. The tracklet algorithm is a proposed FPGA-based approach to charged particle track reconstruction for the trigger which will be described in more detail in a later chapter.

CHAPTER 2

THEORETICAL MOTIVATION

In this Chapter, an overview of the standard model (SM) is presented in Section 2.1 while Section 2.2 introduces the necessity of the Higgs boson in the SM. These sections are based on the introduction to the SM from Ref. [4]. Section 2.3 presents the astrophysical evidence for dark matter and Section 2.4 offers an overview of how the Higgs boson can be used to search for dark matter particles. Finally, the signal models directly explored in this thesis are presented in Section 2.5.

2.1 Standard model

The standard model of particle physics is a description of nature which summarizes the current best understanding of the fundamental structure of matter. It describes the elementary particles (summarized in Fig. 2.1) and the strong and electroweak forces that govern their interactions. The standard model Lagrangian contains information about the kinetic energy, mass and interaction potentials of each of the particles in the model.

The SM Lagrangian is built [4] as the most general Lagrangian constructed from the gauge symmetries of the strong, weak, and electromagnetic forces and the irreducible representation of the particles in these groups. Starting with the free field Lagrangian densities $\mathcal{L}$ and the chosen group, the original $\mathcal{L}$ contains all possible fields and interactions that are invariant under the gauge symmetry of the group. This symmetry implies that there are conserved quantum numbers in each particle interaction. The resulting Lagrangian describes the allowed

particle interactions in the SM. The gauge group of the SM is a local

$$SU(3)_C \times SU(2)_L \times U(1)_Y, \tag{2.1}$$

which is the product of the strong force symmetry group $SU(3)_C$ and the $SU(2)_L \times U(1)_Y$ symmetry group of the unified electromagnetic and weak forces. The subscripts C, L, and Y are used here simply to denote color, left handedness, and hypercharge, respectively. These are conserved quantum numbers in the SM.

The quantum chromodynamic (QCD) portion of the SM Lagrangian describes the strong force. The $\mathcal{L}$ is constructed from the free particle fields for the six quarks, each with three color charges. To enforce a local $SU(3)$ symmetry invariance, eight $G^a_\mu,\ a = 1...8$ gauge fields (gluons) are introduced into the Lagrangian. Gluons are massless and electrically neutral, but carry a color quantum number and therefore interact with themselves. The resulting gauge invariant $\mathcal{L}$ contains the quark propagator, the quark-gluon interaction potentials, and the gluon self-interaction potential.

The electroweak Lagrangian is extracted in a similar way. The fermion part of the SM involves three generations of quarks and leptons, each consisting of left-handed doublets and right-handed singlets under $SU(2)$. The $\mathcal{L}$ of the fermion free fields is required to be symmetric under $SU(2) \times U(1)$. Three gauge fields $W^a_\mu,\ a = 1...3$ and an additional gauge field B_μ are introduced for the $SU(2)$ and $U(1)$ groups, respectively. After extracting the final gauge invariant Lagrangian, the photon, $W^{\pm}$, and Z bosons are interpreted as different linear combinations of W^a_μ and B_μ.

If the SM symmetry was unbroken, all of the gauge fields mentioned above would have to be massless. Mass terms in the Lagrangian are not invariant

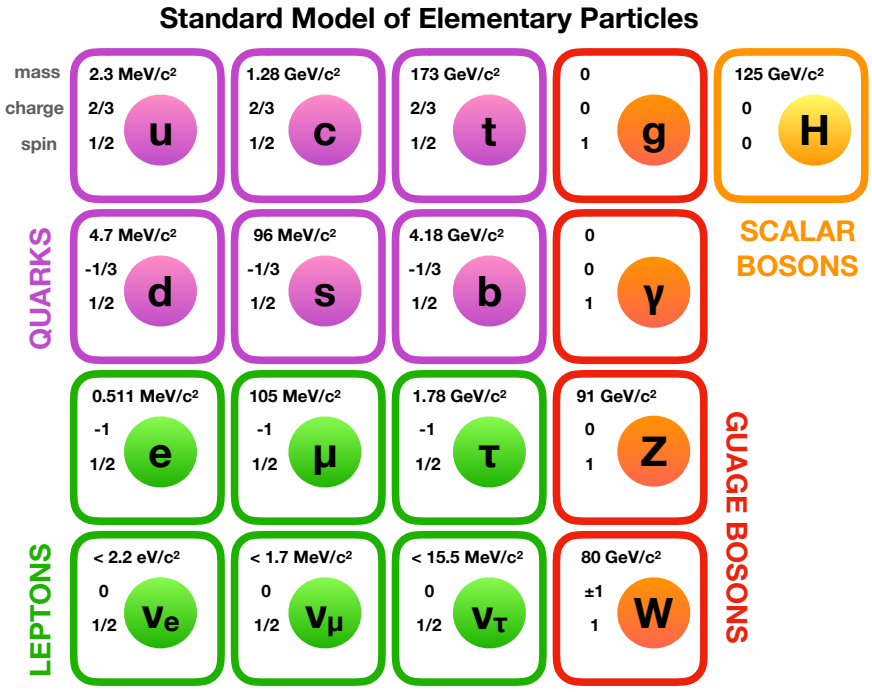

Figure 2.1: Particle constituents of the standard model.

under the transformations of each group and therefore do not maintain their respective group's symmetry. However, while the photon and gluons are massless, experimentally it is known that the $W^{\pm}$ and Z bosons, carriers of the weak force, have masses of approximately 80 and 91 GeV, respectively [1]. One theoretical explanation that introduces mass terms in the SM is spontaneous electroweak symmetry breaking (SSB). The details of SSB and the Higgs mechanism are described in the following section.

2.2 Higgs mechanism

The addition of bare mass terms in the Lagrangian mentioned above explicitly breaks the symmetry in the equations of motion themselves. Instead, the sym-

metries can be spontaneously broken in the ground state. In the Higgs mechanism, the addition of a complex scalar $SU(2)$ doublet ϕ to the SM enables SSB in this way and enables mass terms in the SM Lagrangian.

For the Higgs doublet ϕ:

$$\phi = \begin{pmatrix} \phi^+ \\ \phi^0 \end{pmatrix} = \frac{1}{\sqrt{2}} \begin{pmatrix} \phi_1 + i\phi_2 \\ \phi_3 + i\phi_4 \end{pmatrix} \tag{2.2}$$

the Lagrangian density of the new scalar field is:

$$\mathcal{L} = (D^\mu \phi)^\dagger D_\mu \phi - V(\phi), \tag{2.3}$$

where the gauge covariant derivative $D_\mu \phi$ is:

$$D_\mu \phi = \big(\partial_\mu + \frac{ig}{2}\vec{\sigma} \cdot \vec{W}_\mu + \frac{ig'}{2}\vec{B}_\mu\big)\phi \tag{2.4}$$

where g and g' are coupling constants and $\vec{\sigma}$ are the Pauli matrices.

The vacuum expectation value of the ϕ field is the solution to the equations of motion with the least energy. This ground state of ϕ (defined in Eq. 2.2) can be chosen along a convenient axis so that only ϕ_3 is nonzero:

$$\mathrm{v} \equiv \langle 0|\phi|0\rangle = \frac{1}{\sqrt{2}} \begin{pmatrix} 0 \\ \nu \end{pmatrix}. \tag{2.5}$$

In this axis, the potential of ϕ can be expressed as:

$$V(\phi) \to V(\mathrm{v}) = \frac{1}{2}\mu^2\nu^2 + \frac{1}{4}\lambda\nu^4. \tag{2.6}$$

The potential must be minimized with respect to ν to extract the ground state. If $\mu^2 > 0$, the minimum is found at $\nu = 0$ which does not break the $SU(2) \times U(1)$ symmetry. For the case of $\mu^2 < 0$, the potential $V(\phi)$, which is sketched in Fig. 2.2, has a circle of degenerate minima at a radius of $\nu = \sqrt{-\mu^2/\lambda}$. The

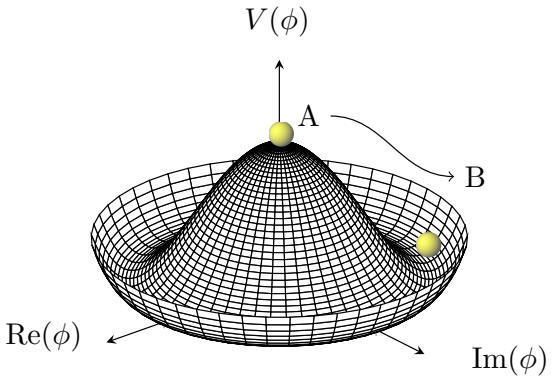

Figure 2.2: Sketch of the Higgs potential field.

ground state is a random point along this circle, thus spontaneously breaking the $SU(2) \times U(1)$ symmetry.

A consequence of SSB is the generation of massless spin-0 particles called Goldstone bosons. However, these extra degrees of freedom can be absorbed as mass terms for the W and Z boson. To see this, it is useful to work in the unitary gauge where the physical particle content is manifest. Let ϕ be:

$$\phi = \frac{1}{\sqrt{2}} \begin{pmatrix} 0 \\ \nu + \mathrm{h} \end{pmatrix} \tag{2.7}$$

where h is the physical Higgs boson. In this case, from Eq. 2.4, one obtains the terms:

$$\frac{g^2\nu^2}{4}\mathrm{W}^{+\mu}\mathrm{W}^{-}_{\mu} + \frac{1}{2}(g^2 + g'^2)\frac{\nu^2}{4}\mathrm{Z}^{\mu}\mathrm{Z}_{\mu}, \tag{2.8}$$

where linear combinations of W^a_μ and B_μ are used to define $\mathrm{W}^{\pm}$ and Z. The terms above are the mass terms in SM for the W and Z bosons. The combination of W^a_μ and B_μ orthogonal to the Z is the photon, and it remains massless. The additional terms from Eq. 2.3 contain the Higgs field kinetic energy term,

Higgs interaction terms (including self-interactions and those with the W and Z bosons) and a mass $m_{\mathrm{h}} = \sqrt{-2\mu^2} = \sqrt{2\lambda}\nu$ term for the Higgs boson.

Lepton and quark masses are generated in a similar way. Terms that involve the interaction of these fermions with the scalar Higgs field are included in the Lagrangian so long as they continue to obey the required symmetry relations. Using the same ground state chosen in Eq. 2.7, the Lagrangian after SSB has mass terms for the fermions that are proportional to ν along with fermion-Higgs boson interaction terms that are proportional to the fermion's mass.

From all of this, it is seen that the Higgs mechanism is the ingredient in the SM that gives all other particles mass. However, there was no experimental evidence for the existence of a scalar particle and therefore no evidence of the Higgs mechanism. The Higgs boson remained an elusive missing piece of the SM for over 40 years. The lack of observation of this important particle, was one of the motivations for building the LHC. And in July 2012, the discovery of the Higgs boson was finally announced.

The Higgs boson was observed by both the ATLAS and CMS Collaborations by its decay to several different SM particles [2, 3]. CMS alone observed an excess of events at a mass of 125 GeV with a statistical significance of greater than five standard deviations above the background expectation. The probability that the background-only hypothesis would fluctuate and yield this distribution is less than one in three million.

To achieve this discovery, searches for the Higgs boson were performed in the $\mathrm{h} \to \gamma\gamma$, $\mathrm{h} \to \mathrm{ZZ}$, $\mathrm{h} \to \mathrm{WW}$, $\mathrm{h} \to \mathrm{b\overline{b}}$, and $\mathrm{h} \to \tau\tau$ decay channels. The branching fraction, or the probability for the Higgs boson to decay via each of

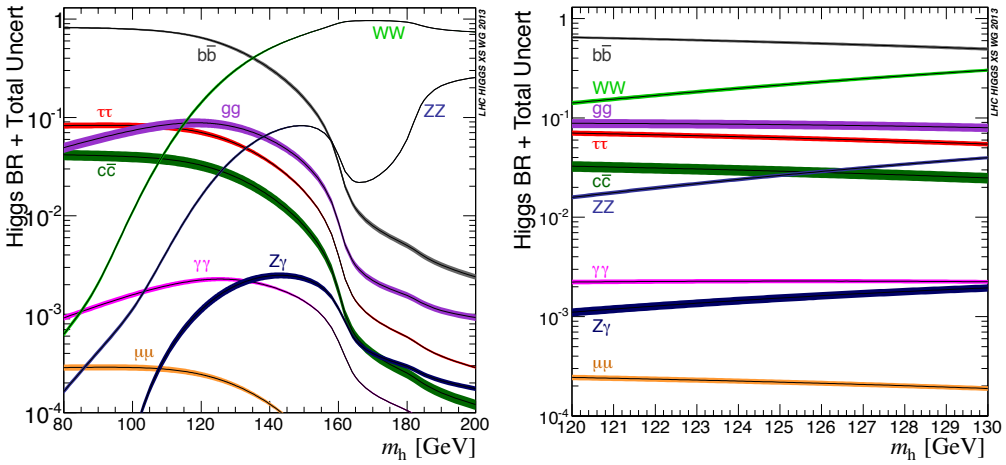

Figure 2.3: SM Higgs boson branching fractions as a function of mass for a large mass range (left) and near $m_{\mathrm{h}} = 125\ \mathrm{GeV}$ (right) [5].

these channels, is computed in the SM. The predicted SM branching fractions for the Higgs boson are shown in Fig. 2.3. It is seen here that the decay $\mathrm{h} \to \mathrm{b\bar{b}}$ is the most likely at $m_{\mathrm{h}} = 125\ \mathrm{GeV}$. However, the $\mathrm{h} \to \mathrm{b\bar{b}}$ channel has a much worse mass resolution and larger background than the $\mathrm{h} \to \gamma\gamma$ and $\mathrm{h} \to \mathrm{ZZ}$ channels. In actuality, the $\mathrm{h} \to \gamma\gamma$ and $\mathrm{h} \to \mathrm{ZZ}$ channels were the main discovery channels in the observation of the Higgs boson.

The excess of events in the CMS $\mathrm{h} \to \gamma\gamma$ analysis is visible in the diphoton invariant mass of 10.4 fb^{-1} of data as shown in Fig. 2.4. The $\mathrm{h} \to \gamma\gamma$ channel is uniquely important because based on spin conservation, a new particle that decays to two photons must be a boson but cannot have spin-1. This suggests that the observed particle is in fact a scalar boson and the SM Higgs boson.

From the high mass resolution of the $\mathrm{h} \to \gamma\gamma$ and $\mathrm{h} \to \mathrm{ZZ}$ channels, the CMS experiment was able to measure the mass of the Higgs boson and compare the signal strength with SM expectations. The current best estimate of the Higgs boson mass is $125.09 \pm 0.24\ \mathrm{GeV}$ and the observed signal strength (the ratio of

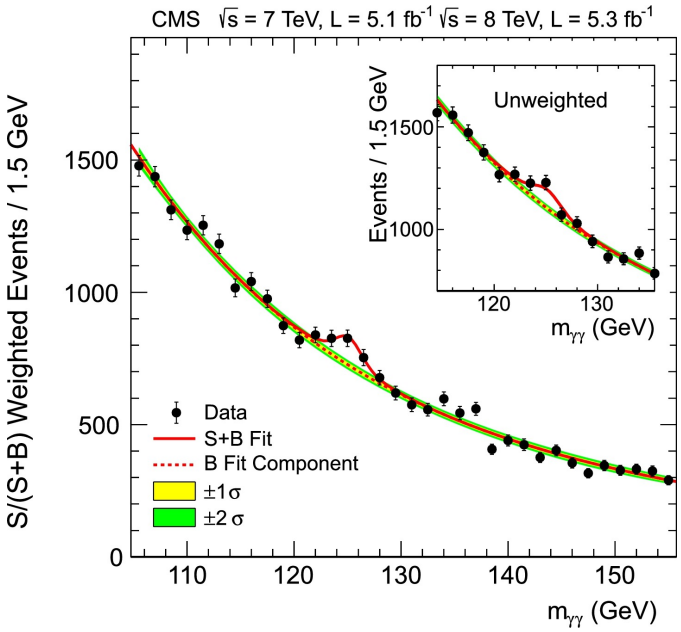

Figure 2.4: Higgs boson observation at CMS in the $\mathrm{h} \to \gamma\gamma$ channel [3].

observed cross section to SM predicted cross section) is 1.10 ± 0.11 [1].

The discovery of the Higgs boson offers new ways to examine the SM. Precise measurements of the Higgs boson production cross section and branching fractions will test the extent of standard model's compatibility with the behavior of the Higgs boson observed in nature. However, there are also many open questions in particle physics that are not contained within the SM framework. As mentioned earlier, dark matter is one of these mysteries. Any particle nature of DM is not described in the SM and remains completely unknown experimentally. The next few sections will detail more about what is known and unknown about dark matter and how the discovery of the Higgs boson opens up new search regimes for particle dark matter.

2.3 Dark matter

There is a large amount of astrophysical evidence of the existence of dark matter in the universe, only a fraction of which will be touched on here. Whether DM has particle origin remains a mystery. There are a number of well-motivated theories beyond the SM that predict the existence of a DM particle. A review of particle dark matter is presented in Ref. [6].

Some of the most convincing evidence of DM comes from galaxy-scale cosmological observations. From the light emitted from galaxies, astronomers can estimate the density of visible mass which seems to be clustered mainly at the center of the galaxy. Astronomers examine rotation curves: the circular velocity of the galaxy as a function of distance r from its center. From Newtonian dynamics, the velocity should be proportional to $\sqrt{m(r)/r}$ where $m(r)$ is the integrated density. Thus it is expected that further away from the galactic center, where the mass drops to zero, the velocity would decrease as a function of $1/\sqrt{r}$. However, the measured velocities are roughly constant across the entire galaxy, as seen in Fig. 2.5. By assuming there is some heavy non-luminous (dark) matter that is roughly constant in the galactic halo, the predicted shape recovers the observed rotation curve.

Gravitational lensing of colliding galaxies provides additional evidence of dark matter. Gravitational lensing is a property of general relativity in which light rays from a distant object are deflected along the path to the observer by the gravitational field from a closer object, thus distorting the appearance of the far-field object. In the colliding galaxies of the Bullet Cluster, the stars mostly traveled through each other. The gasses of the system interacted, emitting a

large amount of x-rays, and suggesting that the majority of the baryonic matter was slowed down with respect to the stars. However, the gravitation lensing of galaxies behind these clusters show that the majority of the mass behaves as if it has passed through without interacting [7]. This suggests the presence of dark matter that pulls the mass distribution away from the visible collision center.

The cosmological scale also provides strong evidence of dark matter [8]. In the early universe, initial gravitational fluctuations gave rise to overdensities of baryonic matter and dark matter. Radiation pressure from photons pushed back on these overdensities of baryonic matter only, while the dark matter continued to clump. This pull and push from gravity and pressure effectively created a damped harmonic oscillator for the baryonic matter. These early baryonic acoustic oscillations can be measured in the cosmic microwave background (CMB). The CMB is the relic radiation of the recombination epoch, the point when photons could escape the dense plasma because the free protons and electrons first combined to form translucent hydrogen gas. The CMB photons have been propagating since then. The power spectrum, built from a spherical harmonic decomposition, characterizes the size of fluctuations in the CMB as a function of angular scale. This is used to estimate the baryonic and non-baryonic mass density of the universe. The Planck Collaboration has done extremely precise measures of the CMB and shown that dark matter is six times more abundant that baryonic matter in the universe [9].

There are a plethora of particle DM models that have been put forth to explain the differences in observed and expected mass in the universe. The amount of luminous matter in the universe is well measured, so DM particles must be electrically neutral so that the do not interact with photons. DM can at

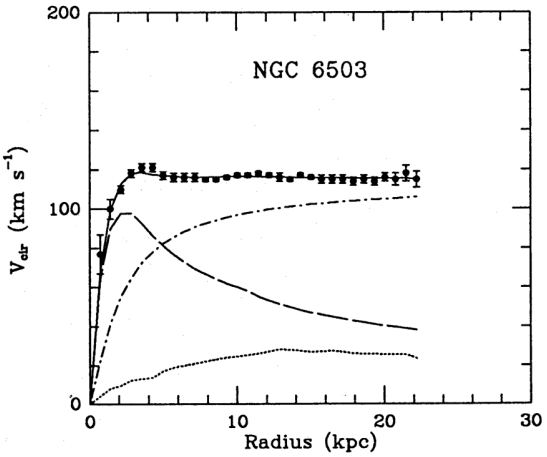

Figure 2.5: Fit (solid curve) to observed (points) rotation curve of the NGC 6503 galaxy. The fit includes the contributions from: visible components (dashed), gas (dotted), and a hypothetical dark-halo (dash-dot curve) [10].

most weakly interact with SM particles to avoid constraints from collider and DM searches. SM neutrinos, which are neutral and weakly-interacting, are too light to recover all cosmological DM observations. One class of DM particle theories that encompasses all of these constraints is that of weakly-interacting massive particles (WIMPs). To explain the expected abundance of dark matter in the universe, it is hypothesized that there are massive DM particles that interact very weakly with ordinary SM particles.

WIMPs are a current leading candidate for particle dark matter because of the so-called WIMP miracle [11]. If a dark matter particle χ exists, it would have existed in thermal equilibrium and in abundance in the early universe. The equilibrium abundance was maintained by equal rates of creation ($l\bar{l} \rightarrow \chi\bar{\chi}$) and annihilation ($\chi\bar{\chi} \rightarrow l\bar{l}$). As the universe cooled to the point where the temperature was below the dark matter mass, the creation rate of DM dropped. The DM abundance continued to annihilate and the relative abundance dropped exponentially until the annihilation rate dropped below the expansion rate. At that point, DM annihilation happened too infrequently, and the total num-

ber of DM particles was essentially frozen. This relic density [1] is relatively constant from that point to the current universe. From the Boltzmann equation, the relic density is given by $\Omega_\chi h^2 = 3 \times 10^{-27}\,\mathrm{cm}^3\,\mathrm{s}^{-1}\langle\sigma\nu\rangle^{-1}$, where $\langle\sigma\nu\rangle$ is the DM annihilation cross section [11]. Independent from this, the annihilation cross section of a hypothetical weak-scale particle can be estimated as $\langle\sigma\nu\rangle \approx \alpha^2(100\ \mathrm{GeV})^{-2} \approx 10^{-25}\,\mathrm{cm}^3\,\mathrm{s}^{-1}$ where α is the fine structure constant. The WIMP miracle is the remarkable realization that a new weak-scale particle (of mass $\approx 100\ \mathrm{GeV}$) has the right annihilation cross section to account for the observed dark matter abundance in the universe $\Omega_\chi h^2 = 0.120 \pm 0.001$ from Planck measurements [9].

Searches for DM particles have been carried out with direct and indirect detection experiments and at particle colliders, like the LHC. Each of these experiments hopes to observe the DM-SM particle interaction, illustrated in Fig. 2.6, in a different way. Direct detection experiments look for scattering of DM and SM particles. Indirect detection experiments look for DM annihilation to SM particles. Collider searches look for production of DM particles from SM particle collisions.

Direct detection experiments aim to observe scattering of DM particles with atomic nuclei on Earth [8]. The DM particles from the galactic halo will bump into the nuclei causing a momentum transfer that can be detected by these experiments. A DM-nucleon interaction may be as rare as a few per year per thousands of kilograms of target material. Therefore, typically large cavities filled with tons of heavy target material, like xenon or argon, are needed to have any chance of observing these interactions. Also, these detectors need to

[1] The relic density is the ratio of the density of DM particles in the universe to the critical density. The critical density is the average density of matter required to just halt the expansion of the universe (ie. a flat universe).

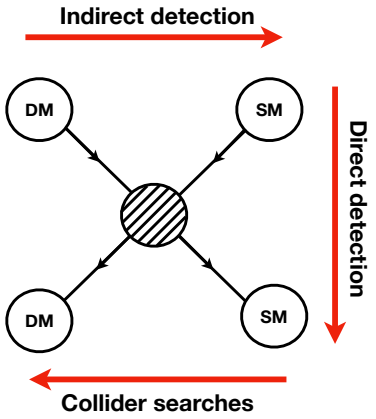

Figure 2.6: Schematic of the effective SM-DM interaction probed by direct detection, indirect detection, and collider searches. The red arrows indicate the direction of time in each type of search.

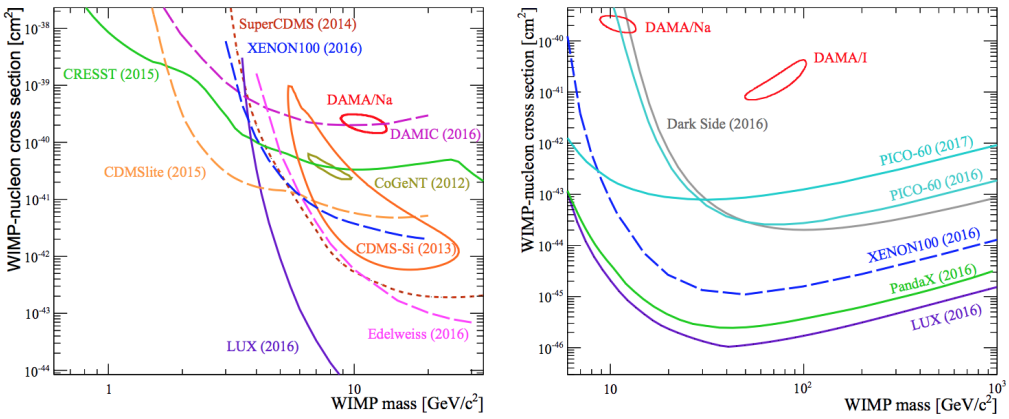

Figure 2.7: The observed (solid) or expected (dashed) exclusion limits from several direct detection experiments on DM-nucleon scattering cross section as a function of m_{DM} [12] for the low mass (left) and high mass (right) regimes. Possible signal regions observed in several experiments are shown as circular contours.

be built with low radioactive materials and placed underground to bring background radiation levels down enough to observe any signal events. The latest direct detection experiment results have constrained the DM-nucleon scattering cross section for many different dark matter masses, as shown in Fig. 2.7.

Indirect detection experiments rely on detecting SM particles that were cre-

ated by DM annihilation or decays in the sky. Neutral signals (like gamma rays) from these events travel in a roughly straight path, and can be detected by ground or space-based telescopes. The gamma ray flux data can be used to set limits on the annihilation cross section, by using the line-of-sight integral of the density through the DM distribution. Challenges arise in interpreting the data, since all astrophysical background sources must be taken into account correctly [8].

In collider experiment searches for dark matter, SM particles are smashed together with the hopes that the energy of the collision will be converted into the production of massive new particles. These new particles could be DM or mediators of DM-SM interactions. If the mediator of these interactions is produced, it can decay either to DM or back to SM particles. The latter case would produce a new resonance in the dijet or dilepton spectrum. In this way, resonant searches have excluded large swatches of particle DM parameter space [13–15]. In the case where the mediator decays to DM, since DM is weakly-interacting, it is likely to escape the detector. If the DM is produced with some SM particles, the DM will leave an imbalance in the recorded momentum of the SM particles in the collision (registered as $p_{\mathrm{T}}^{\mathrm{miss}}$). These "Mono-X" searches for a SM particle (X) plus $p_{\mathrm{T}}^{\mathrm{miss}}$ offer a more direct search for DM production at colliders. In an example simplified model [16, 17], the SM is extended by an additional $U(1)$ gauge symmetry under which candidate Dirac fermion DM particles are charged. A vector mediator facilitates an s-channel production of DM that is searched for in various resonant and Mono-X searches. A summary of the CMS and ATLAS exclusions for this model are shown in Fig. 2.8. With the discovery of the Higgs boson, Mono-h searches offer a new probe of DM, detailed in the following section.

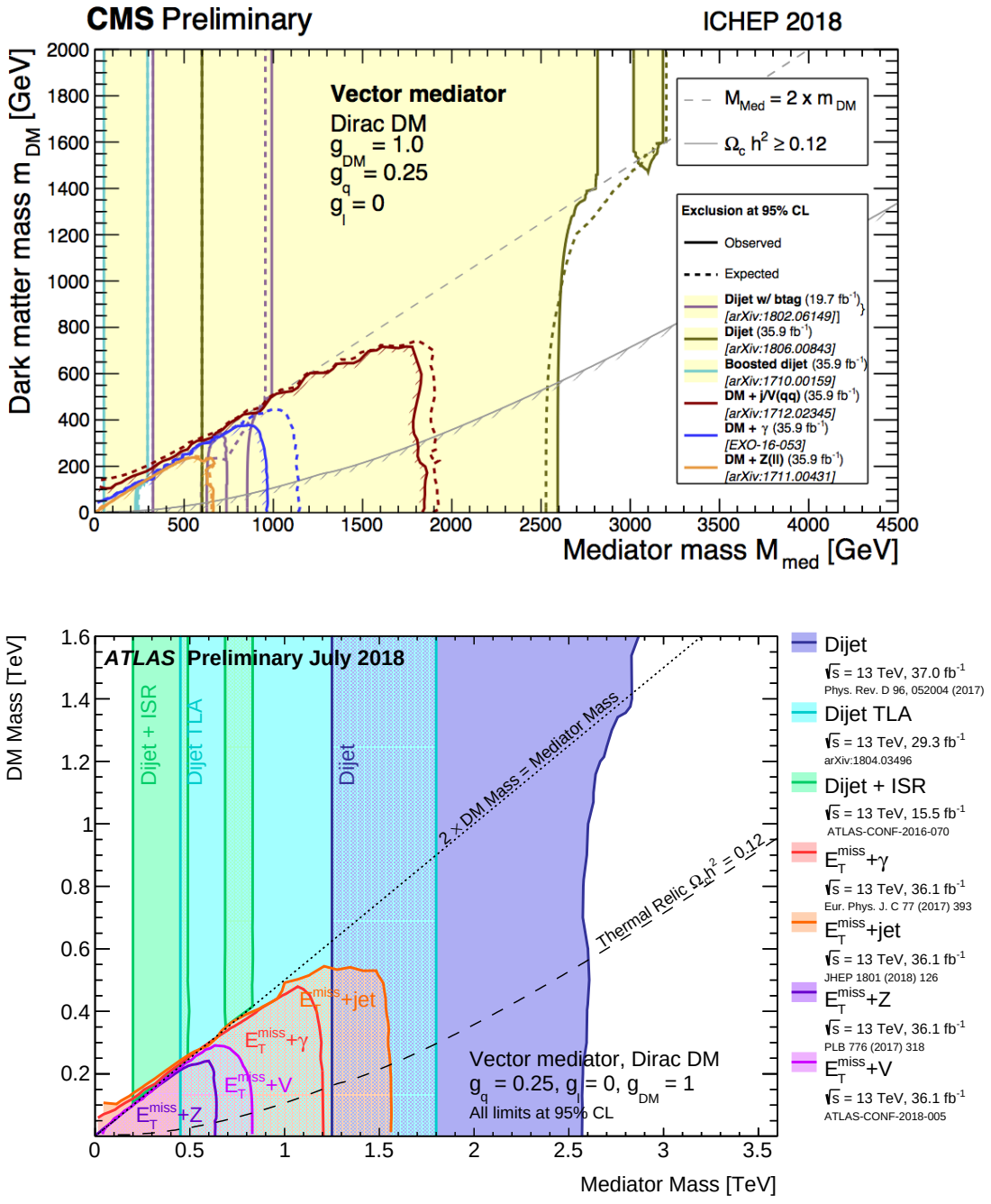

Figure 2.8: Exclusion limits at 95% confidence level of a vector mediator simplified model of Dirac DM production as a function of DM and mediator mass by CMS (upper) and ATLAS (lower) [13, 14].

2.4 Mono-h searches

As mentioned in the Section 2.3, to date only gravitational interactions have been observed between DM and SM particles. The Higgs boson, described in Section 2.2, interacts with massive SM particles with couplings proportional to their mass. It is possible that there could be a new DM-SM interaction that occurs via the Higgs boson. This makes searching for DM particles using the newly discovered Higgs boson particularly enticing [18–20].

Searches for Higgs bosons decaying to invisible particles, i.e. $\mathrm{h} \to p_{\mathrm{T}}^{\mathrm{miss}}$, have put tight constraints on DM particles with masses less than about $m_{\mathrm{h}}/2 \approx 60\ \mathrm{GeV}$ [21, 22]. However, this is not the only way that a Higgs boson could interact with DM particles. A DM particle could be produced in association with a Higgs boson. The Higgs boson could be produced in initial- or final-state radiation in an event where DM is also produced. However, initial-state radiation of an SM-like Higgs boson from a quark or gluon is suppressed by Yukawa or loop processes, respectively [18–20]. Therefore, the associated production of DM and a Higgs boson could arise from a new interaction between DM and SM particles.

The signature of a Higgs boson recoiling off of invisible particles has been explored by both ATLAS and CMS using several different Higgs boson decay channels. There are advantages and disadvantages to each channel, so it is useful to analyze the data in terms of all of these modes. The $\mathrm{h} \to \mathrm{b\bar{b}}$ channel, because it has the largest Higgs boson branching fraction (shown earlier in Fig. 2.3) offers the largest statistical power for these searches. However, this channel suffers from large multijet backgrounds and low mass resolution. To deal with the

large background rates, the $\mathrm{h} \rightarrow \mathrm{b\bar{b}}$ channel generally requires triggering on events with high $p_{\mathrm{T}}^{\mathrm{miss}}$. On the other hand, the $\mathrm{h} \rightarrow \gamma\gamma$ channel, which is a much more unlikely Higgs boson decay mode (happening only 0.2% of the time), offers smaller backgrounds and a more precise measurement of invariant mass. This channel does not need a minimum $p_{\mathrm{T}}^{\mathrm{miss}}$ threshold for triggering and is therefore complementary to searches for DM with the larger Higgs boson decay channels.

Both ATLAS and CMS Collaborations have completed several searches for DM particles produced in association with a Higgs boson. At both $\sqrt{\mathrm{s}} = 8\ \mathrm{TeV}$ and $\sqrt{\mathrm{s}} = 13\ \mathrm{TeV}$, no significant excesses have been observed by either experiment in the $\mathrm{h} \rightarrow \gamma\gamma$, $\mathrm{h} \rightarrow \mathrm{b\bar{b}}$, $\mathrm{h} \rightarrow \tau\tau$, $\mathrm{h} \rightarrow \mathrm{WW}$, or $\mathrm{h} \rightarrow \mathrm{ZZ}$ channels [23–32]. This thesis will explain the first CMS search for DM in the $\mathrm{h} \rightarrow \gamma\gamma$ channel, which is published in Ref. [28] and Ref. [29] for the 2015 and 2016 data sets, respectively. The two benchmark signal models used in this analysis are detailed in the following section.

2.5 Signal models

There are many proposed extensions to the SM that provide new SM-DM interactions and DM particle candidates. There are also many proposed extensions that rely uniquely on the Higgs boson to facilitate these interactions. Generally, these models can be split into effective field theories (EFTs) or simplified models. The EFTs introduce non-renormalizable operators thereby generating $\mathrm{h} + \mathrm{DM}$ directly without specifying the underlying particles involved in the interaction. On the other hand, simplified models offer an explicit model where

new particles are introduced that mediate the DM-SM particle interactions. Both EFTs and simplified models are useful for exploring beyond the SM physics, and DM searches have been interpreted in both ways.

The results for the Mono-h search presented here are solely interpreted in the context of two benchmark simplified models. The signal models (descriptions to follow), recommended by the LHC Dark Matter Forum [16], are a Z′-two-Higgs-doublet model (Z′-2HDM) and a baryonic Z′ model. Mono-h searches have a unique sensitivity to the Z′-2HDM signal [16], whereas the baryonic Z′ model offers a way to compare Mono-h results with direct DM detection experiments. Simulated samples of these models, used for choosing the analysis selection criteria and estimating the sensitivity of the search, are made at leading order (LO) by the MADGRAPH5_aMC@NLO v2.3.0 [33] generator. The decay of the Higgs boson to two photons is simulated by PYTHIA 8.205 [34].

2.5.1 Z′-2HDM interpretation

In the Z′-2HDM scenario, the standard model is extended by an additional $U(1)_{Z'}$ symmetry, with a corresponding massive Z′ gauge boson while an additional $SU(2)$ scalar doublet extends the Higgs sector. Resonant production of the Z′ is possible and can produce a Mono-h signal when the Z′ decays to a Higgs boson h and a pseudoscalar A, which decays to a pair of Dirac fermion DM particles. The LO Feynman diagram for the Z′-2HDM production of dark matter is shown in Fig. 2.9.

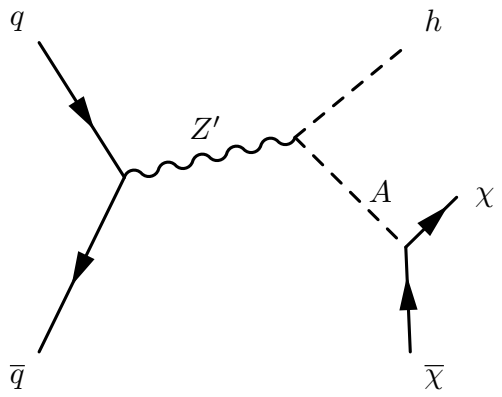

Figure 2.9: The LO Feynman diagram of Z′-2HDM associated production of DM (χ) with a Higgs boson.

The interesting particles in this Z′-2HDM scenario are:

- the massive Z′ gauge boson
- the pseudoscalar A
- Dirac fermion dark matter χ
- two charged scalars $\mathrm{H}^{\pm}$
- a heavy neutral scalar H
- a lighter neutral scalar h (assumed to be the observed Higgs boson).

A Type-2 2HDM framework [35,36] is used to formulate the extended Higgs sector in this model. As mentioned in Section 2.2, the standard model Higgs mechanism requires a single $SU(2)$ scalar doublet. The ground state of this doublet spontaneously breaks the electroweak symmetry which gives masses to the other SM particles. Instead of assuming a single scalar doublet, in a 2HDM, two scalar doublets are added. This yields eight fields: three are Goldstone bosons which are eaten to give the W and Z bosons mass (as in the SM) and five are physical scalar Higgs fields. The five Higgs fields include two charged

scalars $\mathrm{H}^{\pm}$, a heavy neutral scalar H, a lighter neutral scalar h which is assumed to be the observed 125 GeV Higgs boson, and one pseudoscalar A. The A is assumed to have a large branching fraction ($\mathcal{B}$) to the dark matter particles.

Without any additional constraints, the introduction of a second scalar doublet can introduce flavor changing neutral currents (FCNCs) at tree level. In 2HDMs, the Yukawa couplings for fermions with the neutral scalars are not simultaneously diagonalizable, which allows for FCNCs mediated by the neutral Higgs scalars. Tree-level FCNC is strongly disfavored experimentally, for example by searches for $\mathrm{b} \to \mathrm{s}\gamma$ at CLEO [37]. To avoid these constraints, in a Type-2 2HDM, up-type quarks only couple to one Higgs doublet Φ_u while down-type quarks and leptons couple to the other doublet Φ_d [35].

After electroweak symmetry breaking, the Φ_u and Φ_d doublets attain vacuum expectation values of ν_u and ν_d, respectively. In the unitary gauge, the doublets are parameterized as:

$$\Phi_u = \frac{1}{\sqrt{2}} \begin{pmatrix} \cos\beta\ \mathrm{H}^+ \\ \nu_u + \cos\alpha\ \mathrm{h} + \sin\alpha\ \mathrm{H} + i\cos\beta\ \mathrm{A} \end{pmatrix} \tag{2.9}$$

$$\Phi_d = \frac{1}{\sqrt{2}} \begin{pmatrix} -\sin\beta\ \mathrm{H}^+ \\ \nu_d - \sin\alpha\ \mathrm{h} + \cos\alpha\ \mathrm{H} - i\sin\beta\ \mathrm{A} \end{pmatrix} \tag{2.10}$$

where the ratio of vacuum expectation values is denoted as $\tan\beta = \nu_u/\nu_d$ and α is the h-H mixing angle. This analysis assumes $\alpha = \beta - \pi/2$, which is the limit where h has SM-like couplings to fermions and gauge bosons [19]. The observed 125 GeV Higgs boson is assumed to be this SM-like Higgs boson and is denoted as h throughout this thesis.

The model is described by several parameters:

- the pseudoscalar mass m_{A}
- the DM mass m_{DM}
- the Z′ mass $m_{\mathrm{Z}'}$
- the masses of the scalars H and $\mathrm{H}^{\pm}$
- the ratio of vacuum expectation values $\tan\beta = \nu_u/\nu_d$
- the Z′ coupling constant $g_{\mathrm{Z}'}$
- the DM-A coupling constant g_{DM}.

The masses of the Z′ and A are the only parameters that effect the kinematic distributions. The $p_{\mathrm{T}}^{\mathrm{miss}}$ distribution is of particular interest in this analysis and can be seen changing for different values of $m_{\mathrm{Z}'}$ and m_{A} in Fig. 2.10. All other parameters primarily affect the theoretical production cross section σ_{th}, branching fraction, and decay widths of the signal [16]. Therefore, the analysis presented here considers a Z′ resonance with mass between 450 and 2000 GeV, and an A with mass between 300 and 700 GeV.

The scalars H and $\mathrm{H}^{\pm}$ are assumed to have masses at 300 GeV to avoid constraints from $\mathrm{b} \to \mathrm{s}\gamma$ [35]. The parameters $\tan\beta$ and g_{DM} are fixed to unity, while $g_{\mathrm{Z}'} = 0.8$ as recommended by Ref. [16]. The DM mass is fixed to $m_{\mathrm{DM}} = 100\,\mathrm{GeV}$, although since $\mathcal{B}(\mathrm{A} \to \chi\bar{\chi})$ only increases by 7% as m_{DM} decreases, the results presented here are also valid for $1 \leq m_{\mathrm{DM}} < 100\,\mathrm{GeV}$. The value of $\mathcal{B}(\mathrm{A} \to \chi\bar{\chi})$ does decrease when m_{A} is greater than twice the top quark mass, as the decay $\mathrm{A} \to \mathrm{t\bar{t}}$ becomes kinematically accessible. The analysis only considers A decays to DM particles and the signal cross section includes the value of $\mathcal{B}(\mathrm{A} \to \chi\bar{\chi})$.

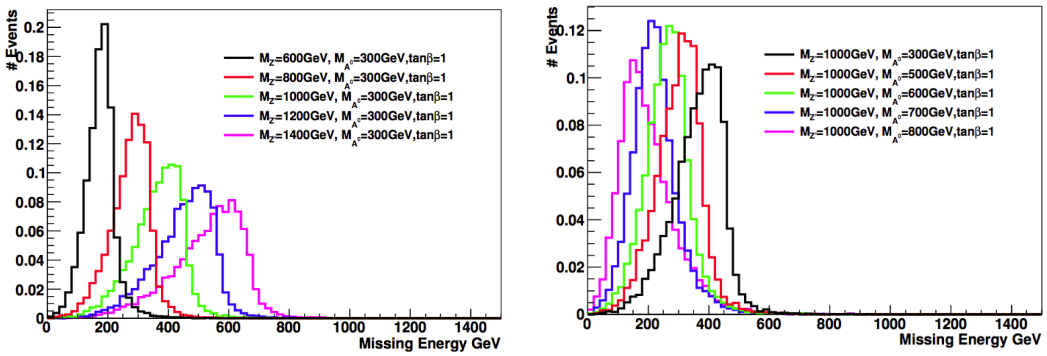

Figure 2.10: The $p_{\mathrm{T}}^{\mathrm{miss}}$ distribution generated in Z′-2HDM simulated samples of $\mathrm{h} + \mathrm{DM}$, varying $m_{\mathrm{Z}'}$ (left) and m_{A} (right) [16].

The decay $\mathrm{Z}' \to \mathrm{Zh}$ is possible in this Z′-2HDM. This decay can also have a Mono-h signature if $\mathrm{Z} \to \nu\nu$. However it is not considered in this analysis, and so the results presented here are somewhat conservative for this model.

2.5.2 Baryonic Z′ interpretation

In a baryonic Z′ model [16, 18] of dark matter production, a new $U(1)_B$ baryon number symmetry is added to the SM with a corresponding vector Z′ gauge boson. It is assumed that the Z′ does not couple to leptons (thus evading dilepton constraints). The consistency of this model necessitates the existence of new stable baryonic states that are neutral under the SM gauge symmetries [38]. In this model, these new states are natural DM candidates. For this search, it is assumed that DM is a Dirac fermion. The particles of interest in this model are: (i) the baryonic Z′ gauge boson mediator, (ii) the baryonic Higgs boson h_B, (iii) the SM Higgs boson h, and (iv) the Dirac fermion DM χ. The Mono-h production of DM is an s-channel process and the corresponding LO Feynman diagram is shown in Fig. 2.11.

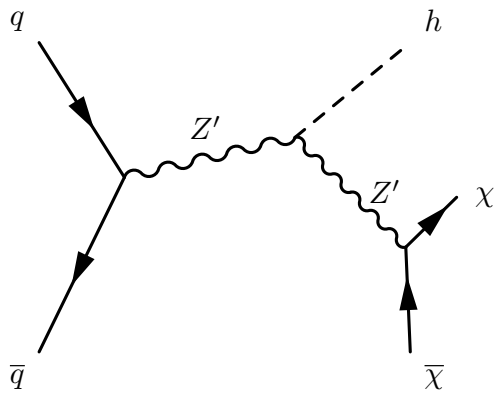

Figure 2.11: The LO Feynman diagram of DM associated production with a Higgs boson in the baryonic Z′ model.

In this model, the Z′ acquires mass from a baryonic Higgs boson h_B which spontaneously breaks the $U(1)_B$ symmetry and acquires a vacuum expectation value ν_B. Generally, the h_B can mix with the SM Higgs boson, which allows the Z′ to interact with the SM h. The h-h_B mixing angle denoted $\sin\theta$ determines the Z′-h coupling $g_{\mathrm{hZ'Z'}} = 2m^2_{\mathrm{Z'}}\sin\theta/\nu_B$.

The model is specified by the parameters:

- the Z′ mass $m_{\mathrm{Z'}}$
- the DM mass m_{DM}
- the h-h_B mixing angle $\sin\theta$
- the DM-Z′ coupling constant g_{DM}
- the quark couplings g_{q}
- the h-Z′ coupling $g_{\mathrm{hZ'Z'}}$.

Only the $m_{\mathrm{Z'}}$ and m_{DM} parameters effect the kinematic distributions. The $p_{\mathrm{T}}^{\mathrm{miss}}$ distributions for varying DM masses are shown in Fig. 2.12 for two choices of $m_{\mathrm{Z'}}$. The remaining parameters are set following the recommendations of

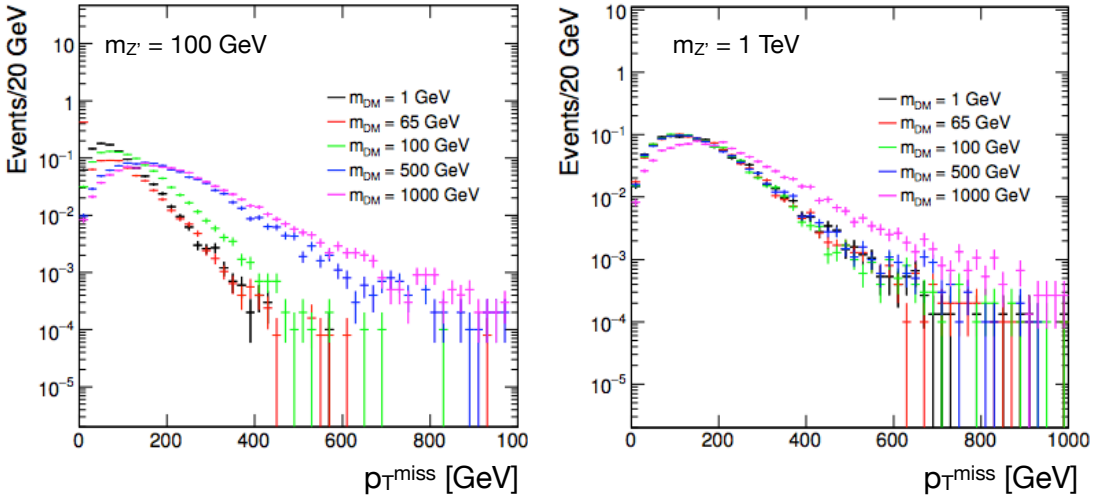

Figure 2.12: The $p_{\mathrm{T}}^{\mathrm{miss}}$ distribution generated in baryonic Z′ simulated samples of $\mathrm{h} + \mathrm{DM}$, for $m_{\mathrm{Z}'} = 100\ \mathrm{GeV}$ (left) and $m_{\mathrm{Z}'} = 1\ \mathrm{TeV}$ (right) [16].

Ref. [16]. The coupling parameters are set to $g_{\mathrm{DM}} = 1$, $g_{\mathrm{q}} = 0.25$ and $g_{\mathrm{hZ'Z'}} = m_{\mathrm{Z}'}^2$, and the mixing angle is set to $\sin\theta = 0.3$. The choice of these parameters maximizes the predicted cross section. Results for other values of these parameters can be obtained by rescaling the cross section.

The analysis scans over the two mass parameters, looking for signals with $m_{\mathrm{Z}'}$ between 100 and 2500 GeV and DM masses between 1 and 900 GeV. If the Z′ has a mass below $m_{\mathrm{h}}/2 \approx 60\ \mathrm{GeV}$, then the decay $\mathrm{h} \to \mathrm{Z'Z'}$ becomes kinematically accessible. This would change the branching fractions of the SM-like h and therefore is not considered in this analysis.

CHAPTER 3

THE LHC AND CMS APPARATUS

The apparatus used in the search for dark matter are the Large Hadron Collider (LHC) and the Compact Muon Solenoid (CMS) detector. The LHC, described in Sec. 3.1, is used to accelerate protons and bring them into collision at the center of the CMS detector. The CMS detector and its subdetectors are described in Sec. 3.2.

3.1 Large Hadron Collider

The LHC [39] is the most powerful particle accelerator and collider built to date. The LHC is a two-beam superconducting hadron accelerator that was constructed inside the already existing 27 km circumference LEP tunnel. It lies approximately 100 m underground near the city of Geneva and the France-Swiss border. The LHC provides proton-proton (pp) collisions at the CMS detector every 25 ns. The LHC was designed to collide protons at $\sqrt{s} = 14$ TeV and with a peak luminosity of $10^{34}\,\mathrm{cm}^{-2}\,\mathrm{s}^{-1}$. Currently, the maximum energy provided by the LHC is $\sqrt{s} = 13$ TeV.

The rate of events $R_{events} = \sigma\mathcal{L}$ produced at the LHC is a function of the production cross section σ and the machine luminosity $\mathcal{L}$. The luminosity is a measurement of the flux of collisions per unit time and depends only on the beam parameters. Luminosity is a function of the number of particles per bunch of each beam N_1 and N_2, the number of bunches per beam n_b, the revolution frequency f_{rev}, the cross sectional area of the beams A, and a reduction factor F

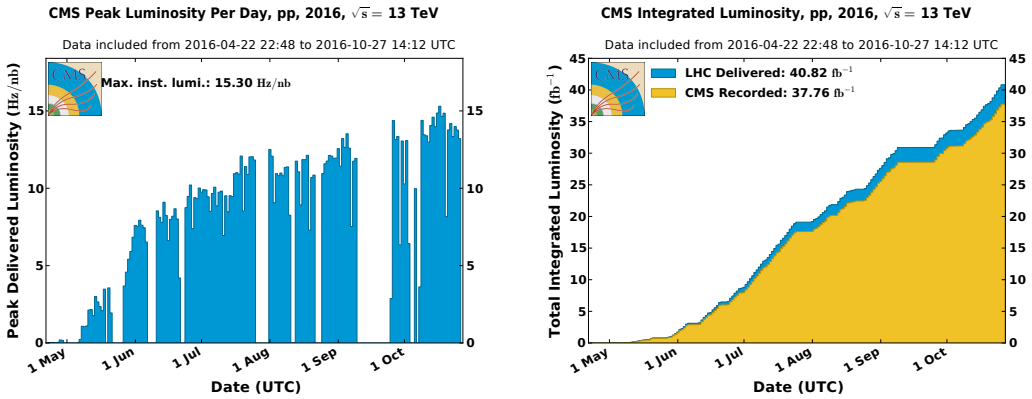

Figure 3.1: The peak luminosity (left) and cumulative integrated luminosity (right) delivered by the LHC day-by-day during the 2016 run [41].

dependent on the crossing angles of the beams. The luminosity is given by [40]:

$$\mathcal{L} = \frac{N_1 N_2 n_b f_{rev}}{AF}, \tag{3.1}$$

where the cross sectional area of the beams $A = \frac{4\pi\epsilon_n\beta^*}{\gamma}$ is determined by the emittance ϵ_n (spread of the beam in position and momentum phase space) and the β^*, the transverse size of the beam along the beam trajectory.

Based on the production rate, the total number of collisions generated at the LHC is

$$N_{events} = \int \sigma \mathcal{L} dt, \tag{3.2}$$

which is a function of the instantaneous luminosity integrated over the run time (or "integrated luminosity") measured in inverse barns ($1\,\text{barn} = 10^{-34}\,\text{cm}^2$). During 2016, the LHC exceeded its planned peak luminosity and delivered over $40\,\text{fb}^{-1}$ of integrated luminosity. The peak luminosity and integrated luminosity day-by-day in 2016 are shown in Fig. 3.1.

The acceleration of protons in the CERN accelerator complex starts with the extraction of protons from a single bottle of hydrogen gas. The hydrogen gas is disassociated to get free hydrogen atoms. An electric field in the Linac2 is

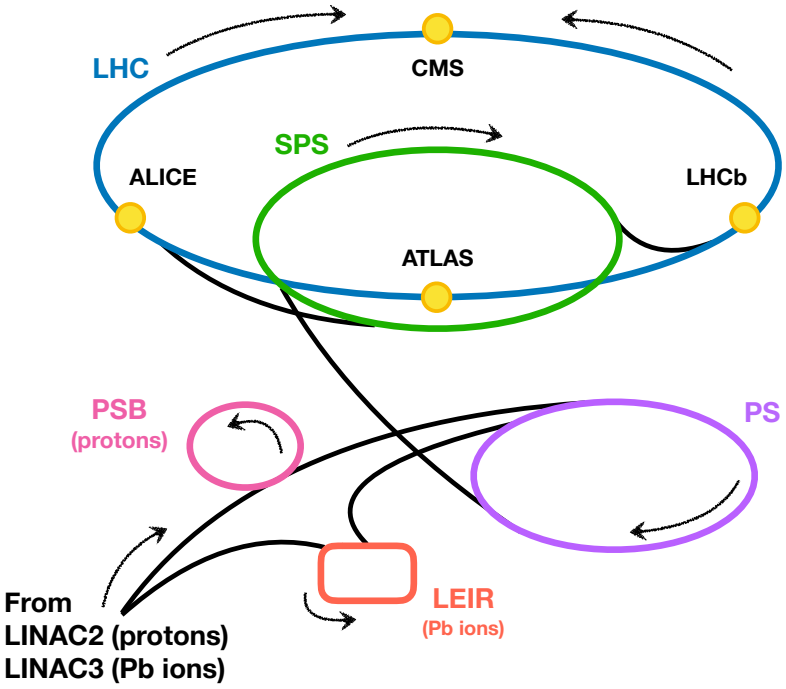

Figure 3.2: Sketch of the CERN accelerator complex (not to scale). Protons injected from LINAC2 go to the PSB then PS then SPS and finally the LHC.

used to strip electrons away from these hydrogen atoms, yielding protons which are accelerated to 50 MeV. Protons are then accelerated through consecutive rings of the LHC complex, as shown in the sketch of Fig. 3.2. The protons are accelerated to 1.4 GeV, 25 GeV, and then 450 GeV by the Proton Synchrotron Booster (PSB), Proton Synchrotron (PS), and then the Super Proton Synchrotron (SPS), consecutively. Finally the protons are supplied to the two beam pipes – tubes kept at ultrahigh vacuum – of the LHC. The LHC accelerates the protons up to their collision energy of 6.5 TeV.

Acceleration and deflection of a beam of protons is achieved using electromagnetic fields since these fields exert a force on any charged particle. Electric fields in radiofrequency (RF) cavities are generated by varying magnetic fields in time. Magnetic fields in RF cavities oscillate (switch directions) at 400 MHz in

the LHC. The RF cavities are built such that electromagnetic waves become resonant in the cavities. Any charged particle that passes through a cavity feels the force from its standing waves. The particles gain energy (or lose energy if they are too fast) from the electromagnetic field in each passage. RF cavities are used to accelerate protons in each of the stages of the CERN accelerator complex.

Magnetic fields are also used to direct the particles to allow the protons to pass in a circle around the accelerator and guide the beam repeatedly through the circular accelerator. The LHC magnet system is composed of niobium-titanium (NbTi) superconductors that are cooled with superfluid helium to 1.9 K. A central feature of the magnet system of the LHC ring are 1,232 main dipoles 15 m in length, each generating magnetic fields of 8.33 T. A cross section of an LHC dipole is shown in Fig. 3.3. These dipoles bend the proton beams tightly around the LHC. The LHC complex has more than 50 types of magnets, including 392 quadrupole magnets that focus (squeeze) the beams. These magnets offer finely-tuned adjustments to the particles' trajectories and spread in space [39].

After rotating around the LHC for about 30 min, the proton beams are brought into collision at the four LHC experiments: ALICE [42], ATLAS [43], CMS [44], and LHCb [45]. ALICE is a heavy ion detector, that primarily examines proton-lead or lead-lead collision events that occur in special month long LHC runs. ATLAS and CMS are both general purpose detectors used for probing pp and heavy ion collisions. LHCb is dedicated to studying CP violation and B hadron decay measurements. The analysis presented in this thesis is performed on pp collision data taken at the CMS detector. Therefore, the rest of this chapter will detail the apparatus of the CMS experiment.

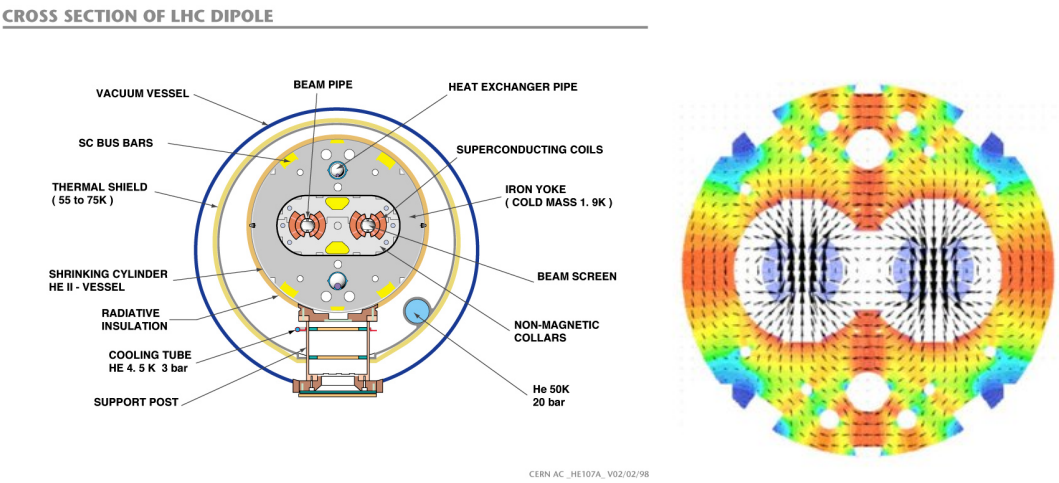

Figure 3.3: Sketch of the cross section of an LHC dipole (left) and the generated magnetic field (right) [46, 47].

3.2 The CMS detector

The CMS experiment, shown in Fig. 3.4, is one of the two general purpose detectors at the LHC. It measures 22 m long by 15 m in diameter and weighs 12,500 tons. The coordinate system used to describe CMS and the data collected there is given in Section 3.2.1. The central feature of the CMS apparatus is a superconducting solenoid, described in Section 3.2.2. Within the solenoid are a silicon pixel and silicon strip tracker (Section 3.2.3), and an electromagnetic (Section 3.2.4) and hadronic (Section 3.2.5) calorimeter. Outside of the solenoid is a muon system described in Section 3.2.6. Additional information about the CMS detector can be found in Ref. [44].

3.2.1 Coordinate system

The CMS detector surrounds a portion of the LHC beam pipe and its coordinate system is inherited from the geometry of this system. The origin is centered at

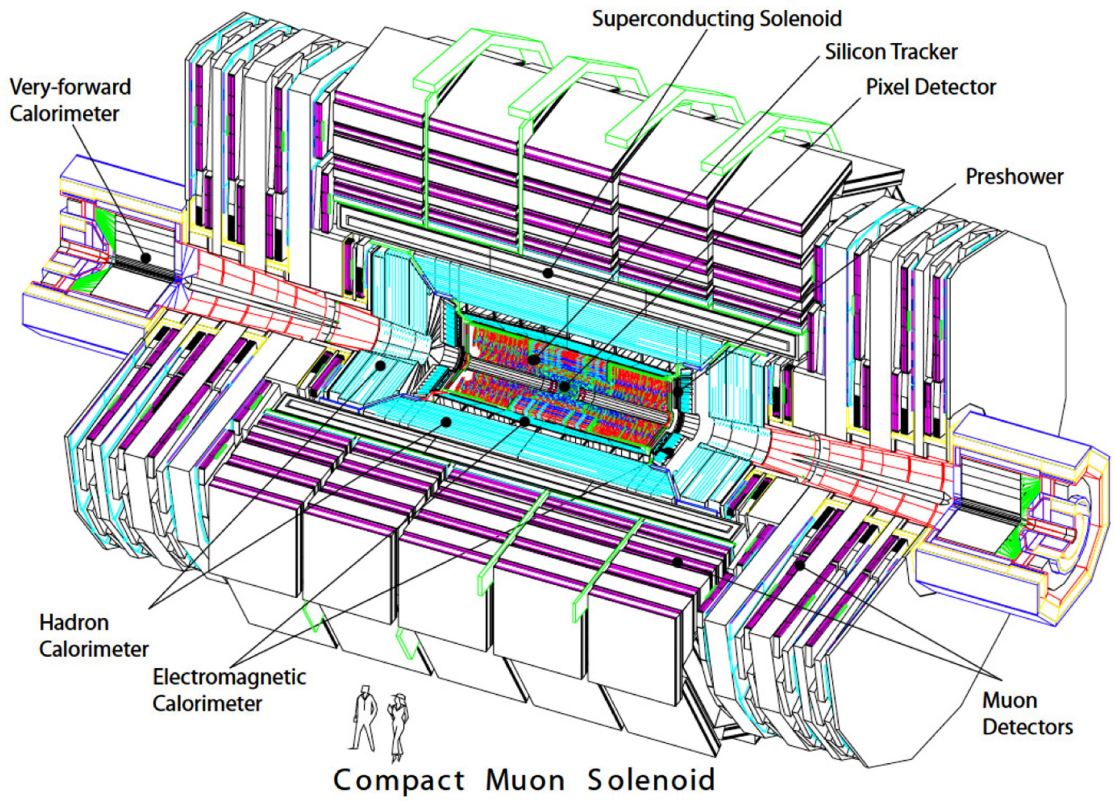

Figure 3.4: Illustration of the CMS detector [44]. A cut out is made to show the subdetectors that make up the inside of the detector.

the nominal collision point in the experiment. The x axis points towards the center of the LHC, while the y axis points upwards. To make a right-handed coordinate system, the z axis direction is along the counterclockwise beam line. Because of the cylindrical nature of the detector, polar coordinates are convenient in this system. The radial distance r gives the distance from the beam pipe, while ϕ is the azimuth angle of the x-y (transverse) plane. The polar angle θ is measured with respect to the counterclockwise beam direction (i.e. the positive z axis). Additionally, it is useful to define the pseudorapidity $\eta = -\ln(\tan(\theta/2))$. Note, the value $\eta = 0$ corresponds to a direction perpendicular to the beam line, while $\eta = \infty$ is parallel to the beam line. Pseudorapidity approaches rapidity $y = \frac{1}{2}\ln(\frac{E+p_z}{E-p_z})$ when a particle's momentum is much higher than its mass.

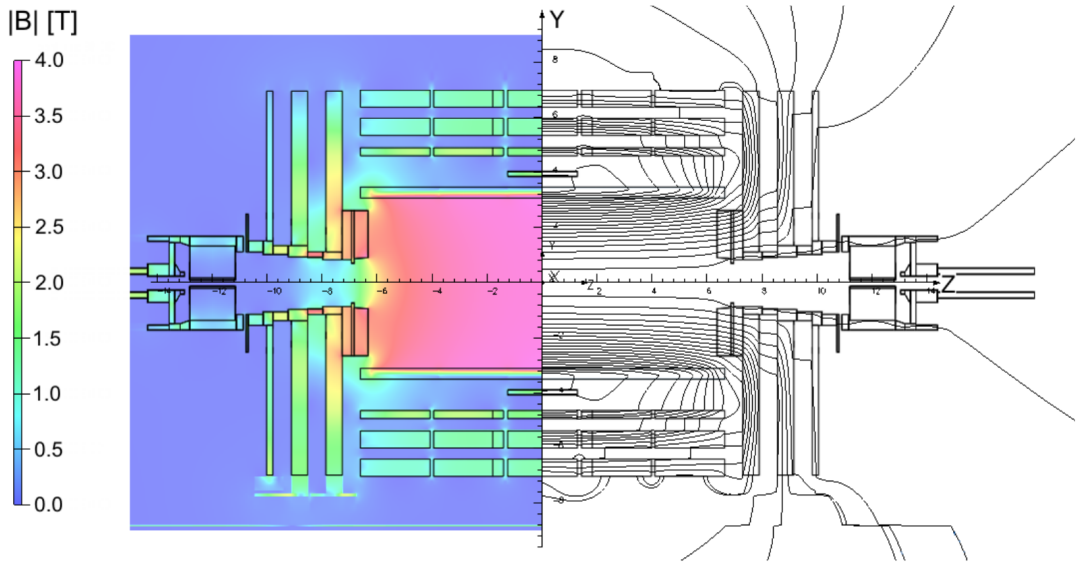

Figure 3.5: Magnetic field and field lines of the CMS solenoid [48].

3.2.2 Solenoid

The central feature of the CMS detector is its superconducting solenoid that provides a uniform magnetic field of 3.8 T along the beam direction, shown in Fig. 3.5. The solenoid, with an inner diameter of 6 m, encases the tracker and calorimeters. In order to achieve a magnetic field of 3.8 T, the magnet is composed of four layers of NbTi superconductor coils. Each coil is reinforced with aluminum conductors. This structure is shown in Fig. 3.6 (left).

The flux of the magnetic field is returned by a 10,000 ton iron yoke. The yoke covers most of the 4π solid angle. The iron yoke, shown in Fig. 3.6 (right), is instrumented as four stations outside of the solenoid and as part of the muon system. In this way, the yoke has the additional benefit of being a stopper for particles entering the muon system. Effectively only muons can make it through the calorimeters and the iron yoke and reach the outer muon chambers.

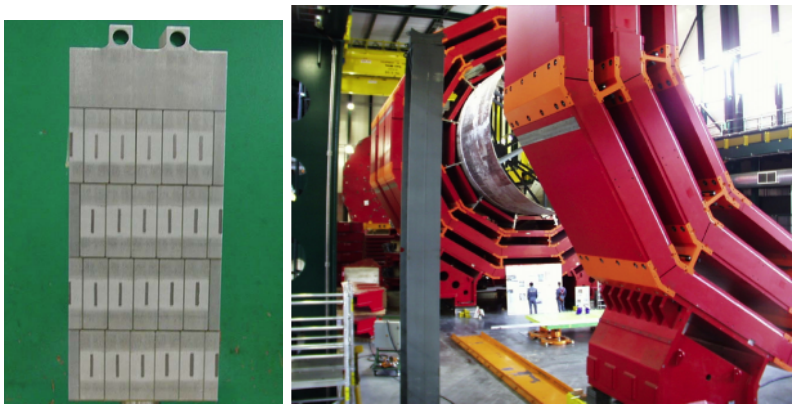

Figure 3.6: Cross section of the reinforced conductor coils (left) and yoke during assembly (right) of the CMS magnet system [44].

3.2.3 Silicon trackers

A silicon pixel and strip tracker [49] is located within the solenoid volume. The pixels occupy the region closest to the interaction point and are described in Sec. 3.2.3. The silicon strip tracker, described in Sec. 3.2.3, lies just outside of the pixel system. Positions of charged particles as they pass through the silicon are recorded and used to recover the particles' trajectories (and consequently their momenta). The pixels record precise three-dimensional positions, while the strip tracker provides coarser one- or two-dimensional position measurements. Trajectories are measured by these inner tracker detectors covering $0 \leq \phi \leq 2\pi$ and $|\eta| < 2.50$. A layout of the tracker system is shown in Fig. 3.7. Images of the pixel and strip tracker are shown in Fig. 3.8.

Pixel detector

The innermost layer of the CMS detector is the silicon pixel detector [49]. Because it is the layer closest to the beam, the pixel detector receives the largest radiation dose of all the CMS detector components. In 2016, the pixel detector

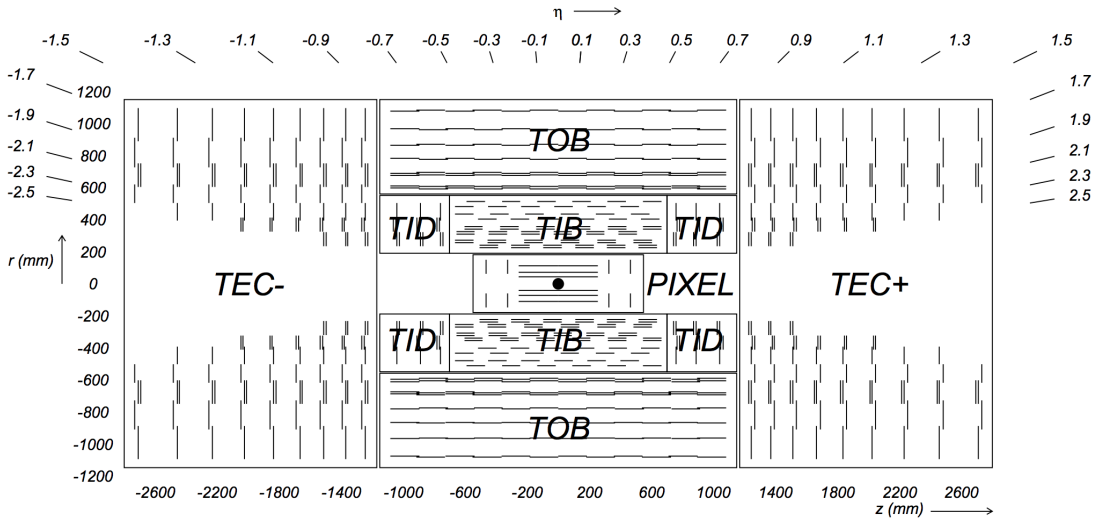

Figure 3.7: Schematic of the CMS silicon tracker system [44]. The pixel system makes up the innermost layers, the silicon strip system is composed of several different subdetectors: TIB, TID, TOB, and TEC.

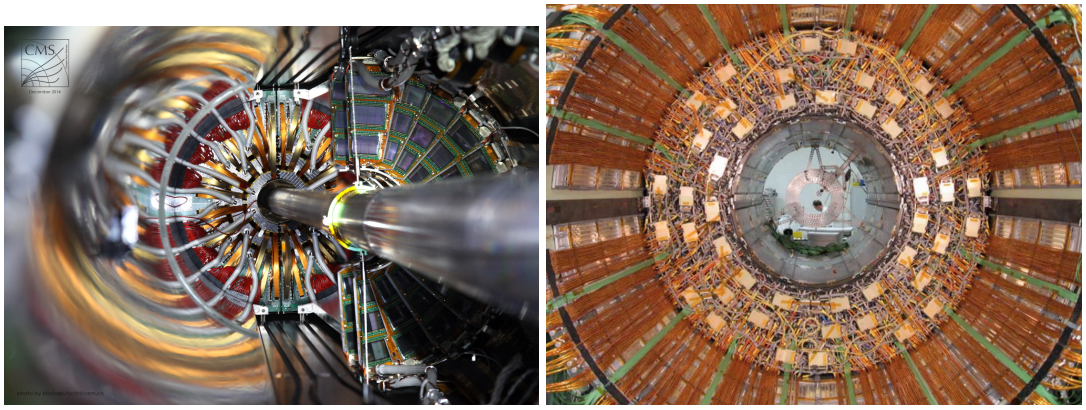

Figure 3.8: Photos of portions of the pixel detector (left) and strip detector (right) during installation [44, 50].

reached the end of its usable lifespan and was replaced in preparation for the remainder of Run 2 and Run 3 (2017-2023). The pixel detector in 2015 and 2016, the time of the analyses presented in this thesis, is described below.

The pixel detector is composed of 66 million silicon pixels that are spread over three cylindrical layers at radii of 4.4, 7.3, and 10.2 cm from the beam pipe and two endcap disks located at $|z| = 34.6$ and 46.5 cm. The pixel detector is

designed such that any charged particle traversing the detector should have three precise position measurements.

The sensors are 100 μm by 150 μm pixels composed of high dose n-implants in a high resistance n-substrate. This radiation-hard design ensures a high signal charge at moderate bias voltages. A charged particle will cause electrons to be ejected from the silicon atoms and create electron-hole pairs. These charges are collected on the surface by an electric current. Read-out chips (ROCs) with a custom ASIC are bump bonded to a 52×80 set of pixel sensors. A detector module is composed of 8 to 16 ROCs. A token bit manager orchestrates the read out of the ROCs in each module.

Silicon strip tracker

The silicon strip tracker [49] is located just outside of the pixel detector in the radial region between 20 and 116 cm. The strip tracker is composed of three systems: the tracker inner barrel/disks (TIB/TID), the tracker outer barrel (TOB), and tracker endcaps (TECs). The sensor elements are single sided p-on-n type silicon micro-strip sensors. Custom integrated circuits amplify, shape, and store the signals from the silicon sensors. The CMS tracker is the largest silicon tracker ever built. It is composed of 24,244 silicon strip sensors covering a region of 198 m^2.

The TIB/TID is composed of 320 μm thick silicon strips positioned parallel to the beam axis in four barrel layers and positioned radially in three disks at each end. The strip pitch is 80 μm for layers 1 and 2, 120 μm for layers 3 and 4, and varied between 100 and 141 μm for the disks. The TOB is made of 500 μm

thick strips with pitches of 183 μm on the four inner layers and 122 μm on the outer two layers. The strip side of the sensor provides a measurement of the ϕ position of a particle hit. A second sensor is mounted back-to-back with a stereo angle of 100 mrad to provide a measurement of the z coordinate in the TIB and TOB and r coordinate in the TID.

Beyond the TOB, the TEC covers the region $124 < |z| < 282$ cm. Each TEC subdetector is composed of nine disks with up to seven rings of silicon strips. The strips on the inner four (outer three) rings are 320 μm (500 μm) thick. The strips are arranged radially and have pitches varying from 97 to 184 μm. Rings 1, 2, and 5 of the TEC have second rotated strip sensors back-to-back thus providing measures of the r coordinate.

A charged particle with $|\eta| < 2.4$ should have about nine hits in the silicon strip tracker and at least four two-dimensional measurements. The design provides a single point resolution of about 23 to 53 μm for ϕ and 230 to 530 μm for z/r coordinates. Alignment of the tracker is monitored frequently with lasers and reconstructed tracks.

3.2.4 Electromagnetic calorimeter

Outside of the silicon tracker system at a radius of 1.29 m is a lead tungstate ($PbWO_4$) crystal electromagnetic calorimeter (ECAL) [51]. The ECAL is a hermetic homogeneous calorimeter composed of 61,200 crystals in the barrel and about 15,000 crystals in the endcaps. The barrel calorimeter (EB) covers the region $|\eta| < 1.479$, while the endcaps (EE) cover $1.479 < |\eta| < 3.0$. An additional preshower detector is located in front of the EE detectors in the region

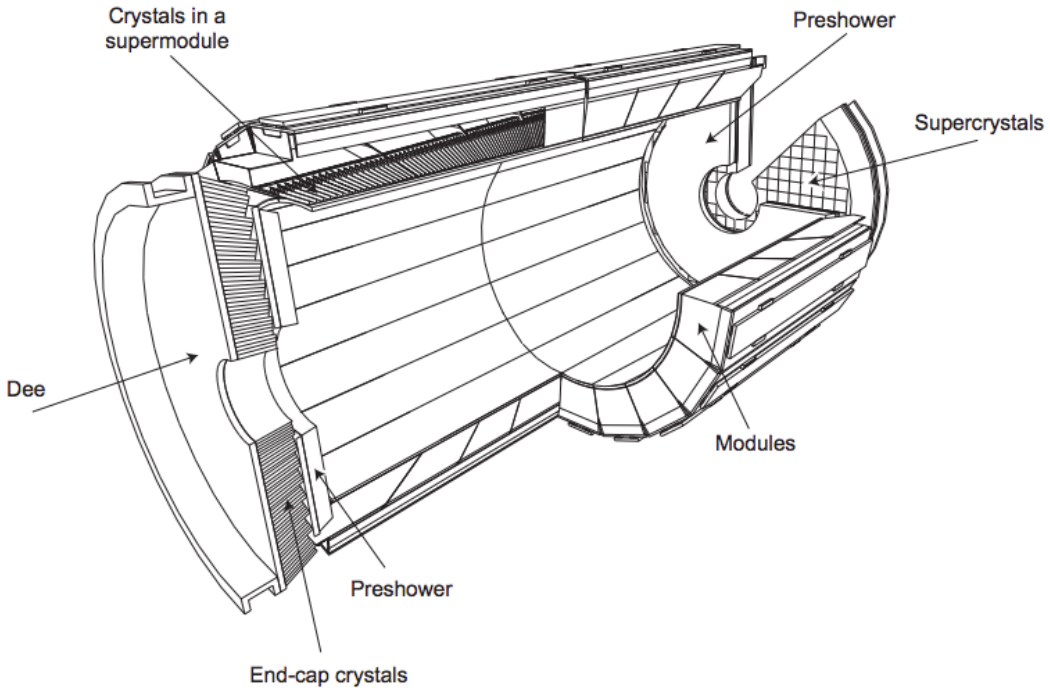

Figure 3.9: Schematic of the CMS electromagnetic calorimeter [44].

$1.653 < |\eta| < 2.6$. A schematic of the ECAL is shown in Fig. 3.9.

The $PbWO_4$ crystals, shown in Fig. 3.10 (left), are very dense, but highly transparent scintillators. The scintillator emits 80% of the light in 25 ns, comparable to the LHC bunch spacing. Their short radiation length (0.89 cm) and Moliére radius (2.2 cm) means electromagnetic showers are relatively small, allowing for a precise position measurement. The performance of the crystals is temperature dependent. To maintain the necessary resolution, the crystals have to be kept at $18 \pm 0.05\,^{\circ}$C. Lasers are used to monitor the loss of optical transmission in the crystals due to radiation.

In the EB, the crystals are aligned in a quasi-projective geometry (visible in Fig. 3.9) to avoid having gaps aligned with particle trajectories. This means the crystals are oriented with a 3° offset in both η and ϕ between the crystal's

Figure 3.10: Lead tungstate crystal and light collector from the ECAL (left) and brass and plastic scintillator towers from the HCAL (right) [44].

axis and the trajectory from the interaction point. The EB crystals have a tapered shape, the front face of the crystal is $22\times22\,\mathrm{mm}^2$ while the rear face is $26\times26\,\mathrm{mm}^2$. The crystals are 230 mm long which corresponds to 25.8 radiation lengths. The granularity $(\Delta\eta, \Delta\phi)$ is approximately $(0.0174, 0.0174)$. A pair of avalanche photodiodes collect the light emitted by each crystal in the barrel.

In the EE, 5×5 units (supercrystals) of crystals are mounted at angles from 3 to 8°. The front and rear face of the EE crystals are $28.6\times28.6\,\mathrm{mm}^2$ and $30\times30\,\mathrm{mm}^2$, respectively. The crystals are 220 mm long in the EE. A single vacuum phototriode collects the light at the back of each crystal in the endcaps.

The preshower detector is a 20 cm thick sampling calorimeter composed of two layers of lead radiators which initiate electromagnetic showers and two layers of silicon strip sensors that measure the deposited energy. The silicon strips have a 1.9 μm pitch and cover an active area of $61\times61\,\mathrm{mm}^2$. The preshower improves the spatial resolution of the EE which improves photon and neutral pion identification capabilities of the ECAL.

Only above energies of about 500 GeV does leakage out of the rear of the ECAL become significant. Below this, in the typical range of particles produced

at CMS, the energy resolution of the ECAL can be parameterized as [44]:

$$(\frac{\sigma}{E})^2 = (\frac{2.8\%}{\sqrt{E}})^2 + (\frac{0.12}{E})^2 + (0.30\%)^2. \tag{3.3}$$

The first term is the stochastic term, second term is the noise term, and the last is a constant term. The stochastic energy resolution comes from photostatistics, event-by-event fluctuations in the shower containment, and differences in energy deposited and measured by the preshower. Electronic noise, digitization noise, and pileup contribute to the noise term. The constant term arises from energy leakage out the rear, intercallibration errors, and the nonuniformity of longitudinal light collection.

3.2.5 Hadronic calorimeter

Directly outside of the ECAL is a brass and scintillator hadron calorimeter (HCAL) [52] that occupies the radial region from 1.77 to 2.95 m. The HCAL is a hermetic sampling calorimeter that measures a particle's position, energy, and arrival time. This portion of the CMS detector is particularly important for jet and $p_{\mathrm{T}}^{\mathrm{miss}}$ reconstruction. The HCAL is composed of four main components: the barrel (HB), the endcaps (HE), the outer barrel calorimeter (HO), and the forward calorimeter (HF). A schematic of the HCAL is shown in Fig. 3.11.

A tower in the HCAL is composed of several alternating layers of absorbers and plastic scintillators, shown in Fig. 3.10 (right). Generally, incoming particles hit the dense absorber layers and interact creating numerous secondary particles. The shower of particles then passes through the scintillating layers causing them to emit light. The light recorded from all layers of the tower by a hybrid photodiode is a measure of the energy of the incoming particle.

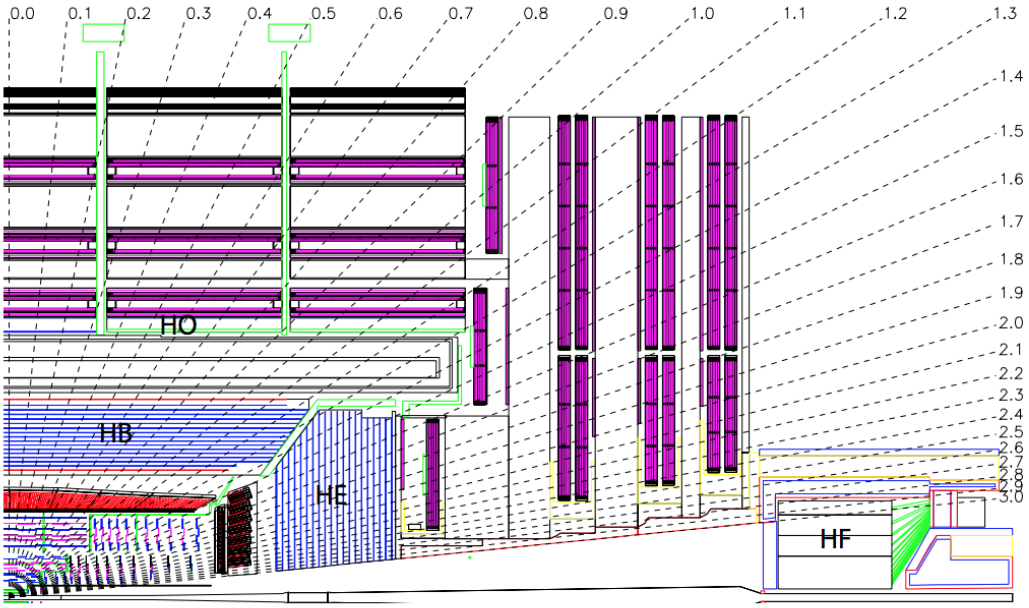

Figure 3.11: Longitudinal schematic of the CMS hadronic calorimeter [44].

The HB surrounds the ECAL and fits inside of the solenoid and is extended to $|\eta| < 1.3$. For structural support, stainless steel absorbers are used for the first and last layer of the HB towers. The towers in the HB are composed of 18 brass absorbers and 15 plastic scintillator layers 3.7 mm thick. An additional first and last scintillator are each 9 mm thick. The tower composition of the HE is similar to that of the HB. A tower is composed of 18 brass layers and 17 plastic scintillators with an additional first scintillator 9 mm thick. The HE extends from $1.3 < |\eta| < 3.0$. The HCAL segmentation $(\Delta\eta, \Delta\phi)$ is approximately $(0.087, 0.087)$ for the region $|\eta| < 1.6$ and $(0.17, 0.17)$ for the region $1.6 < |\eta| < 3.0$.

The HO ensures that any energy that leaks out of the HB is still measured. The HO is found after the first layer of the iron flux return yoke and reaches $|\eta| < 1.3$. A single layer of 10 mm scintillator makes up the HO. The total absorber

thickness of the HCAL is 5.39 radiation lengths [44] near $\eta = 0$. This increases to 10.3 radiation lengths at $|\eta| \approx 1.3$. The HF extends the reach of the HCAL in the forward region to $|\eta| < 5.0$. The HF is composed of a cylindrical steel absorber, radiation-hard quartz fibers are interspersed every 5 mm. The quartz 800 μm diameter fibers act as the active scintillating material.

3.2.6 Muon system

The muon system makes up the outermost layers of the CMS detectors. The CMS experiment uses three types of gas-ionization detectors for muon identification [53]. A sketch of the muon system layout is shown in Fig. 3.12. Since high momentum muons can traverse meters of iron without interacting, they are not stopped by the previous layers of the detector and reach these outer layers. Three types of muon chambers are used to get accurate position measurements.

Drift tube (DT) chambers cover the region $|\eta| < 1.2$ and are organized into four stations that are interspersed among the steel flux-return yoke outside of the magnet. Each DT consists of a 4 cm wide gas-filled aluminum tubes. When a charged particle traverses the volume, it ionizes the gas releasing electrons which drift towards the positively-charged wire, as shown in Fig. 3.13 (left). This yields accurate position measurements of the muons throughout the layers of the muon chambers.

In the endcap regions of $0.9 < |\eta| < 2.4$, the muon system is composed of cathode strip chambers (CSCs) also implemented as four interspersed stations. CSCs are composed of positively-charged wires perpendicular to negatively-charged copper strips within the gas volume. As in the DTs, a muon ionizes

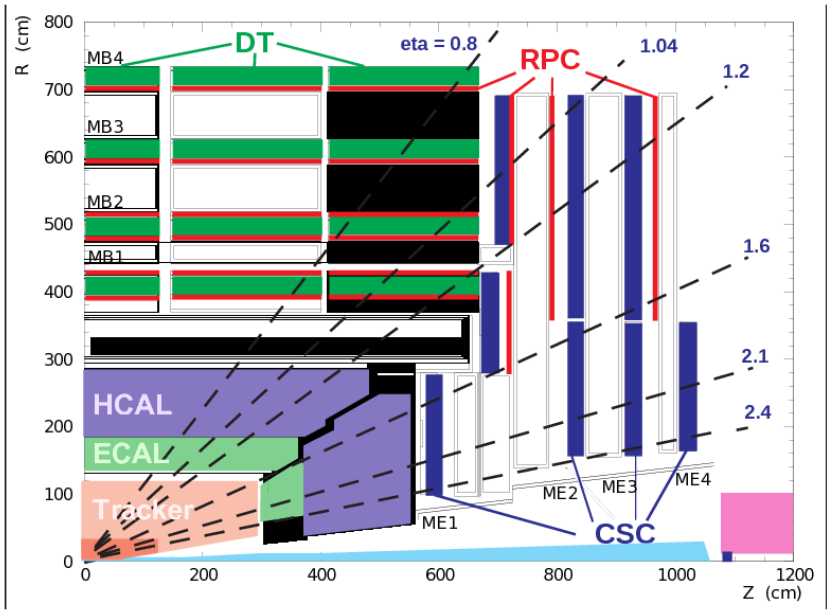

Figure 3.12: Sketch of a quarter of the CMS detector with muon systems labeled [54].

the gas and electrons cascade toward the wires, while positive ions move toward the strips. Because the wires and strips are perpendicular to each other, the passing particle is registered in two position coordinates. The effect of a traversing muon in a CSC is sketched in Fig. 3.13 (right).

In addition, there are six layers of resistive plate chambers (RPCs) in the range of $|\eta| < 1.6$ for use in the trigger system because of their precise timing resolution of about 1 ns. The RPCs are composed of two oppositely-charged parallel plates separated by a gas volume. When a particle passes through and ionizes the gas it again create a cascade of electrons. External sensors quickly detect the electrons and the pattern of the hits are used in the trigger to measure the muon's momentum.

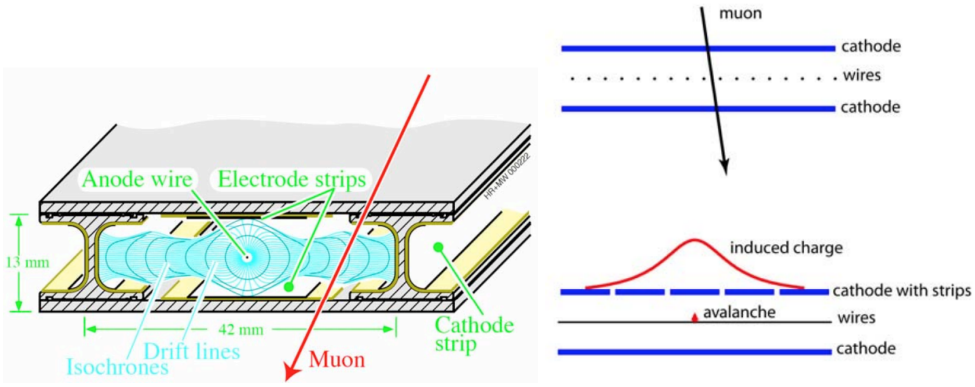

Figure 3.13: Sketch of a muon traversing a DT (left) and a CSC (right) [44].

3.2.7 Data acquisition and trigger system

The CMS trigger and data acquisition system is designed to collect and analyze the information from the CMS detector at the LHC bunch crossing frequency of 40 MHz. At design luminosity, the pp interaction rate at CMS is larger than 1 GHz. However, most of these events are not hard-scattering interactions. CMS relies on a two-tiered trigger system, described in more detail in Ref. [55], to select the most interesting collisions and reduce the stored-data rate to manageable levels. The first level (Level-1 or L1) is a hardware trigger that brings the data rate to 100 kHz, the maximum rate allowed by the CMS readout electronics. Next, a high-level trigger (HLT), implemented in software, further improves the purity of events of interest and reduces the rate to around 400-1000 Hz for offline storage.

Level-1 trigger

Within 4 μs of a collision, the L1 system provides a tentative accept or reject signal. The L1 accepts a collision event if it contains candidate physics objects, for example energy clusters consistent with a photon or electron. The current

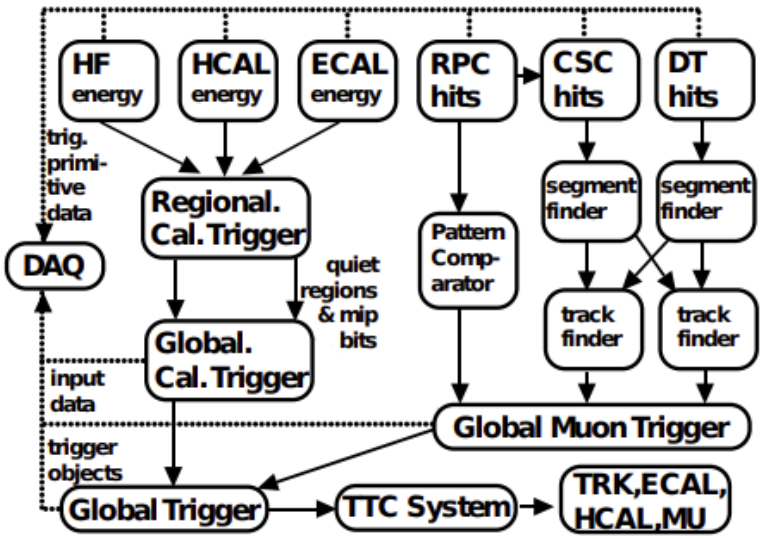

Figure 3.14: Overview of the CMS L1 trigger system [55].

L1 uses only detector information from the calorimeters and muon detectors [1]. A schematic of the L1 trigger is shown in Fig. 3.14. Trigger primitives from the calorimeters (HF, HCAL, and ECAL) and from the muon detectors (RPC, CSC, and DT) are processed in several steps before being sent to the global trigger for the accept/reject decision.

The calorimeter information is processed through two stages: a regional (RCT) and then global (GCT) calorimeter trigger. The RCT processes in parallel energy deposit information from over 8000 ECAL and HCAL towers. The output of the RCT are electron/photon candidates and regional energy sums. In the GCT, the electrons/photons are sorted, jets are found, and global quantities like $p_{\mathrm{T}}^{\mathrm{miss}}$ are calculated. The GCT outputs a sorted subset of the found physics objects to the global trigger.

At the same time, L1 muon objects are constructed from each of the three

[1] Chapter 6 details a proposal for the inclusion of tracker information at L1 for the CMS detector during the HL-LHC era.

muon detector systems. The CSC and DT systems first identify track segments from hit information in their respective stations. These segments are then sent to a track finder system which uses pattern recognition algorithms to identify muon candidates and make a preliminary measurement of their momenta. Hits from the RPCs are directly sent to a pattern comparator to identify muon candidates. The regional track finders just described then send muon candidates to a global muon trigger which merges the lists, and after removing any duplicate objects, outputs muon objects to the global trigger.

The final step of the L1 trigger is the global trigger which makes the official accept/reject decision. The triggers are a set of quality and momentum requirements on each object that are applied to the final list of physics objects that were sent from the calorimeters and muon systems. If the data is accepted, the signal is sent to readout the whole CMS detector and forward the data to the HLT for the next stage of the decision.

Data acquisition system

The L1 trigger, as mentioned earlier, is designed to reduce the event rate to 100 kHz. The raw signals from the entire CMS detector must be readout at this rate. There are about 55 million channels in the detector, which get condensed to an output data rate of about 100 Gbps. Front-end systems store data continuously in 40 MHz pipelined buffers [44]. Upon arrival of the L1 accept decision, data are sent from the buffers to the data acquisition system. From there, all data for an event is combined into a complete event which is then sent to the event filter farm of the HLT.

High-level trigger

After passing the L1 trigger, an event is processed by the HLT using algorithms similar to those of the offline processing. The HLT processing occurs on approximately 13,000 CPU cores. The HLT can take up to about 175 ms to process a single event. The event filters of the HLT reconstruct physics objects from the raw detector data. Then, the selection is applied as a sequence of steps. If at any point, the physics objects do not pass the selection of that step, the processing stops. Accepted events are then transferred for offline reconstruction and storage.

CHAPTER 4

RECONSTRUCTION OF PHYSICS OBJECTS

General information about event reconstruction is presented first in Sec. 4.1. Charged particle track reconstruction and vertex identification are detailed in Sec. 4.2 and Sec. 4.3, respectively. Then additional details about the reconstruction of each of the physics objects used in the Mono-h analysis, namely photons, jets, and $p_{\mathrm{T}}^{\mathrm{miss}}$, are described in more detail in Secs. 4.4, 4.5, and 4.6.

4.1 Event reconstruction

Both data and simulated events undergo the same event reconstruction. In the case of simulated events, GEANT4 [56] first models the CMS detector response to generated particle physics signals. The data (and simulated) signals from the CMS detector are then reconstructed into physics objects. The reconstruction is handled by the particle-flow (PF) algorithm [57] which combines information from all CMS subdetectors to perform a global event reconstruction.

Particle-flow is a heuristic algorithm that generates a list of stable particles (PF candidates), namely protons, electrons, muons, and charged and neutral hadrons. Photon energy is obtained from ECAL measurements. The energy of electrons is made from a combination of the ECAL cluster measurement, the electron momentum from the tracker, and the energy sum of all bremsstrahlung photons spatially compatible with the electron track. Muon energy is determined from the curvature of the muon track. Charged hadron energy is determined from the momentum measured in the tracker and the matching ECAL and HCAL energy deposits. Neutral hadron energy is obtained solely from the

ECAL and HCAL energies.

4.2 Charged particle track reconstruction

In the LHC collision environment, charged particle track reconstruction is extremely important. Currently, the CMS detector has approximately 2,000 tracks per event. Charged particles leave distinctive hits in the CMS tracker (described in Sec. 3.2.3). Since charged particles curl in a magnetic field, the particles have a helical trajectory in the detector. Reconstructing quickly and accurately the trajectories from the hits is accomplished through dedicated software algorithms. The track reconstruction occurs as a sequence of steps [58]: (i) hit reconstruction, (ii) seed generation, (iii) track finding, (iv) track fitting, and finally (v) selection.

First, hits are reconstructed in the pixel and strip detectors. In the pixel detector, any pixel above its single pixel threshold are read out, others are zero-suppressed. Pixel clusters are formed by adjacent above-threshold pixels. The cluster position is found from a charge-weighted average of the individual pixel positions. In the strip detector, a strip is accepted if its charge exceeds five times the channel noise, or if the strip and one of its neighbors exceed twice the channel noise. Strips with charge three times the noise level act as seeds. Neighboring strips above threshold are added to form a cluster. A charge-weighted average is used to extract the hit position of the cluster. These positions are then translated to the global coordinate system, taking into account the alignment measurements of the tracker.

An iterative tracking procedure [58] is used to reconstruct the trajectories. The first iteration produces tracks that are the easiest to find (ie. prompt tracks

with relatively large p_{T}). Hits associated with these tracks are removed for subsequent iterations. This reduces some of the combinatorial complexity of finding more difficult tracks (for example, displaced tracks or tracks with missing hits or low p_{T}).

In each iteration, seeds (initial track candidates) are found first using three hits with three-dimensional positions. Five track parameters are needed to describe a charged particle's helical trajectory: p_{T}, η, the angle at the point of closest approach ϕ_0, the z position at closest at closest approach z_0, and the x-y distance at closest approach or impact parameter d_0. Seeds give an initial estimate of these track parameters and uncertainties.

Track finding is based on the Kalman filter method [59–61]. Using the initial track parameter estimate, tracks are projected to successive detector layers. Multiple scattering and energy loss are considered in the estimation of the trajectory to the next layer. In each layer, the algorithm looks for compatible hits within a small search window. Tracks are built up by adding a hit from successive detector layers. At each layer, the track parameters are updated.

The final track fitting takes into account the information from all collected hits and gives the final and best estimate of the track parameters. A Kalman filter and smoother are used to extract the final trajectories. Starting with the innermost hits, the track parameters are again estimated and iteratively corrected by each successive hit. After a track is built, the parameters are smoothed by applying the same process working backwards towards the beam line.

In the track fitting stage, a Runge-Kutta propagator [62] is used to extrapolate the trajectory. This takes into effect the material interactions and inhomoge-

neous magnetic field. The non-perfect helical trajectory is estimated over many small steps to improve the accuracy of the model. This method is also used later to estimate the point of closest approach for the final track.

This method can produce a large number of reconstructed tracks that are not associated with a charged particle. Applying selection requirements on the number of hits, quality of the track, and compatibility with a vertex can reduce significantly these spurious tracks.

4.3 Vertex reconstruction

Charged particle tracks are used to reconstruct interaction vertices in collision events. A vertex is made from a collection of tracks that appear to originate from the same z position. The fit of the clustered tracks is then used to extract the exact position of the vertex. The z coordinate of the reconstructed vertices distinguishes particles from the hard interaction and those from pileup interactions.

The $\mathrm{h} + \mathrm{DM}$ signature is tricky for vertexing because neither photons or $p_{\mathrm{T}}^{\mathrm{miss}}$ produce tracks and selecting an incorrect vertex can reduce the mass resolution. However, if the reconstructed vertex is within 1 cm of the true vertex, the mass resolution is dominated by the photon energy resolution. The reconstructed vertex with the largest value of the physics-object p_{T}^2 is taken to be the primary pp interaction vertex (PV). The efficiency to find the PV within 1 cm of the true vertex, for the signal simulated samples, is roughly 70%. In the SM $\mathrm{h} \to \gamma\gamma$ analysis [63], a boosted decision tree is used to select the vertex, however this has only modest gains in vertexing efficiency, and is not used in the Mono-h

analysis since the $p_{\mathrm{T}}^{\mathrm{miss}}$ is calculated with respect to the largest p_{T}^2 vertex.

To ensure a quality vertex, additional selection criteria are applied. Consistency between the PV and interaction point is enforced by requiring the z position of the vertex be less than 24 cm, and the distance from the interaction point in the x-y plane be less than 2 cm. Also, the number of degrees of freedom of the vertex is required to be greater than four.

4.4 Photon reconstruction

As mentioned earlier, photons are useful particles for observing the Higgs boson and for searching for new physics because of the excellent resolution of the ECAL in the CMS detector. Reconstruction of photon objects is of particular importance for this analysis. Photons are reconstructed [64] from their energy deposits in the ECAL which are generally spread over several crystals. Due to interactions with material in the region from the beam axis to the ECAL, photons can convert to electrons, and electrons often emit bremsstrahlung photons. Photons and electrons are practically indistinguishable in the ECAL, therefore their reconstruction in the ECAL proceeds exactly the same. Electrons are later distinguished from photons if there are tracks in the silicon tracker that point to an ECAL cluster.

The PF algorithm makes clusters of ECAL crystals using the highest energy crystal as a seed and collecting all immediate neighbor crystals with energies well above the electronic noise levels. Completed clusters with energy greater than 4 GeV are then used to build superclusters (clusters of clusters). Superclusters are small in the η direction, but extended in the ϕ direction to account for

the azimuthal bending of charged particles in the strong magnetic field. These superclusters should contain the majority of the energy from the photon and any conversions. If the energy of the supercluster is larger than $10\ \mathrm{GeV}$ a PF photon candidate is seeded [57].

Mass in the rest frame of the particle is determined by its energy and momentum, quantities that are conserved during a decay. The invariant mass of a system of particles is computed by

$$m = \sqrt{\sum E^2 - ||\sum \vec{p}\,||^2} \tag{4.1}$$

and reconstructs the mass of the mother particle in a decay. In the case of this signal, the diphoton invariant mass $m_{\gamma\gamma}$ is used to estimate the Higgs boson mass and is calculated by

$$m_{\gamma\gamma} = \sqrt{2p_{\mathrm{T}1}p_{\mathrm{T}2}(1-\cos\theta_{12})}, \tag{4.2}$$

which depends on the p_{T} of the leading and subleading photon and the angle θ_{12} between the two photons. Accurate photon energy is therefore a necessary component in the accuracy of the mass distribution. Several corrections are applied to achieve the best energy measurement. Adjustments to the cluster energy correct for individual ECAL channel calibrations [65] and transparency losses. During data taking, the ECAL crystal transparency can vary due to radiation and annealing. The transparency is monitored by measuring each channel's response to laser light injected approximately every 30 minutes. Corresponding corrections are applied per channel during the event processing.

The energy resolution of each cluster also depends on the variation of the shower containment in the cluster. For photons that shower before reaching the ECAL, the cluster energy can vary based on the amount of energy absorbed before the ECAL, how much of the shower energy is clustered, and any cluster

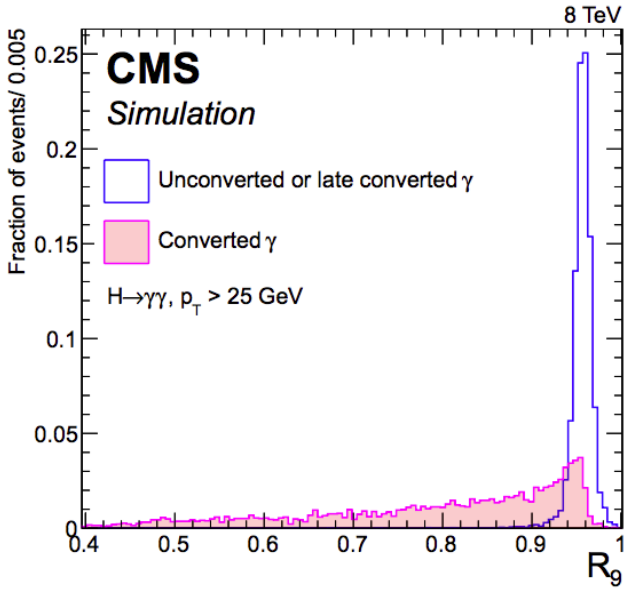

Figure 4.1: Distribution of R_9 for photons that have converted before the ECAL and those that have not [64].

positioning on intermodule voids or off-pointing crystals. The R_9 of a photon supercluster is the energy in a 5×5 grid of crystals centered around the most energetic crystal divided by the supercluster energy. Photons that convert before the ECAL have a wider energy distribution and consequently a broader R_9 distribution. Therefore, R_9 is particularly useful in distinguishing converted and unconverted photons as shown in Fig. 4.1. Corrections for cluster energy are extracted from a multivariate regression technique that is applied as function of energy, η, and R_9.

Finally, after all of the above corrections, there is an additional fine tuning of the energy calibration using comparisons of observed and simulated $\mathrm{Z} \to \mathrm{ee}$ events. In an enriched $\mathrm{Z} \to \mathrm{ee}$ sample, electrons are reconstructed as photons by simply using only ECAL information. The dielectron invariant mass of data and simulated events are compared. The data photon energies are scaled (by less than 1%) to match simulation. Additionally, the energy of simulated events

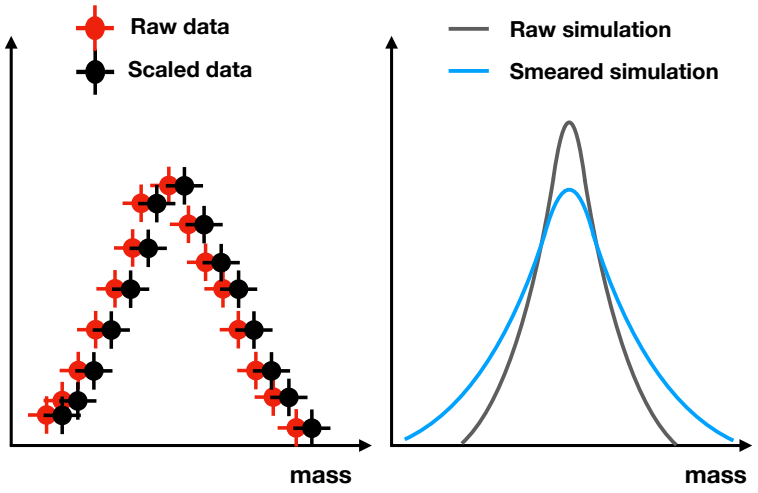

Figure 4.2: Sketch of the effect of scaling (left) and smearing (right) on mass.

is smeared (by less than 2%) to match the resolution of the data. This smearing is likely needed because of a slight underestimation of the amount of material in the detector prior to the ECAL. A sketch of these corrections is shown in Fig. 4.2. After all corrections, the final dielectron invariant mass around the Z boson peak has excellent agreement between data and simulated events as demonstrated in Fig. 4.3.

Since the photon identification was optimized for the Mono-h search, the details on the selection are given later in Section 5.3. However, it is useful to define here several photon-related variables that will go into photon identification criteria in the trigger and ultimate event selection. Identifying photons from candidate objects is based on several variables detailed below:

- R_9: As mentioned earlier, this is the ECAL energy in a 5×5 grid of crystals centered around the most energetic crystal divided by the supercluster energy. This is useful in distinguishing converted and unconverted photons.

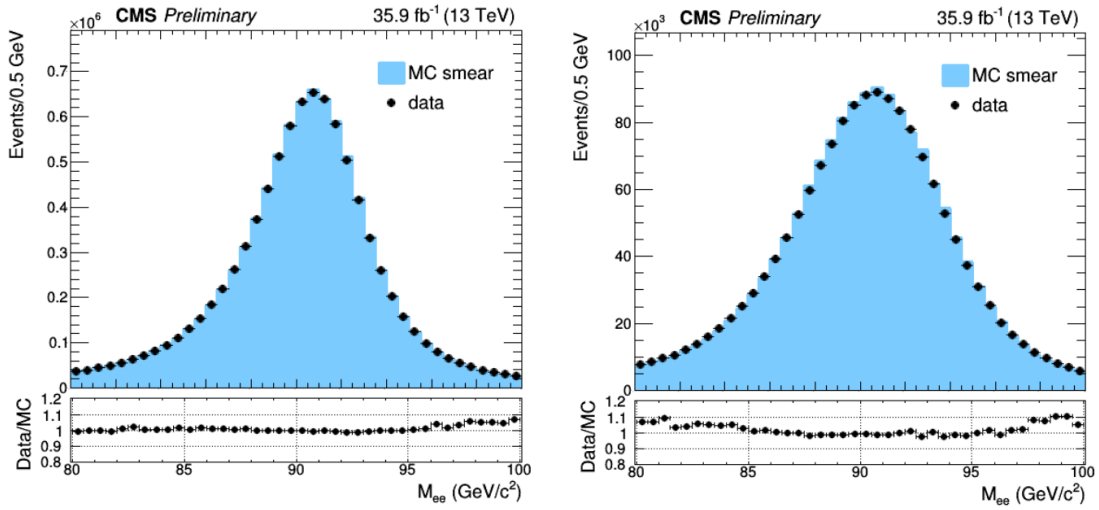

Figure 4.3: Mass distribution of $\mathrm{Z} \to \mathrm{ee}$ events in data and simulated events with all corrections applied for electrons in the barrel (left) and endcap (right) [66].

- $\mathrm{H/E}$: The ratio of hadronic-to-electromagnetic calorimeter energy deposits of the photon candidate. More precisely, this is the ratio of energy in HCAL towers directly behind the supercluster, divided by the supercluster energy. A photon will primarily deposit all of its energy in the ECAL and therefore this ratio should be relatively small.

- $\sigma_{\eta\eta}$: The standard deviation of a single crystal η within a 5×5 grid, weighted by the ratio of the crystal's energy to the supercluster energy. This is effective at describing the spread of the photon cluster. A larger $\sigma_{\eta\eta}$ is indicative of a jet, since photons or electrons will generally deposit all of their energy in one or two crystals in η.

- $\mathrm{I_{Ch}}$: The charged-hadron isolation is computed from a sum of track p_{T} associated with the PV and within a cone of $\Delta\mathrm{R} = \sqrt{(\Delta\eta)^2 + (\Delta\phi)^2} < 0.3$ of the photon candidate.

- $\mathrm{I_{Neu}}$: The neutral-hadron isolation is computed from a sum of neutral-hadron p_{T} within a cone of $\Delta\mathrm{R} < 0.3$ of the photon candidate.

- I_{γ}: The photon isolation is computed from a sum of photon p_{T} within a cone of $\Delta\mathrm{R} < 0.3$ of the photon candidate.

The isolation variables employ footprint removal, so that the effect of the photon candidate is minimized in the summations. In each event, pileup interactions can produce additional objects which can fall within the isolation cone of the photon. These objects then contribute their p_{T} to the isolation sums mentioned above. The isolation variables are therefore corrected by the mean p_{T} density of each event to mitigate the effect of pileup [67].

4.5 Jet reconstruction

Collisions at the LHC, unsurprisingly, primarily produce quarks and gluons. These are not observable on their own because of color confinement, however, they do create collimated showers of hadrons. Collections, or jets, of charged and neutral hadrons produce tracks and calorimeter deposits. Jets are reconstructed by clustering the PF candidates in an event using the anti-k_{T} algorithm [68] with a distance parameter R of 0.4 as implemented in FastJet [69]. In the anti-k_{T} algorithm generally conical jets are formed using a distance metric between particles which is determined by their $1/p_{\mathrm{T}}^2$ and physical separation. Particles with a distance greater than R from each other are clustered separately.

Jet momentum is calculated as the vector sum of all particle momenta clustered in the jet. Jets, like all other objects reconstructed in the CMS detector, need to be calibrated in order to have the correct energy scale. Energy corrections are essentially a scaling of the jet momentum that is dependent on p_{T}, η, and jet flavor. Jet energy corrections, composed of both energy scale and energy

resolution corrections, are applied to all jets to correct for energy coming from pileup events, detector response, and residual data-simulation discrepancies. The procedure for 13 TeV data taking and its performance are akin to that of the 8 TeV data taking period, which is detailed in Ref. [70].

Mismeasured high-p_{T} jets can produce a $\vec{p}_{\mathrm{T}}^{\,\mathrm{miss}}$ that is aligned in the same direction as the jet. Therefore, jets are used in the Mono-h analysis as a way to clean events with possibly mismeasured $p_{\mathrm{T}}^{\mathrm{miss}}$. All jets with $p_{\mathrm{T}} > 50$ GeV and that fall with $|\eta| < 4.7$ are used in the Mono-h analysis if they pass a loose set of selection requirements. The selection is based on the fraction and number of charged, neutral, and electromagnetic constituents in the jet, and designed to remove jets originating from calorimeter noise. A description of the criteria and efficiency for the 2015 data set is found in Ref. [71]. The criteria for the 2016 data set is comparable. The selection is roughly 98% efficient at identifying jets in an enriched dijet data set. In a minimum-bias sample, the jet background rejection is greater than 90%.

4.6 Missing transverse momentum reconstruction

The missing transverse momentum vector ($\vec{p}_{\mathrm{T}}^{\,\mathrm{miss}}$), with magnitude $p_{\mathrm{T}}^{\mathrm{miss}}$, is the negative vector sum of the p_{T} of all PF candidates in a pp collision event as depicted in Fig. 4.4. Because $p_{\mathrm{T}}^{\mathrm{miss}}$ is inferred from the p_{T} of the physics objects in an event, it is highly dependent on the reconstruction of these objects. The CMS Collaboration has several algorithms used to estimate $p_{\mathrm{T}}^{\mathrm{miss}}$ [72]. The one used in this analysis does not solely rely on the original PF jet p_{T} in the $\vec{p}_{\mathrm{T}}^{\,\mathrm{miss}}$ calculation. Instead, the jets' p_{T} in the $\vec{p}_{\mathrm{T}}^{\,\mathrm{miss}}$ calculation are corrected by their jet

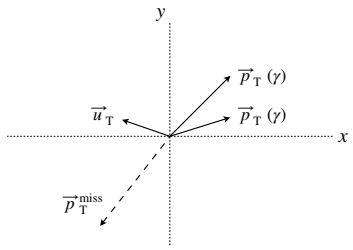

Figure 4.4: Illustration of object momentum and the resulting $\vec{p}_{\mathrm{T}}^{\,\mathrm{miss}}$ in the transverse plane for a signal-like event where two photon objects point right and the vector $\vec{u}_{\mathrm{T}}$ denotes the vector sum of all other particles reconstructed in the event.

energy corrections [70] as described in the previous section. The $\vec{p}_{\mathrm{T}}^{\,\mathrm{miss}}$ becomes:

$$\vec{p}_{\mathrm{T}}^{\,\mathrm{miss}} = \mathrm{PF}\ \vec{p}_{\mathrm{T}}^{\,\mathrm{miss}} - \sum_{jets}(\vec{p_{\mathrm{T}}}_{,jet}^{\,\mathrm{corr}} - \vec{p_{\mathrm{T}}}_{,jet}). \tag{4.3}$$

In general, anomalous large $p_{\mathrm{T}}^{\mathrm{miss}}$ in an event can be caused by uninteresting causes like detector noise, cosmic rays, and beam-halo particles. Events of these nature are not well-modeled in simulation. Filters that use timing, pulse-shape and topological information are applied to remove these events from the data set. The filters identify better than 85% of spurious high-$p_{\mathrm{T}}^{\mathrm{miss}}$ events with a mistagging rate less than 0.1%. More information about these filters can be found in Ref. [72].

The reconstructed $\vec{p}_{\mathrm{T}}^{\,\mathrm{miss}}$ of the data has a sinusoidal modulation in the ϕ component, visible in Fig. 4.5. Possible causes of the modulation include anisotropic detector responses, inactive calorimeter cells, detector misalignment, and/or the displacement of the beam spot. It has also been noted that the modulation increases roughly linearly with the pileup. The Mono-h analysis depends on an accurate estimate of the $\vec{p}_{\mathrm{T}}^{\,\mathrm{miss}}$ direction. To reduce the amplitude of the ϕ modulation, the origin of the coordinate in the transverse momentum plane is shifted as a function of PF particle species and η. The corrected ϕ component and $p_{\mathrm{T}}^{\mathrm{miss}}$

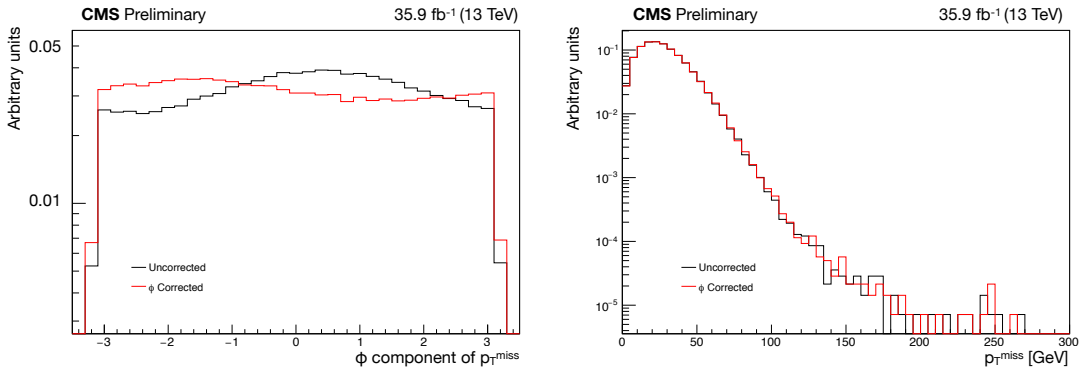

Figure 4.5: The ϕ component of the $\vec{p}_{\mathrm{T}}^{\,\mathrm{miss}}$ (left) and the magnitude $p_{\mathrm{T}}^{\mathrm{miss}}$ (right) for data before (black) and after (red) the correction.

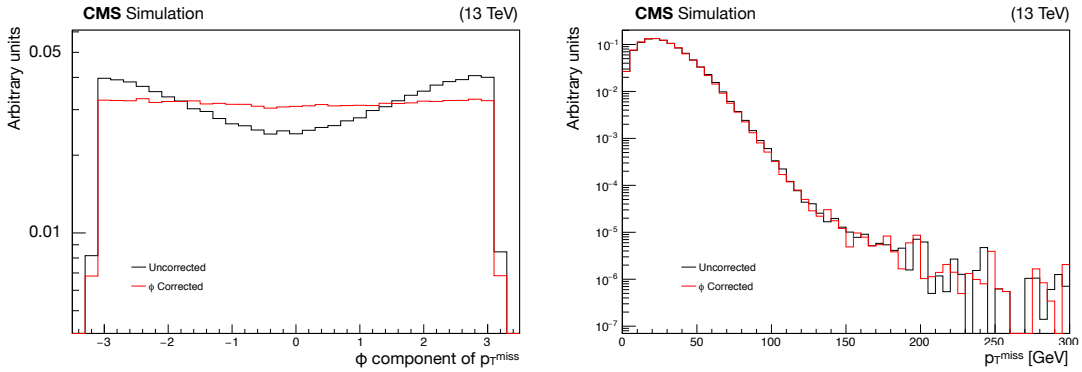

Figure 4.6: The ϕ component of the $\vec{p}_{\mathrm{T}}^{\,\mathrm{miss}}$ (left) and the magnitude $p_{\mathrm{T}}^{\mathrm{miss}}$ (right) for simulated events before (black) and after (red) the correction.

magnitude are shown for data in Fig. 4.5 and for simulation in Fig. 4.6.

CHAPTER 5

MONO-H($\gamma\gamma$) ANALYSIS

A search for particle dark matter particles produced in association with a Higgs boson decaying to two photons is presented here. Two benchmark models that yield this signal were previously described in Sec. 2.5. The primary sources of background events are discussed in Sec. 5.1. Then in Sec. 5.2 the observed data set is presented. Photon identification, optimization of the event selection, and the ultimate event selection criteria are described in Sec. 5.3, Sec. 5.4, and Sec. 5.5, respectively. The estimation of the background, which is primarily extrapolated from the data, is detailed in Sec. 5.7. A discussion of the systematic uncertainties affecting the analysis are presented in Sec. 5.8. The statistical treatment of the data is detailed in Sec. 5.9. Section 5.10 shows the results of the Mono-h search including the interpretation in terms of the benchmark signal models. Section 5.11 summarizes a similar search at ATLAS. Finally, a summary of the analysis is presented in Sec. 5.12.

5.1 Background sources

This search looks for a final state that is composed of two photons and a momentum imbalance registered as $p_{\mathrm{T}}^{\mathrm{miss}}$. The final state of the $\mathrm{h} + \mathrm{DM}$ signal has many standard model background sources. These backgrounds fall into two categories: resonant background from events where there is a SM Higgs boson that decays to two photons, and nonresonant backgrounds. The nonresonant sources are expected to have a larger contribution to the total background, while the resonant backgrounds are in some cases irreducible.

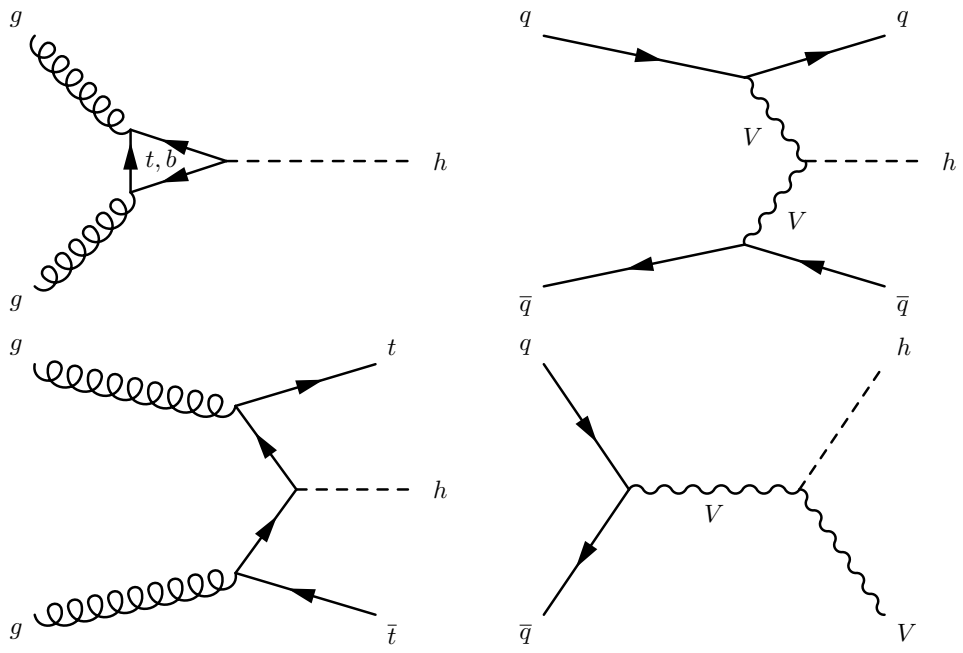

Figure 5.1: Feynman diagrams at LO for SM h production via ggh (upper left), VBF (upper right), $\mathrm{t\bar{t}h}$ (lower left), and Vh (lower right).

5.1.1 Resonant backgrounds

There are four prominent Higgs boson production mechanisms at the LHC: i. gluon-gluon fusion (ggh), ii. vector boson fusion (VBF), iii. associated production with top quarks ($\mathrm{t\bar{t}h}$), and iv. associated production with a vector boson (Vh) where the vector boson is either a Z or W boson. Example leading order diagrams for each of these production mechanisms are shown in Fig. 5.1. Of these production mechanism, the SM Vh production is an irreducible background for this analysis if $\mathrm{Z} \to \nu\nu$. The others can appear signal-like if they have large misreconstructed $p_{\mathrm{T}}^{\mathrm{miss}}$.

Monte Carlo (MC) simulated samples of SM h production are generated at next-to-leading order (NLO) using MADGRAPH5_aMC@NLO v2.2.2 [33]. As in the signal samples, the decay of the Higgs boson is simulated by PYTHIA using

the CUETP8M1 underlying event tune parameter set [73]. The parton distribution functions (PDFs) are taken from the NNPDF3.0 set [74]. The predicted SM cross sections are calculated at NLO by the LHC Higgs Cross Section working group for each production mechanism [75]. The SM h cross sections are summarized in Table 5.1.

Table 5.1: Theoretical SM Higgs boson production cross sections [75].

Production mode	Cross section [pb]
ggh	48.58
VBF	3.782
$\mathrm{t\bar{t}h}$	0.5071
Vh	2.257

The resonant background simulated samples, in addition to being used for optimizing the event selection, are used in the background yield estimation. This is described in more detail in Sec. 5.7.1. In contrast, the nonresonant backgrounds, described next, although also used to choose the optimal event selection, are not used in the background estimation. Instead, the nonresonant distribution is taken from the observed data. This process is detailed in Sec. 5.7.2.

5.1.2 Nonresonant backgrounds

The dominant nonresonant backgrounds for this analysis are events with real or mismeasured $p_{\mathrm{T}}^{\mathrm{miss}}$ and two photons that happen to have an invariant mass close to the mass of the SM Higgs boson. The largest contribution to the nonresonant background are $\gamma\gamma$ events followed by $\gamma + \mathrm{jet}$ and QCD multijet events.

Two real photons can primarily be produced by either quark-antiquark annihilation (Born processes) or gluon-gluon fusion (box processes). These pro-

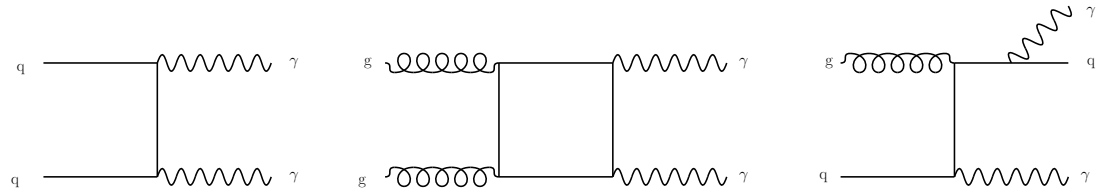

Figure 5.2: Born (left), box (center), and bremsstrahlung (right) processes of nonresonant diphoton production.

duction mechanisms are shown in Fig. 5.2. The simulated $\gamma\gamma$ event sample is generated at LO with SHERPA v2.2.2 [76]. In $\gamma + \mathrm{jet}$ and multijet events, a final state jet is reconstructed as a photon. These samples are modeled at LO with PYTHIA.

Additional nonresonant backgrounds arise from various electroweak processes. These include: single top, $\mathrm{t\bar{t}}$, W boson, or Z boson production in association with one or two photons. Drell-Yan (DY) production where the Z boson decays to pairs of electrons or muons can also be misidentified as an event with two photons. The DY and electroweak backgrounds are generated at NLO with MADGRAPH5_aMC@NLO v2.3.0.

5.2 Observed data set

The search for $\mathrm{h} + \mathrm{DM}$ is performed on pp collision data at a center-of-mass energy $\sqrt{\mathrm{s}} = 13\ \mathrm{TeV}$ and a bunch spacing of 25 ns. The data are collected at the CMS detector in 2015 and 2016. The 2015 data set correspond to an integrated luminosity of 2.2 fb^{-1}. The 2016 data set correspond to an integrated luminosity of 35.9 fb^{-1}. The data included in the analysis fulfill all quality criteria for all of the subcomponents of the CMS detector.

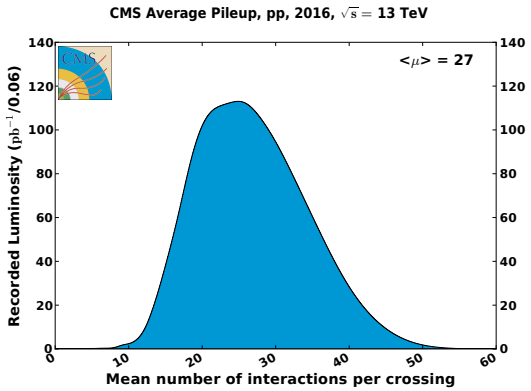

Figure 5.3: Average number of vertices in the 2016 data set [41].

This thesis will focus primarily on the analysis of the 2016 data [29,77], which is more sensitive to DM signals because of the increased size of the data set. The 2015 analysis [28, 78], which is part of the first CMS paper on $\mathrm{h} + \mathrm{DM}$, is described briefly in Appendix A. It is included to show an alternative way of doing the background estimation and signal extraction.

During the 2016 run, the average pileup was 27 simultaneous pp events at the CMS experiment. This is shown in the number of vertices per event in Fig. 5.3. Minimum-bias collision events generated with PYTHIA are added to the simulated samples to mimic the effects of pileup. This generation of overlapping pp collisions is necessary, but does not completely agree with the observed pileup distribution. Therefore, the simulated samples are reweighted to match the number of vertices distribution observed in the data.

The data that is stored and processed in this analysis are selected by the Level-1 and High-Level Triggers. In general, if an event with a photon passes the L1 trigger requirements, local ECAL information about the seed photon is unpacked by the HLT. The HLT reads the information in a rectangle of $\Delta\eta \times \Delta\phi = 0.14 \times 0.4$ around the L1 seed. The HLT then runs a clustering algorithm

on this particular segment of interest and decides if the events are accepted.

For both the 2015 and 2016 data set, similar triggers are used to select the data. The primary difference being that the 2016 trigger has a slightly looser mass requirement than that of the 2015 trigger. At L1, a diphoton trigger is used that has transverse energy thresholds of 22 and 15 GeV for the p_{T} leading and subleading photons. At HLT, these thresholds are raised to 30 and 18 GeV, respectively. The events are filtered into two categories based on their R_9 values and based on if they fall in the barrel (EB) or endcap (EE). Loose photon identification criteria [1] based on the cluster shower shape, isolation requirements, and a selection on the ratio of hadronic-to-electromagnetic energy deposits are applied on the candidate photons. The 2015 (2016) trigger selection at HLT has an additional requirement that the diphoton invariant mass $m_{\gamma\gamma}$ is greater than 95 (90) GeV. Full HLT selection requirements for the 2016 trigger are given in Table 5.2. The effect of the trigger is also modeled and applied to the simulated samples.

Table 5.2: Trigger selection requirements for the 2016 trigger.

	$\mathrm{H/E}$	$\sigma_{\eta\eta}$	R_9	I_{γ}	I_{Ch}
EB; $R_9 > 0.85$	< 0.12	–	> 0.5	–	–
EB; $R_9 \leq 0.85$	< 0.12	< 0.015	> 0.5	$< (6.0 + 0.012 p_{\mathrm{T}})$	$< (6.0 + 0.002 p_{\mathrm{T}})$
EE; $R_9 > 0.90$	< 0.1	–	> 0.8	–	–
EE; $R_9 \leq 0.90$	< 0.1	< 0.035	> 0.8	$< (6.0 + 0.012 p_{\mathrm{T}})$	$< (6.0 + 0.002 p_{\mathrm{T}})$
Other trigger requirements					
$m_{\gamma\gamma} > 90$ GeV	HLT seeded $p_{\mathrm{T}} > 30$ GeV		HLT unseeded $p_{\mathrm{T}} > 18$ GeV		

The efficiency for the data to pass the trigger selection is computed using the tag-and-probe method [79]. The tag-and-probe method is a generic way to measure efficiency by exploiting diobject resonances, in the case here the dielectron invariant mass peak in a $\mathrm{Z} \to \mathrm{ee}$ resonance is utilized. The "tag" object has a

[1] Reminder, photon identification variables are defined in Sec. 4.4.

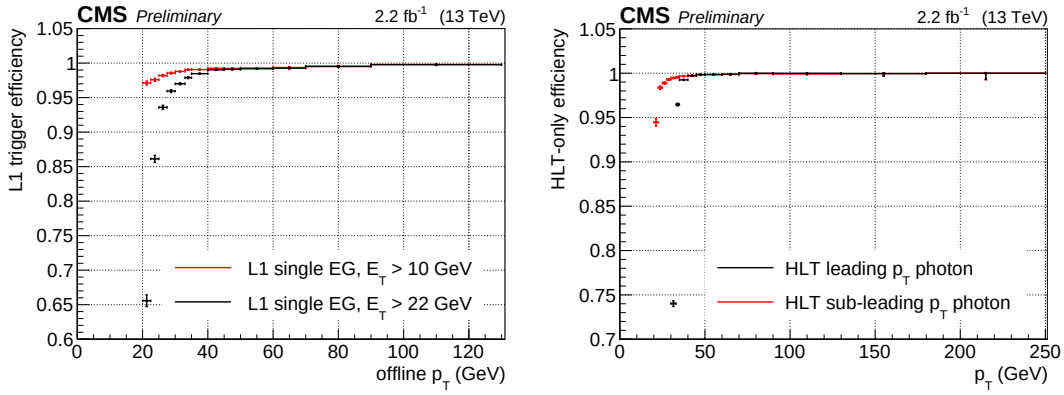

Figure 5.4: Level-1 (left) and high-level (right) trigger efficiency as a function of p_{T} for leading (black) and subleading (red) photons in the 2015 trigger [80].

set of very tight identification requirements applied (the misidentification rate of the tag should be less than 1%). The other object, the "probe", is selected by pairing these objects with the tags such that the invariant mass is consistent with a $\mathrm{Z} \to \mathrm{ee}$ resonance. The efficiency is calculated from the number of probes passing the desired criteria divided by the total number of probes. Generally the number of events in each case is extracted by fitting the resonance peak.

The trigger efficiency, extracted using the tag-and-probe method, as a function of photon p_{T} is shown for the 2015 data set in Fig. 5.4 [80]. Similar performance is observed for the 2016 data set. The observed efficiency is 98%, and the efficiency reaches the plateau at about 40 GeV for the seeded leg.

As already hinted, data selected with a single electron or photon are also used in this analysis. This data set is used for estimating the aforementioned trigger efficiency and for evaluating scale factors between data and simulation that will be detailed later. This "Single Electron" data set passes a trigger with a 27 GeV electron p_{T} threshold. The electron falls in $\eta < 2.1$ and passes other tight identification criteria.

5.3 Photon identification

The photons that enter the Mono-h analysis are required to fall within the fiducial range of the ECAL ($|\eta| < 2.5$) excluding the gap between $1.44 < |\eta| < 1.57$. A loose selection, detailed in Table 5.3, is applied to identify photons for the Mono-h analysis. This selection has an estimated 90% efficiency for identifying photons, while having an 82% background-rejection rate.

Table 5.3: Loose working point selection for barrel and endcap photon identification. A conversion-safe electron veto is also applied in both regions.

Variable	Barrel selection	Endcap selection
H/E	< 0.0597	< 0.0481
$\sigma_{\eta\eta}$	< 0.01031	< 0.03013
$\mathrm{I_{Ch}}$ [GeV]	< 1.295	< 1.011
$\mathrm{I_{Neu}}$ [GeV]	$< 10.910 + 0.0148p_{\mathrm{T}}$ $+ 0.000017p_{\mathrm{T}}^2$	$< 5.931 + 0.0163p_{\mathrm{T}}$ $+ 0.000014p_{\mathrm{T}}^2$
(if $\Delta\mathrm{R} > 0.3$) I_γ [GeV]	$< 3.630 + 0.0047p_{\mathrm{T}}$	$< 6.641 + 0.0034p_{\mathrm{T}}$

In addition to these criteria, a conversion-safe electron veto is applied to reject only prompt electrons. This means any event is vetoed if it contains charged particles that have a hit in the inner most layer of the pixel detector that is unmatched to a conversion vertex that points to the photon cluster. This selection helps to reduce the Drell-Yan background contribution, while maintaining a practically 100% efficiency for signal events.

The dependency on the $\Delta\mathrm{R}$ in the photon isolation is a unique component for this analysis that was added to optimize the photon identification for signals with Lorentz-boosted topologies. For signal models with high-mass mediators, the Higgs boson gets a momentum boost. When the boosted Higgs boson decays, the outgoing photons are produced collinearly and hit the ECAL close to each other. Consequently, the $\Delta\mathrm{R}$ difference between the two photons is small,

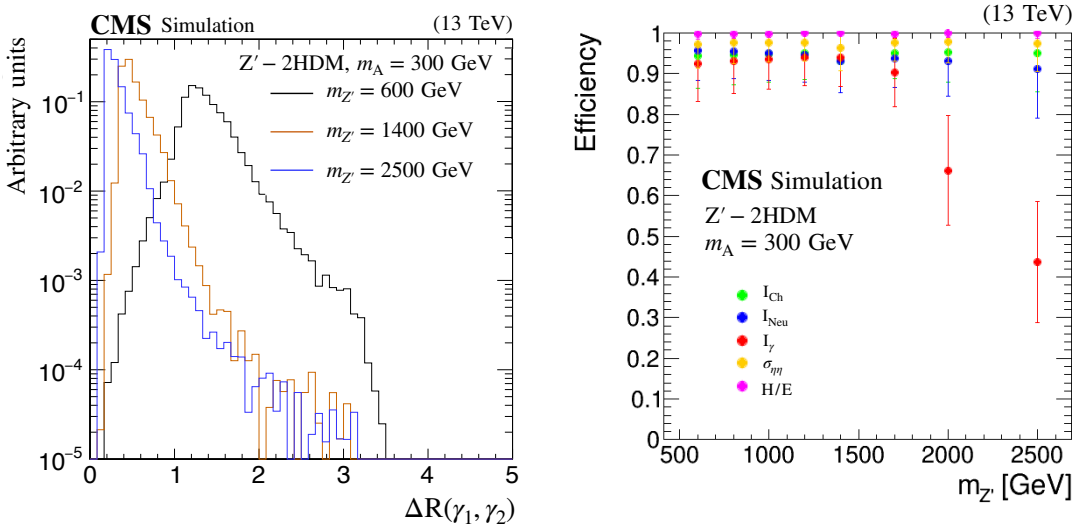

Figure 5.5: The ΔR of the two photons for select signal points (left), and the efficiency of the Z′-2HDM signals to pass the selection on each variable of the photon identification as a function of $m_{Z'}$ (right).

as seen in Fig. 5.5 (left). When the photons overlap in this way, there are large contributions from one photon to the photon isolation sum of the other, this causes the photon identification efficiency to drop. For the Z′-2HDM, this is seen in high $m_{Z'}$ signals, as shown in Fig. 5.5 (right). In order to maintain efficiency to signals with such topologies, the requirements on I_γ are not applied for photons that fall within $\Delta R < 0.3$ of each other.

A tag-and-probe method, described earlier for the trigger efficiency measurement, is also used here to understand any potential difference in photon identification efficiency between data and simulated events. The identification selection is applied to the Single Electron data set (mentioned in Sec. 5.2). The efficiency for data and simulated events to pass the criteria is shown in Fig. 5.6. Also shown is the ratio of data and simulated event efficiency. The difference in these efficiencies, shown in Fig. 5.7 are taken as scale factors that are applied to the simulated events.

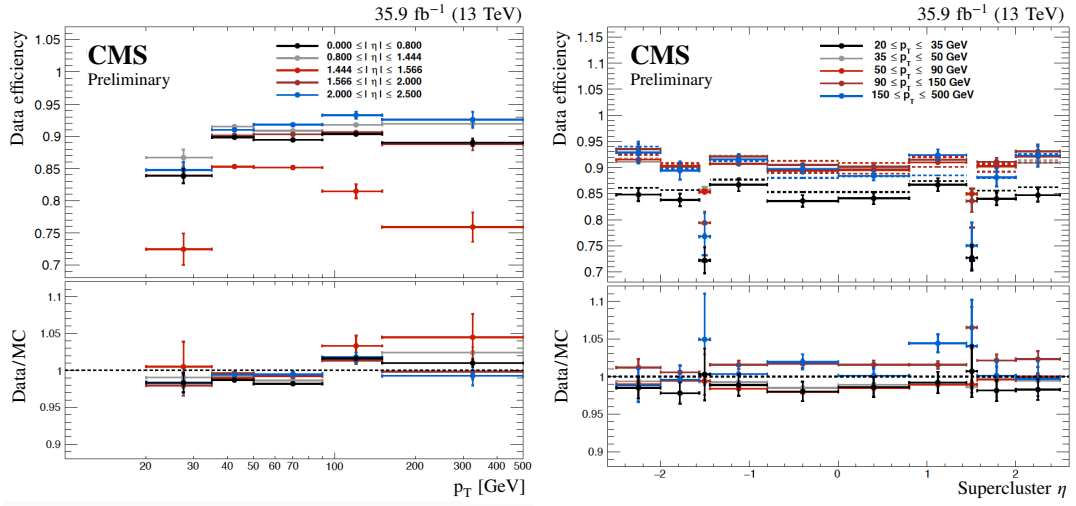

Figure 5.6: Photon identification efficiency as a function of p_{T} (left) and η (right) for data (lines) and simulated events (dashed lines). The lower pad shows the ratio of data to simulated events efficiency.

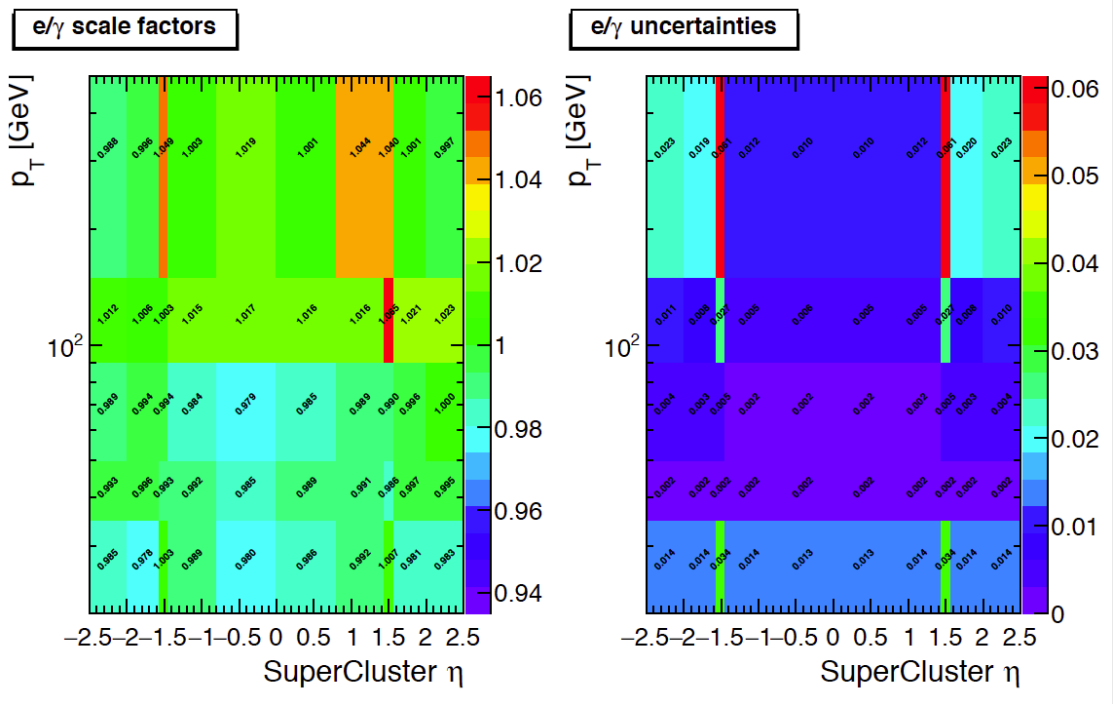

Figure 5.7: Scale factors (left) and uncertainties on the scale factors (right) for the photon identification.

5.4 Selection optimization

The criteria for event selection was optimized using signal and background simulated events. The Punzi significance [81] is a frequentist definition of signal sensitivity and was maximized to find the optimal selection criteria for the analysis. The Punzi significance S is calculated for the number of standard deviations wanted for detection (a) using the signal selection efficiency ϵ and the number of background events B. The significance is defined as:

$$S = \frac{\epsilon}{(a/2 + \sqrt{\mathrm{B}})}. \tag{5.1}$$

Setting $a = 5$, the Punzi significance is studied for the variables: $p_{\mathrm{T}1}/m_{\gamma\gamma}$, $p_{\mathrm{T}2}/m_{\gamma\gamma}$, $p_{\mathrm{T}}^{\mathrm{miss}}$, and $p_{\mathrm{T}\gamma\gamma}$. Note, that $p_{\mathrm{T}1}/m_{\gamma\gamma}$ and $p_{\mathrm{T}2}/m_{\gamma\gamma}$ are used instead of $p_{\mathrm{T}1}$ and $p_{\mathrm{T}2}$, respectively, since these better preserve the shape of the $m_{\gamma\gamma}$ distribution which is ultimately used for the background estimation.

Two dimensional scans of Punzi significance for various selection criteria are shown in Fig. 5.8. The optimal selection for the high-$p_{\mathrm{T}}^{\mathrm{miss}}$ region was chosen based on studies of the Z′-2HDM signal with $m_{\mathrm{A}} = 300\ \mathrm{GeV}$ and $m_{\mathrm{Z}'} = 600\ \mathrm{GeV}$. The low-$p_{\mathrm{T}}^{\mathrm{miss}}$ region selection was optimized using the baryonic Z′ model with $m_{\mathrm{DM}} = 1\ \mathrm{GeV}$ and $m_{\mathrm{Z}'} = 10\ \mathrm{GeV}$. These were the lightest mass points available at the time and offered the softest $p_{\mathrm{T}}^{\mathrm{miss}}$ spectra for each model.

5.5 Event Selection

Preselected photons are required to pass general event preselection criteria, summarized in Tab. 5.4. The events are then split into a high-$p_{\mathrm{T}}^{\mathrm{miss}}$ category

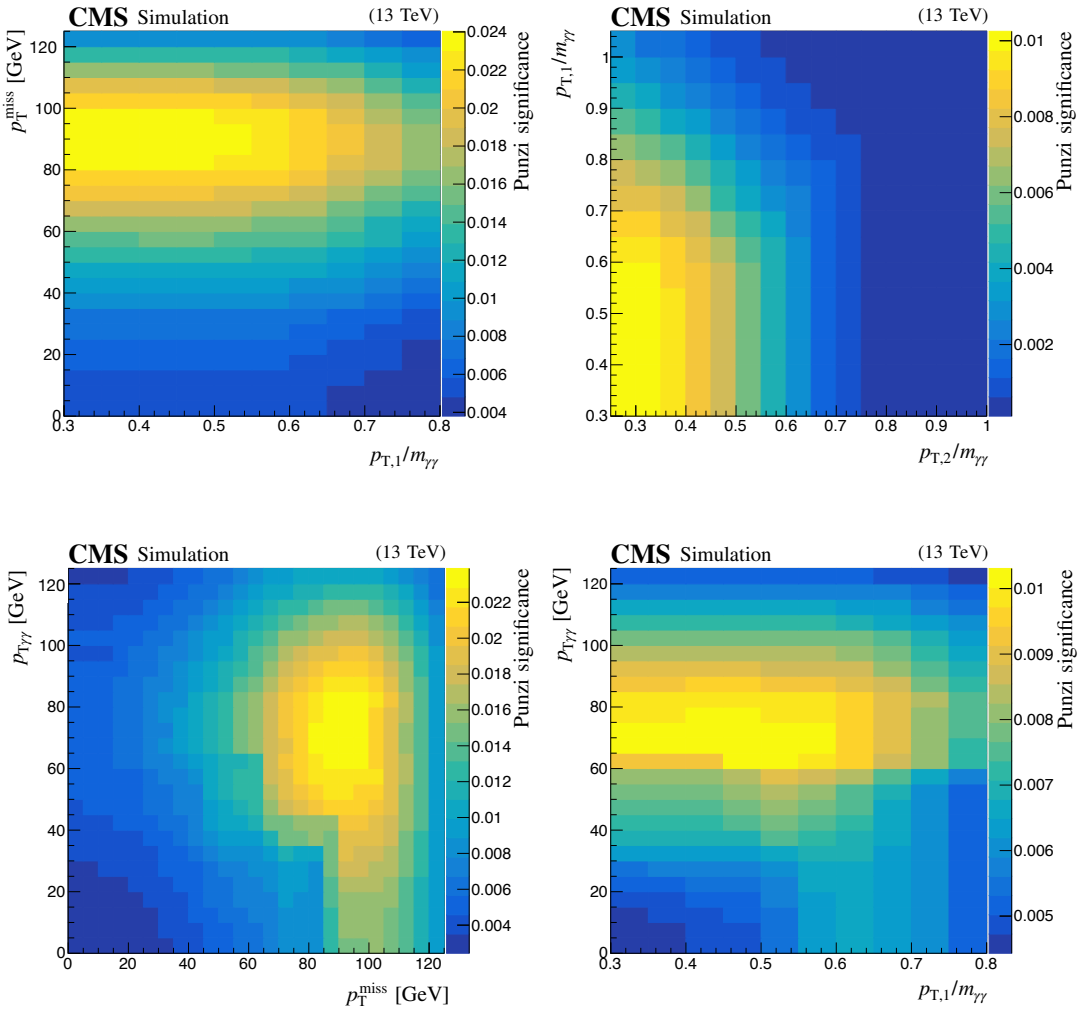

Figure 5.8: Scans of Punzi significance for the baryonic Z′ model.

($p_{\mathrm{T}}^{\mathrm{miss}} \geq 130$ GeV) and a low-$p_{\mathrm{T}}^{\mathrm{miss}}$ category ($50 < p_{\mathrm{T}}^{\mathrm{miss}} < 130$ GeV). The kinematic selection applied, chosen by the optimized selection mentioned above, is shown in Table 5.5. Additionally, events are rejected if they have three or more jets each with p_{T} above 30 GeV to reject multijet backgrounds.

Two topological requirements are also applied. A misreconstructed high p_{T} jet can cause a large amount of nearly collinear $p_{\mathrm{T}}^{\mathrm{miss}}$. To protect against events of this nature, events are removed if there are highly energetic jets collinear to

Table 5.4: Event preselection requirements.

Variable	Selection criteria
$p_{\mathrm{T}1}$	> 30 GeV
$p_{\mathrm{T}2}$	> 20 GeV
$p_{\mathrm{T}1}/m_{\gamma\gamma}$	> 0.33
$p_{\mathrm{T}2}/m_{\gamma\gamma}$	> 0.25
$m_{\gamma\gamma}$	$\geq 100, \leq 300$ GeV

Table 5.5: Kinematic requirements for the low- and high-$p_{\mathrm{T}}^{\mathrm{miss}}$ categories.

Variable	Low-$p_{\mathrm{T}}^{\mathrm{miss}}$ category	High-$p_{\mathrm{T}}^{\mathrm{miss}}$ category
$p_{\mathrm{T}}^{\mathrm{miss}}$	> 50 GeV, < 130 GeV	≥ 130 GeV
$p_{\mathrm{T}1}/m_{\gamma\gamma}$	> 0.45	> 0.5
$p_{\mathrm{T}2}/m_{\gamma\gamma}$	> 0.25	> 0.25
$p_{\mathrm{T}\gamma\gamma}$	> 75 GeV	> 90 GeV

the $\vec{p}_{\mathrm{T}}^{\,\mathrm{miss}}$ by requiring that $\min|\Delta\phi(\vec{p}_{\mathrm{jet}}, \vec{p}_{\mathrm{T}}^{\,\mathrm{miss}})|$ be greater than 0.5 for any jet with p_{T} above 50 GeV. Additionally, because it is expected for the signal that the $\vec{p}_{\mathrm{T}}^{\,\mathrm{miss}}$ is back-to-back with the Higgs boson, events must pass the selection $|\Delta\phi(\vec{p}_{\gamma\gamma}, \vec{p}_{\mathrm{T}}^{\,\mathrm{miss}})| > 2.1$.

5.6 Data-simulation comparison

To understand the performance of the data and how well it is modeled by the simulation, it is useful to compare the data with simulated events. The contribution from the simulation is summed for all background processes. In all of the distributions, the total number of simulated events are scaled to match the integral of the data. With selection applied on $p_{\mathrm{T}1}/m_{\gamma\gamma}$, $p_{\mathrm{T}2}/m_{\gamma\gamma}$, $p_{\mathrm{T}\gamma\gamma}$, and the veto on number of jets, distributions for the photon η, ϕ, and p_{T} are shown in Fig. 5.9, Fig. 5.10, and Fig. 5.11, respectively. Additionally, distributions are shown for $p_{\mathrm{T}\gamma\gamma}$ and $m_{\gamma\gamma}$ in Fig. 5.12. It is also useful to look at the topological

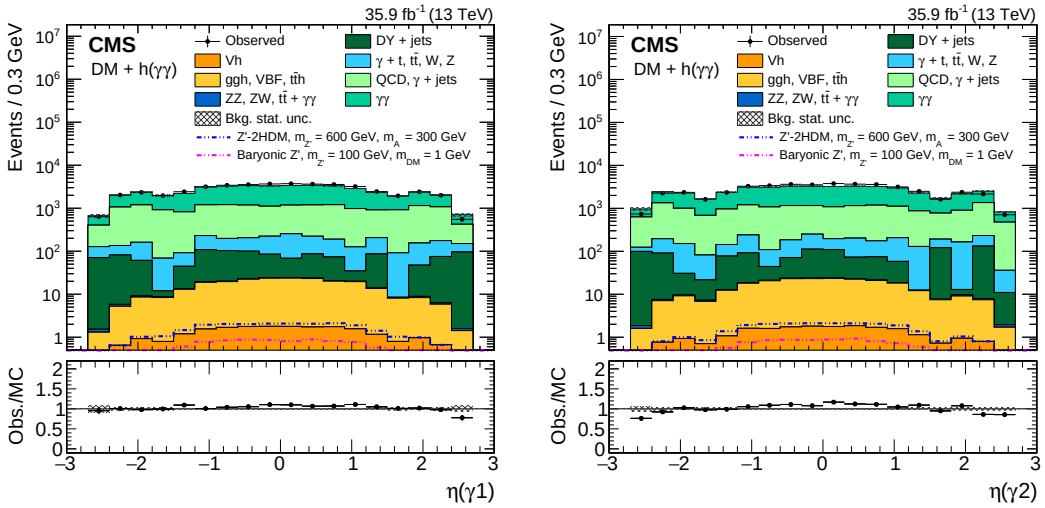

Figure 5.9: The η of the leading (left) and subleading (right) photon in data and simulation after selection on $p_{\mathrm{T}1}/m_{\gamma\gamma}$, $p_{\mathrm{T}2}/m_{\gamma\gamma}$, $p_{\mathrm{T}\gamma\gamma}$, and the veto on number of jets. The simulated events are scaled to match the integral of the data.

variables used in the analysis. The $\min|\Delta\phi(\vec{p}_{\mathrm{jet}}, \vec{p}_{\mathrm{T}}^{\,\mathrm{miss}})|$ is shown in Fig. 5.13 and the $|\Delta\phi(\vec{p}_{\gamma\gamma}, \vec{p}_{\mathrm{T}}^{\,\mathrm{miss}})|$ is shown in Fig. 5.14 with all other selection applied. For all of the abovementioned variables, the observed and simulated data have nearly identical distributions.

Likewise, after all other selection are applied, the $p_{\mathrm{T}}^{\mathrm{miss}}$ distribution is compared between the data and simulation in Fig. 5.15. Very good agreement is seen between the data set and the simulation. This is useful only as a validation that the data is well understood, since the nonresonant component of the background, which makes up the majority of the background, is estimated directly from the data.

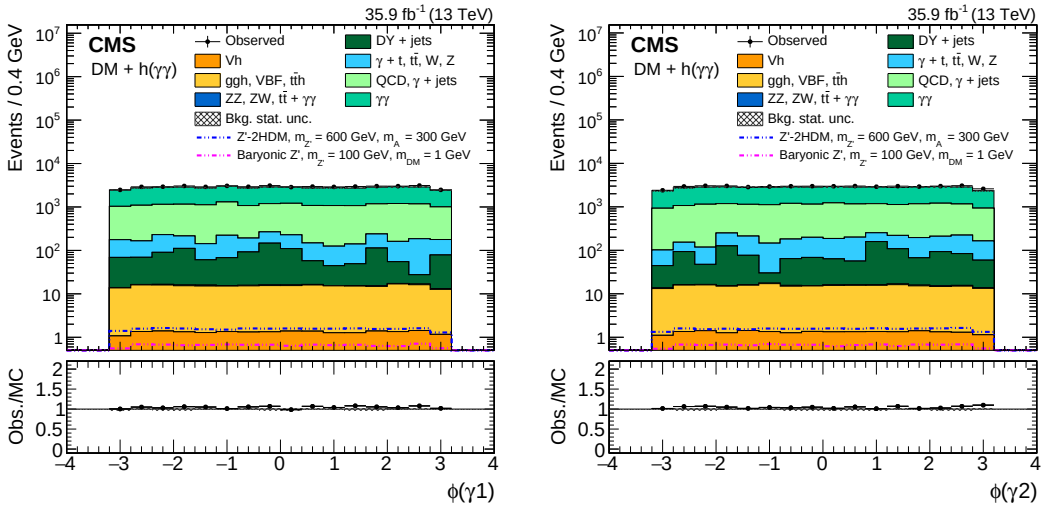

Figure 5.10: The ϕ of the leading (left) and subleading (right) photon in data and simulation after selection on $p_{\mathrm{T}1}/m_{\gamma\gamma}$, $p_{\mathrm{T}2}/m_{\gamma\gamma}$, $p_{\mathrm{T}\gamma\gamma}$, and the veto on number of jets. The simulated events are scaled to match the integral of the data.

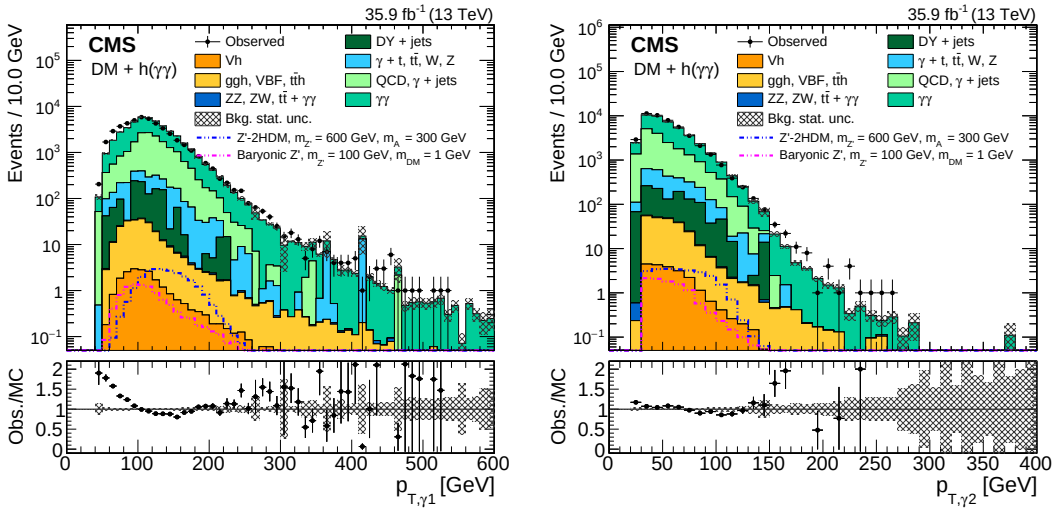

Figure 5.11: The p_{T} of the leading (left) and subleading (right) photon in data and simulation after selection on $p_{\mathrm{T}1}/m_{\gamma\gamma}$, $p_{\mathrm{T}2}/m_{\gamma\gamma}$, $p_{\mathrm{T}\gamma\gamma}$, and the veto on number of jets. The simulated events are scaled to match the integral of the data.

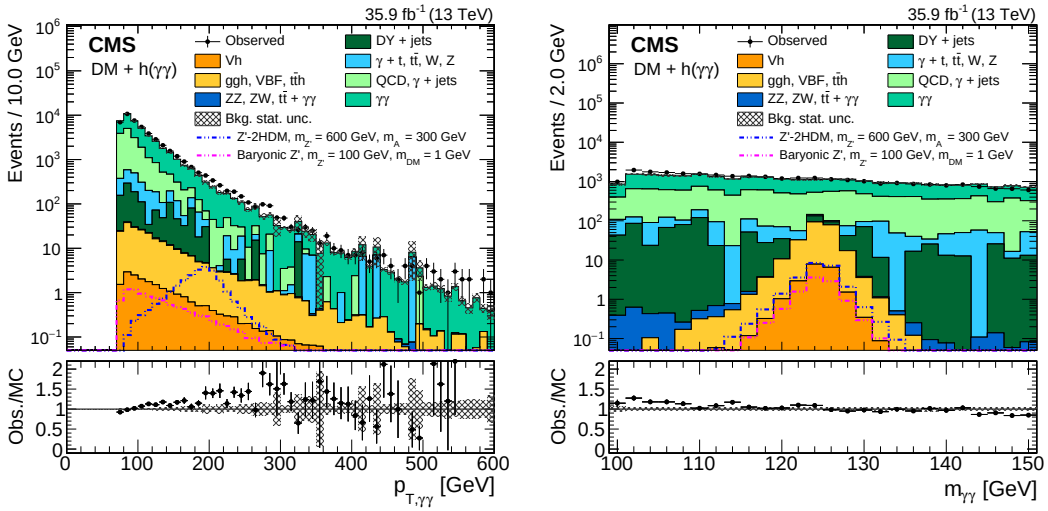

Figure 5.12: The $p_{\mathrm{T}\gamma\gamma}$ (left) and $m_{\gamma\gamma}$ (right) photon in data and simulation after selection on $p_{\mathrm{T}1}/m_{\gamma\gamma}$, $p_{\mathrm{T}2}/m_{\gamma\gamma}$, $p_{\mathrm{T}\gamma\gamma}$, and the veto on number of jets. The simulated events are scaled to match the integral of the data.

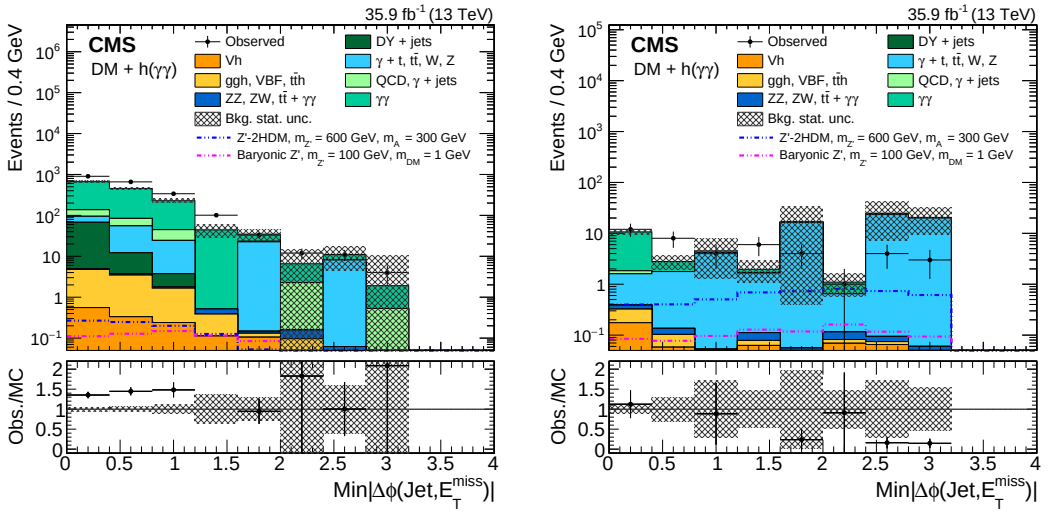

Figure 5.13: The $\min|\Delta\phi(\vec{p}_{\mathrm{jet}}, \vec{p}_{\mathrm{T}}^{\,\mathrm{miss}})|$ in data and simulation for the low-$p_{\mathrm{T}}^{\mathrm{miss}}$ (left) and high-$p_{\mathrm{T}}^{\mathrm{miss}}$ (right) after all selection except for the selection on this variable. The simulated events are scaled to match the integral of the data.

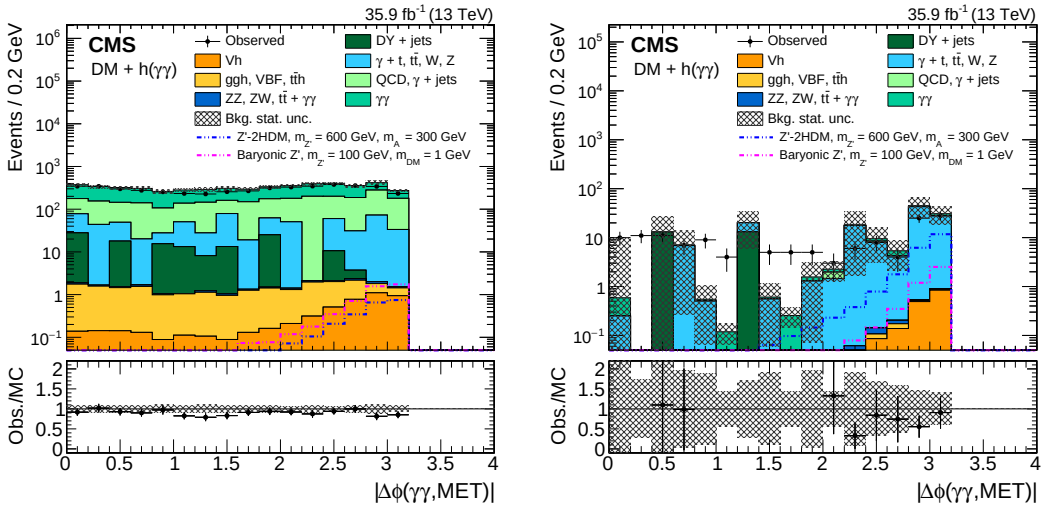

Figure 5.14: The $|\Delta\phi(\vec{p}_{\gamma\gamma}, \vec{p}_{\mathrm{T}}^{\,\mathrm{miss}})|$ in data and simulation for the low-$p_{\mathrm{T}}^{\mathrm{miss}}$ (left) and high-$p_{\mathrm{T}}^{\mathrm{miss}}$ (right) after all selection except for the selection on this variable. The simulated events are scaled to match the integral of the data.

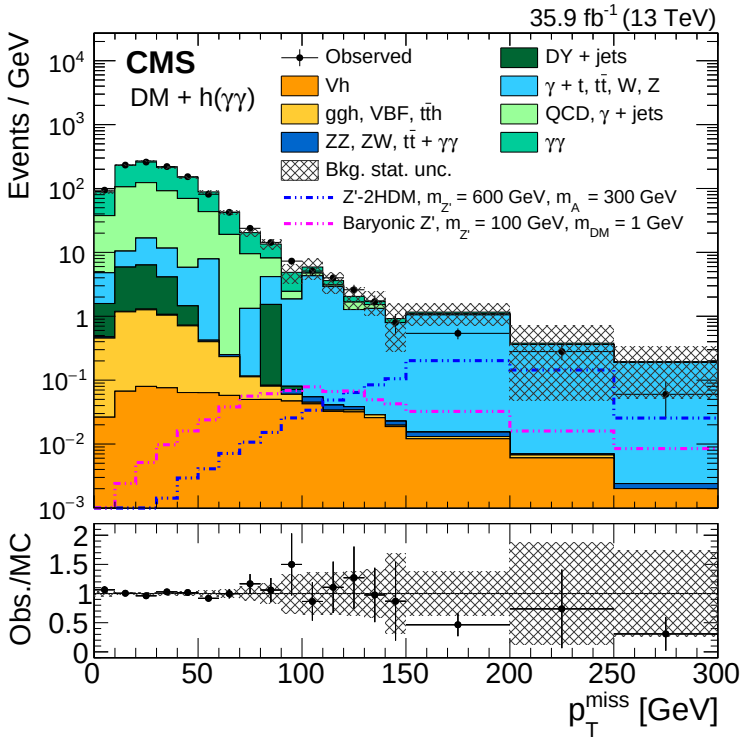

Figure 5.15: The $p_{\mathrm{T}}^{\mathrm{miss}}$ distribution in data and simulation after all selection is applied. Events with $p_{\mathrm{T}}^{\mathrm{miss}}$ below 50 GeV are not used in the analysis. The signals are shown with a cross section of 1 pb. The simulated events are scaled to match the integral of the data.

5.7 Background estimation and signal extraction

In order to extract an estimation of the background and signal contributions, a narrow resonance search is preformed. This method is similar to that of the SM Higgs boson diphoton analysis [63]. After applying all event selection, the diphoton invariant mass $m_{\gamma\gamma}$ between 105 and 180 GeV is fit with a probability density function (pdf) that is composed of signal and background shapes. The background pdf is composed of a resonant component (described in Sec. 5.7.1) and a nonresonant component (described in Sec. 5.7.2). The signal pdf and signal extraction are detailed in Sec. 5.7.3.

5.7.1 Resonant background pdf

The resonant background arises from the production of SM Higgs bosons decaying to two photons. This background contribution creates a peak in the $m_{\gamma\gamma}$ distribution. Both the signal and resonant backgrounds have a peak around $m_{\gamma\gamma} = 125\ \mathrm{GeV}$, as shown in Fig. 5.16. Therefore, any signal observed will be a peak in $m_{\gamma\gamma}$ on top of the resonant background peak. The contribution to the peak from the SM $\mathrm{h} \to \gamma\gamma$ backgrounds is estimated with simulated events. A mass distribution template taken from the simulated events is scaled to the SM Higgs boson production cross section at NLO. This template is included as a resonant component in the final background pdf.

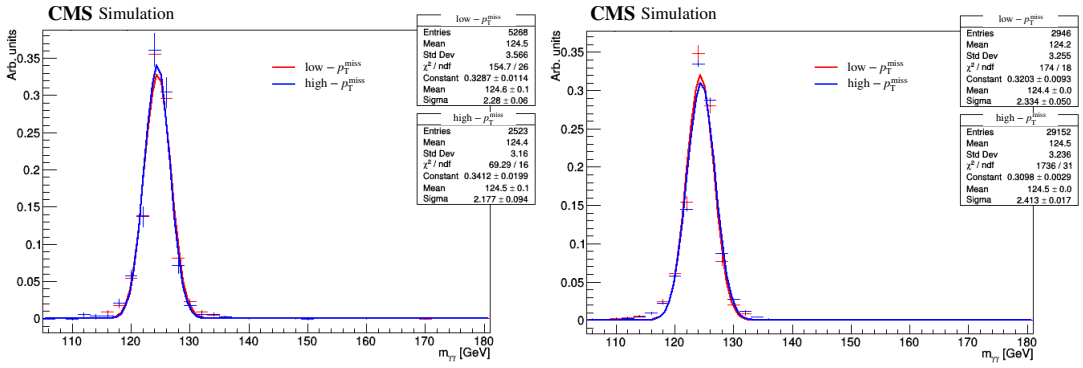

Figure 5.16: Shape of the $m_{\gamma\gamma}$ distribution for the SM Vh background (left) and for the Z′-2HDM signal (right) in simulated events in both the low-$p_{\mathrm{T}}^{\mathrm{miss}}$ (red) and high-$p_{\mathrm{T}}^{\mathrm{miss}}$ (blue) categories.

5.7.2 Nonresonant background pdf

The nonresonant background is mostly due to $\mathrm{pp} \to \gamma\gamma$ events and electroweak processes. Instead of estimating these contributions from the simulated events, the nonresonant background is estimated using the observed data. The diphoton $m_{\gamma\gamma}$ distribution in the data is fit, in each $p_{\mathrm{T}}^{\mathrm{miss}}$ category, with an analytic function that is used to model the nonresonant background. The true functional form of the background is obviously unknown, so the parametric model must be flexible enough to describe a variety of potential underlying functions. Also, using an incorrect model can lead to biases in the measured signal yield and artificially modify the sensitivity of the analysis. Three functions, commonly used in dijet [82] and diphoton [83] resonance searches, are considered as possible models for the nonresonant background pdf. The analytic functions considered

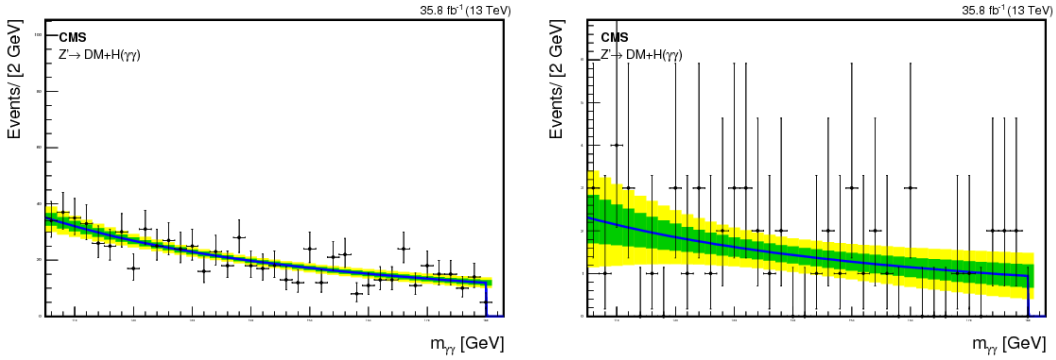

Figure 5.17: Example of the power law fit to the $m_{\gamma\gamma}$ distribution for one of the pseudo-experiments for the low-$p_{\mathrm{T}}^{\mathrm{miss}}$ (left) and high-$p_{\mathrm{T}}^{\mathrm{miss}}$ (right) categories.

are:

- Power law: ax^{-b} where a and b are free parameters
- Exponential times power law: $ax^{-b}e^{-c}$ with free parameters a, b, and c
- Dijet: $\frac{p_0(1-x)^{p_1}}{x^{p_2+p_3\log(x)}}$ where $x = m/\sqrt{s}$ and p_0, p_1, p_2, p_3 are free parameters

A detailed bias study is performed to choose which analytic function to use in the background estimation. A template of the $m_{\gamma\gamma}$ shape is built from simulated nonresonant events. This template is used to generate 1000 pseudo-experiments for each $p_{\mathrm{T}}^{\mathrm{miss}}$ category. For each pseudo-experiment, the number of events generated is equal to the number of events observed in data in that category. The resulting $m_{\gamma\gamma}$ distribution for each pseudo-experiment is fit with each of the analytic functions considered. An example of a fit for one of the pseudo-experiments is shown in Fig. 5.17. The same exercise is also repeated injecting a potential signal contribution.

The pull of the pseudo-experiment is defined as the difference in the number of simulated events N_{MC} and those predicted by the fit function N_{fit} divided by

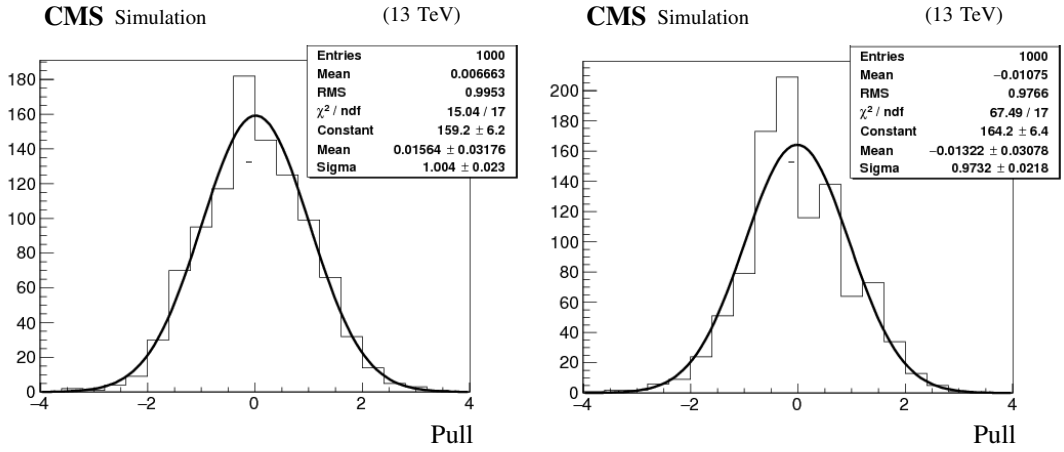

Figure 5.18: Pull of the fits for the power law function in the low-$p_{\mathrm{T}}^{\mathrm{miss}}$ (left) and high-$p_{\mathrm{T}}^{\mathrm{miss}}$ (right) categories.

the statistical uncertainties of the fit σ_{fit}:

$$pull = \frac{N_{fit} - N_{MC}}{\sigma_{fit}}. \tag{5.2}$$

For each analytic function tested, the pull of each pseudo-experiment is calculated. The distribution of pulls for the power law function is shown in Fig. 5.18. The bias (the median of the pulls) is shown for each of the analytic functions considered in Fig. 5.19. As seen there, the power law has the smallest bias. It is also the simplest of the functions considered. For these reasons, it is chosen as the background model.

If the bias is five times smaller than the statistical uncertainty in the number of fitted events, any potential bias from the choice of background model is considered negligible. This criteria is also satisfied for the power law function, therefore any systematic uncertainty in the bias from the chosen background fit function is neglected in this analysis.

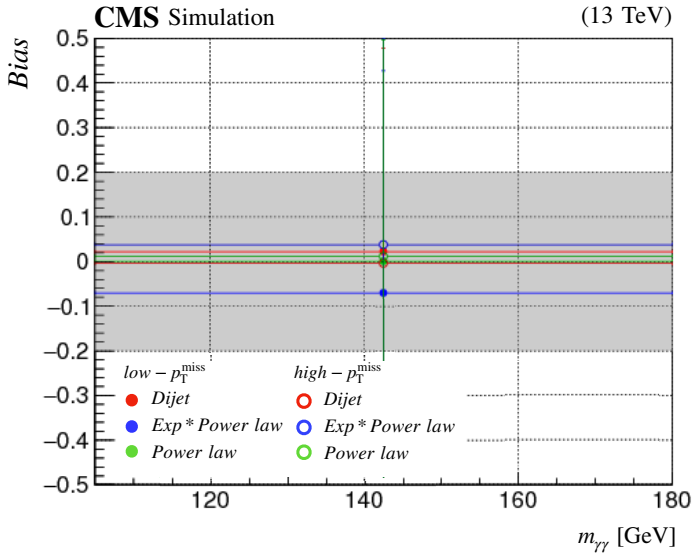

Figure 5.19: Bias for both the low-$p_{\mathrm{T}}^{\mathrm{miss}}$ (closed points) and high-$p_{\mathrm{T}}^{\mathrm{miss}}$ (open points) fit with the three functions: power law (green), exponential times power law (blue), and dijet function (red).

5.7.3 Signal extraction

The signal pdf is the $m_{\gamma\gamma}$ shape taken from the simulated signal samples weighted to the theoretical production cross section. The signal shape is dominated by the detector resolution and reconstruction response in the ECAL, therefore the shape is smeared as mentioned in Sec. 4.4. The signal shape for the Z′-2HDM signal is shown in Fig. 5.20.

To extract the signal yields, the $m_{\gamma\gamma}$ distribution observed in the data is fit with a signal plus background pdf. The background pdf is composed of the resonant and nonresonant background pdfs mentioned above. The background-only template for both $p_{\mathrm{T}}^{\mathrm{miss}}$ categories is shown in Fig. 5.21. An explanation of the maximum-likelihood fit and how the signal strength is estimated is given later in Sec. 5.9.

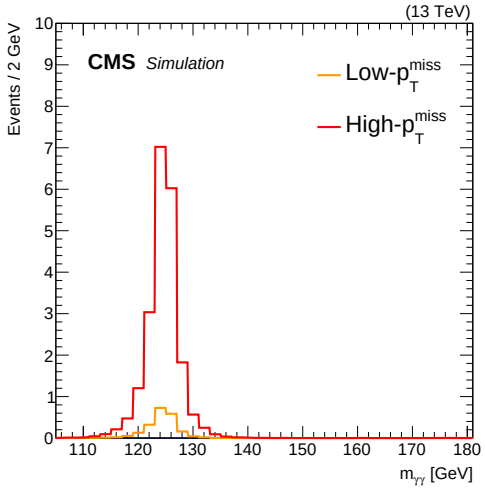

Figure 5.20: The Z′-2HDM signal shape in the low-$p_{\mathrm{T}}^{\mathrm{miss}}$ (orange) and high-$p_{\mathrm{T}}^{\mathrm{miss}}$ (red) categories.

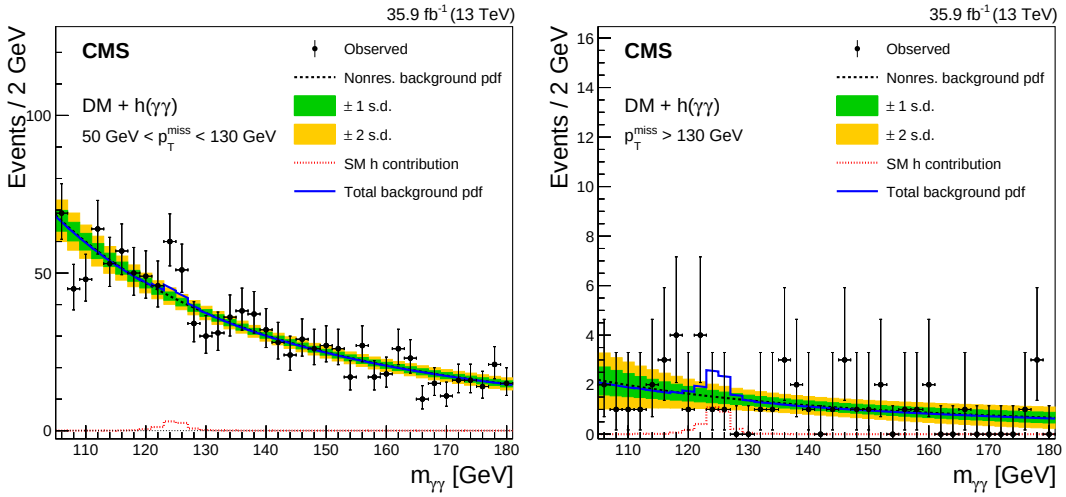

Figure 5.21: The background-only fit of the $m_{\gamma\gamma}$ distribution in the low-$p_{\mathrm{T}}^{\mathrm{miss}}$ (left) and high-$p_{\mathrm{T}}^{\mathrm{miss}}$ (right) categories. The fit is preformed with the sum of a power law function (dashed black) to describe the nonresonant background contribution, and a resonant shape (dashed red) taken from the simulation to account for the SM $\mathrm{h} \to \gamma\gamma$ contribution. The sum of these nonresonant and resonant shapes (solid blue) is used to estimate the total background in this analysis.

5.8 Systematic uncertainties

This section details the systematic uncertainties related to the Mono-h search. The systematic uncertainties can be split into theoretical and experimental sources of uncertainty. Additionally, the uncertainties can be separated between those that affect the overall expected yields and those that can change the expected shape. The uncertainties are summarized in Tab. 5.6.

Table 5.6: Systematic uncertainties affecting the resonant backgrounds. Uncertainties denoted with an asterisk are also applied to the signal.

	Change in yield or shape
Theoretical sources	
PDF	2–4%
Renorm. and fact. scale	0.3–9%
Higgs boson branching fraction *	1.73%
Cross section (ggh)	20%
Experimental sources	
Integrated luminosity *	2.5%
Trigger efficiency *	1.0%
Photon identification efficiency *	2.0%
Photon energy scale *	Shape
$p_{\mathrm{T}}^{\mathrm{miss}}$ energy scale (Vh and $\mathrm{t\bar{t}h}$) *	0.5%
$p_{\mathrm{T}}^{\mathrm{miss}}$ mismeasurement (ggh and VBF)	50%
$\Delta\phi$ selection efficiency (ggh and VBF)	1–4%

Theoretical uncertainties change the theoretical production cross section of the Higgs boson. Uncertainty in the underlying parton distribution function (PDF) are addressed using the recommendations of the PDF4LHC group [84]. The uncertainties arising from the renormalization and factorization scale are taken into effect using the recommendations from the LHC Higgs Cross Section working group [5]. These theoretical uncertainties modify the expected SM $\mathrm{h} \to \gamma\gamma$ yield by 0.3 to 9.0%. The Higgs boson branching fraction has a 1.73% systematic uncertainty [5] primarily originating from uncertainties on input pa-

rameters (like quark masses) in the calculation of the Higgs boson width. Based on the CMS measurement of the differential Higgs boson production cross section [85] for events with diphoton p_{T} above 70 GeV, an additional 20% uncertainty is included on the ggh cross section.

Several experimental sources of systematic uncertainties affect the Mono-h analysis. In general, these affect how well simulated samples model the data, and are therefore only relevant to simulated samples used in the signal extraction. An uncertainty of 2.5% is applied to the normalization of simulated samples to account for the uncertainty in the integrated luminosity measurement of the 2016 data set [86]. The trigger efficiency is measured for observed events as detailed in Sec. 5.2. The difference in trigger efficiency between observed and simulated events is taken as a systematic uncertainty of 1% [85]. Similarly, the difference in photon identification efficiency for observed and simulated events (shown earlier in Fig. 5.6) is taken as a 2% systematic uncertainty.

As mentioned in Sec. 4.4, the photon energy scale is corrected using $\mathrm{Z} \to \mathrm{ee}$ events. The uncertainty on the overall photon energy scale is primarily related to differences between electrons and photons. So it is evaluated by comparing $\mathrm{Z} \to \mathrm{ee}$ events and $\gamma\gamma$ events with $m_{\gamma\gamma} \approx 90$ GeV. The resulting difference of $\pm 0.5\%$ is applied as a shift in the $m_{\gamma\gamma}$ peak, as shown in Fig. 5.22. The variation of the $m_{\gamma\gamma}$ shape is included for the signal and resonant background templates in the final fit.

There are several systematic uncertainties in this analysis related to the use of the $p_{\mathrm{T}}^{\mathrm{miss}}$. Since $\vec{p}_{\mathrm{T}}^{\,\mathrm{miss}}$ is calculated from the vector sum of all other physics objects, the uncertainties on the energy and resolution of these objects affects the value of $p_{\mathrm{T}}^{\mathrm{miss}}$. Jet, photon, electron, muon, and tau energies can all modify the

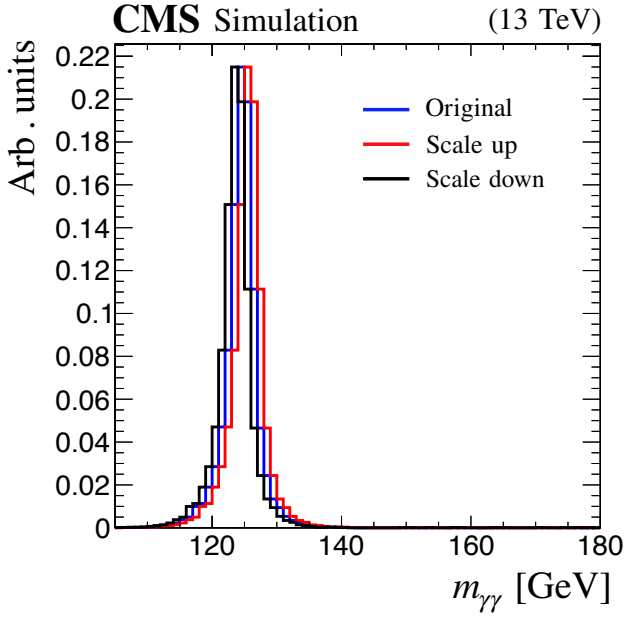

Figure 5.22: The nominal signal $m_{\gamma\gamma}$ shape (blue) and the $m_{\gamma\gamma}$ shape scaled up (red) and down (black).

$p_{\mathrm{T}}^{\mathrm{miss}}$. The corresponding uncertainty is calculated by shifting the reconstructed p_{T} of each object within the momentum scale and resolution uncertainties of that object and recalculating the $p_{\mathrm{T}}^{\mathrm{miss}}$ of the event [72]. Since this analysis does not rely on the shape of the $p_{\mathrm{T}}^{\mathrm{miss}}$ distribution, the change in the $p_{\mathrm{T}}^{\mathrm{miss}}$ distribution only changes the efficiency of events to pass the $p_{\mathrm{T}}^{\mathrm{miss}}$ selection. The largest difference in efficiencies is less than 0.5% and is taken as a systematic uncertainty on the normalization of simulated samples that have have true $p_{\mathrm{T}}^{\mathrm{miss}}$ (ie. signal samples, Vh and $\mathrm{t\bar{t}h}$ samples). This is completely negligible in the results. For simplicity, it is not included when the $\mathrm{h} \to \gamma\gamma$ analysis is combined with other Mono-h analyses with different decay channels.

On the other hand, for simulated samples that do not have real sources of $p_{\mathrm{T}}^{\mathrm{miss}}$ (i.e. the ggh and VBF samples), the fraction of events in the tail of the $p_{\mathrm{T}}^{\mathrm{miss}}$ region is not well understood. This uncertainty is quantified in a $\gamma + \mathrm{jet}$ control

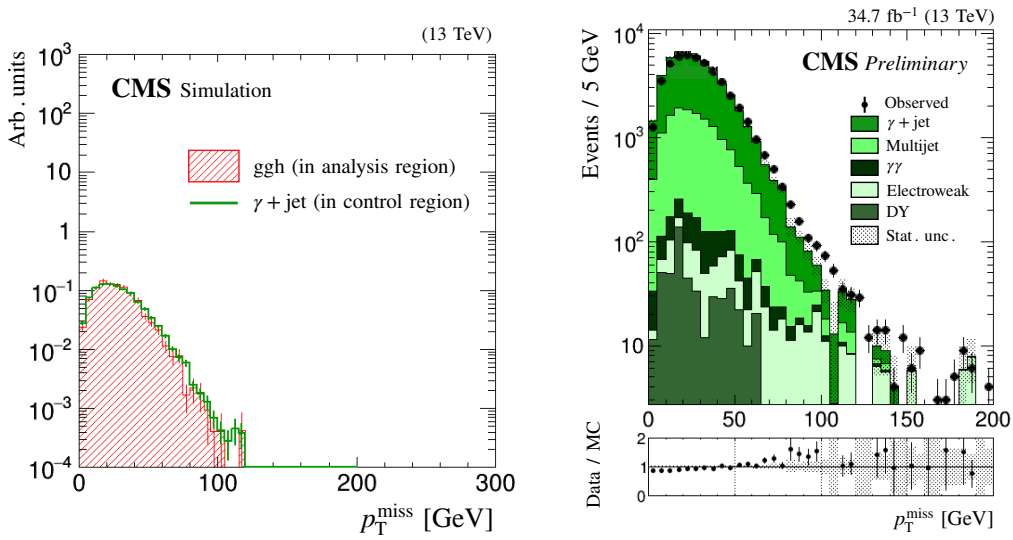

Figure 5.23: A comparison of the p_T^{miss} distribution (left) of ggh simulated events (red hatched) in the standard analysis and γ + jet simulated events (green) in the control region. Also shown is the p_T^{miss} distribution of data and simulation in the γ + jet control region (right).

region, which has a similar p_T^{miss} distribution to the SM Higgs boson events as shown in Fig. 5.23 (left). The p_T^{miss} distribution of observed and simulated events in the γ + jet control region is shown in Fig. 5.23 (right). In the control region, the efficiency for data and simulated events to pass the p_T^{miss} selection is compared. The 50% efficiency difference is applied as a systematic uncertainty on the normalization of the ggh and VBF samples. While this may seem like a large uncertainty, there are so few events with high p_T^{miss} for these samples, that this has little overall effect on the analysis.

In events with low p_T^{miss}, the ϕ component of the p_T^{miss} is not well defined. A systematic uncertainty is assigned to account for any difference between data and simulation of the topological p_T^{miss} variables. These variables are compared in a Z $\rightarrow$ ee control region as shown in Fig. 5.24. The difference in efficiencies between data and simulation selection for these variables is 1% and 4%. These are taken as systematic uncertainties on the simulated events with mismeasured

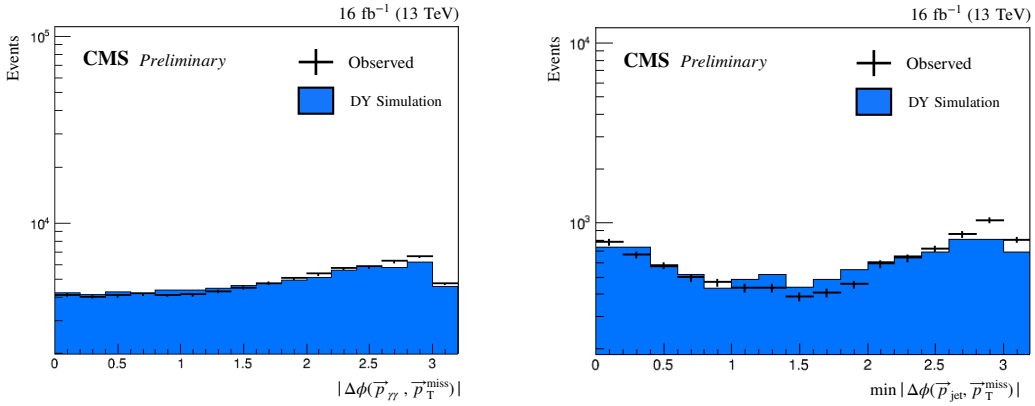

Figure 5.24: The $|\Delta\phi(\vec{p}_{\gamma\gamma}, \vec{p}_{\mathrm{T}}^{\,\mathrm{miss}})|$ (left) and $\min|\Delta\phi(\vec{p}_{\mathrm{jet}}, \vec{p}_{\mathrm{T}}^{\,\mathrm{miss}})|$ (right) for observed and simulated events in a $\mathrm{Z} \rightarrow \mathrm{ee}$ control region. Other electroweak backgrounds are included in the simulation, but DY is the only visible contributor in this region.

$p_{\mathrm{T}}^{\mathrm{miss}}$ (i.e. the ggh and VBF samples).

These systematic uncertainties, summarized in Tab. 5.6, do not include any systematic uncertainty on the nonresonant background. The nonresonant background is extracted from an analytic function fit to the data. As mentioned in Sec. 5.7.2, because the bias in the nonresonant background estimation is five times less than the statistical uncertainty in the number of fitted events, any bias is completely negligible and is therefore not included as a systematic uncertainty. It is also useful to note that the whole analysis is statistically limited. The systematic uncertainties, just described, have very little effect on the search results.

5.9 Statistical analysis

Results in particle physics are generally presented as limits on the signal strength modifier μ which scales the overall rate of a potential signal. For ex-

ample, $\mu = 0$ corresponds to the background-only hypothesis, while $\mu = 1$ corresponds to exactly the amount of signal predicted. For the signal extraction of this analysis, a simultaneous unbinned maximum-likelihood fit is performed for the low-$p_{\mathrm{T}}^{\mathrm{miss}}$ and high-$p_{\mathrm{T}}^{\mathrm{miss}}$ categories. Sec. 5.9.1 details the fit strategy, while Sec. 5.9.2 explains how this in turn is used to set upper limits on the signal production cross section. Finally, the statistical combination of multiple Higgs boson decay channels is described in Sec. 5.9.3.

5.9.1 Maximum-likelihood fit

A maximum-likelihood fit is used in this analysis to extract the signal strength modifier μ. Maximizing the likelihood function is simply a way to find the values of the model parameters, in this case μ and the nuisance parameters θ, that maximize the agreement between the predicted model and the observed data. The model is constructed with the pdfs $f_s(x)$ and $f_b(x)$ of observable x and the expected event rates S and B for the signal and background, respectively. In this analysis, the observable is the diphoton invariant mass $m_{\gamma\gamma}$. As mentioned in Sec. 5.7, the signal pdf $f_s(x)$ is taken from simulated signal events. The background pdf $f_b(x)$ is a sum of a continuous distribution extracted from data modeling the nonresonant contributions and a resonant contribution taken from simulated $\mathrm{h} \to \gamma\gamma$ events.

The exact likelihood function [87] is given by:

$$\mathcal{L}(\mathrm{data}|\mu, \theta) = \mathrm{Poisson}(\mathrm{data}|\mu s + b) \cdot \rho(\theta|\tilde{\theta}) \tag{5.3}$$

where data represents the experimental observation and θ are nuisance parameters. In an unbinned likelihood for n observed events, the probability of ob-

serving the data distribution given the signal strength and nuisance parameters is given by the Poisson pdf:

$$\text{Poisson}(\text{data}|\mu s + b) = \frac{1}{n}\prod_i (\mu S f_s(x_i) + B f_b(x_i)) \cdot e^{-(\mu S + B)}. \quad (5.4)$$

Maximizing this likelihood function gives the value of μ that offers the best agreement between this model and the data.

However, the predictions for both the signal and background yields prior to looking at the data are subject to uncertainties. The systematic uncertainties, described in Sec. 5.8 and summarized in Tab. 5.6, are represented by the set of nuisance parameters θ in the likelihood. Systematic uncertainties are handled by the additional pdfs $\rho(\theta|\tilde{\theta})$ in the likelihood, where $\tilde{\theta}$ is the best estimate of the nuisance. In this analysis, only the photon scale uncertainty modifies the expected shape of the signal and resonant background distributions, and is therefore included in the fit as a variation of the model. All other uncertainties affect the normalization only and are represented as log-normal pdfs in the likelihood. The full background pdf and the signal plus background pdf before the maximum-likelihood fit ("prefit") are compared with the signal plus background pdf after the maximum-likelihood fit ("postfit") in Fig. 5.25.

5.9.2 Exclusion limit calculation

The expected and observed yields are used to calculate an upper limit on the production cross section of $\mathrm{h} + \mathrm{DM}$ production via the two benchmark signal models. Upper limits are computed [87] at 95% confidence level (CL) using a profile likelihood ratio and the modified frequentist criterion [88, 89].

The compatibility of the data with the background-only and signal plus

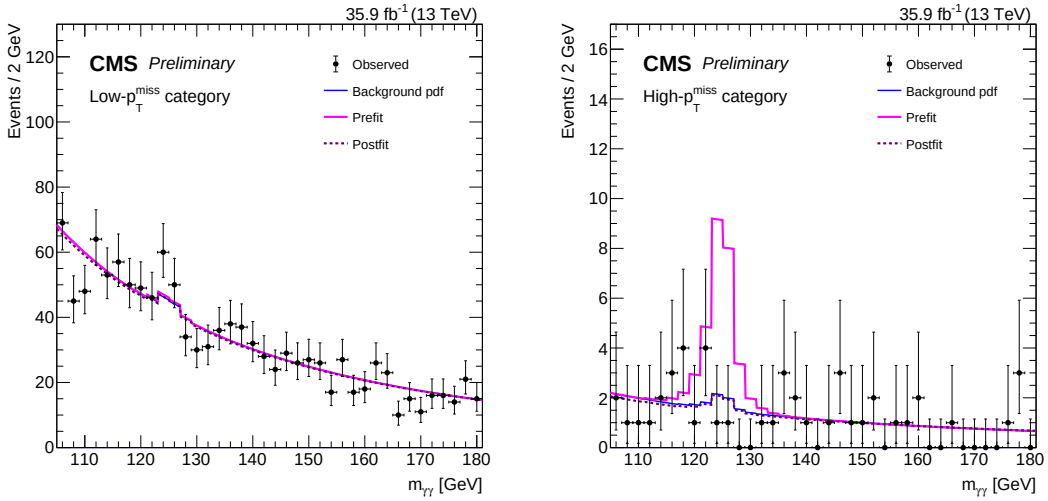

Figure 5.25: Signal plus background pdf prefit (pink) and postfit (purple dashed) for the low-$p_{\mathrm{T}}^{\mathrm{miss}}$ (left) and high-$p_{\mathrm{T}}^{\mathrm{miss}}$ (right) categories. The signal plus background pdf postfit is comparable to the total background pdf prefit (blue). The signal pdf is shown for the Z′-2HDM signal with $m_{Z'} = 600$ GeV and $m_{\mathrm{A}} = 300$ GeV.

background hypotheses is evaluated with the profile likelihood ratio $\tilde{q}_\mu$ test statistic [90]:

$$\tilde{q}_\mu = -2 \ln \frac{\mathcal{L}(\mathrm{data}|\mu, \hat{\theta}_\mu)}{\mathcal{L}(\mathrm{data}|\hat{\mu}, \hat{\theta})}. \tag{5.5}$$

The $\hat{\mu}$ and $\hat{\theta}$ are the global estimators (values that maximize the likelihood), while $\hat{\theta}_\mu$ is the conditional estimator of θ for a given a value of μ and the data. Higher values of $\tilde{q}_\mu$ correspond to a larger compatibility between the data and the μ. The value of $\hat{\mu}$ is constrained to $0 \leq \hat{\mu} \leq \mu$. Values of $\hat{\mu} < 0$ would result in unphysical negative signal rates and the $\hat{\mu} \leq \mu$ constraint yields a one-sided confidence limit so that upward data fluctuations will not exclude signals with strength μ.

Instead of finding just the μ that has the global maximum likelihood, several values of μ are scanned over. The observed $\tilde{q}_\mu^{\mathrm{obs}}$ is evaluated for each value of μ. Likewise, the estimators $\hat{\theta}_\mu^{\mathrm{obs}}$ are extracted from the maximum-likelihood

fit, as described in Sec. 5.9.1, for each μ tried. Using these estimators, the pdfs $f(\tilde{q}_\mu|\mu, \hat{\theta}_\mu^{\rm obs})$ are constructed [2] for both the $\mu = 0$ background-only and $\mu > 0$ signal plus background hypotheses. The p-value (probability of observing $\tilde{q}_\mu \geq \tilde{q}_\mu^{\rm obs}$) under the signal plus background hypothesis is then given by:

$$p_{s+b} = \int_{\tilde{q}_\mu^{\rm obs}}^{\infty} f(\tilde{q}_\mu|\mu, \hat{\theta}_\mu^{\rm obs}) d\tilde{q}_\mu \tag{5.6}$$

while the p-value for the background-only hypothesis is evaluated as:

$$p_b = \int_{\tilde{q}_0^{\rm obs}}^{\infty} f(\tilde{q}_\mu|0, \hat{\theta}_0^{\rm obs}) d\tilde{q}_\mu. \tag{5.7}$$

The ratio of these probabilities

$$\mathrm{CL}_s(\mu) = \frac{p_{s+b}}{p_b} \tag{5.8}$$

is a modified frequentist criterion [88,89] that is used to put confidence limits on signal production. When $\mathrm{CL}_s(\mu) \leq \alpha$, the signal strength μ is excluded at a $1-\alpha$ confidence level. To extract observed 95% CL upper limits on signal significance ($\mu_{95\%\ \mathrm{CL}}$), the value of μ is adjusted until $\mathrm{CL}_s \leq 0.05$. Since $\mu_{95\%\ \mathrm{CL}}$ is interpreted as $\sigma_{95\%\ \mathrm{CL}}/\sigma_{\rm th}$, for each point in the parameter space of a signal model, values of $\mu_{95\%\ \mathrm{CL}} \leq 1$ exclude, at 95% CL, the signal with production cross section $\sigma_{95\%\ \mathrm{CL}}$ at least $\sigma_{\rm th}$ at that point.

Expected limits are a way to characterize the sensitivity of the search to a potential signal and are constructed in a similar way as the observed limits. Background-only pseudo-experiments are used instead of the observed data to evaluate the CL_s statistic and $\mu_{95\%\ \mathrm{CL}}$. The expected exclusion values are extracted from the cumulative probability distribution of the $\mu_{95\%\ \mathrm{CL}}$. The median

[2] These pdfs are either constructed using pseudo-experiments or with an asymptotic approximation [90] where the pdf is approximated by a χ^2 distribution with one degree of freedom. The asymptotic approximation agrees with full limits made from pseudo-experiments to better than a few percent as shown in Fig. 5.26.

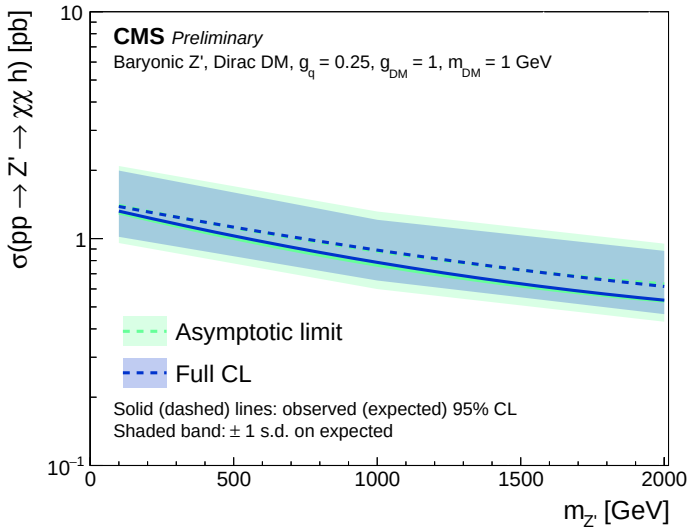

Figure 5.26: Comparison of upper limits on the baryonic Z′ signal between the full CL generated by pseudo-experiments and the asymptotic approximation.

expected limit is the value of $\mu_{95\%\ \mathrm{CL}}$ when the cumulative probability reaches 50% and corresponds to the median value with which a nonzero μ is rejected assuming the background-only hypothesis. Similarly, the plus (minus) one and two standard deviation bands are the $\mu_{95\%\ \mathrm{CL}}$ values where the cumulative distribution reaches 84% (16%) and 97.5% (2.5%), respectively.

5.9.3 Combination with other Higgs boson decay channels

The $\mathrm{h} \to \gamma\gamma$ decay channel, while unique in its ability to probe low-$p_{\mathrm{T}}^{\mathrm{miss}}$ dark matter signatures, is not the only Higgs boson decay channel that has sensitivity to these DM models. To improve the search power of the analysis, it is useful to do a statistical combination with other Higgs boson decay channels.

The h decay channels are combined using a joint likelihood function which

is simultaneously fit for all channels. The joint likelihood is given by:

$$\mathcal{L}(data|\mu, \theta_{comb}) = \prod_{channel} \mathcal{L}(data|\mu, \theta_{channel}). \tag{5.9}$$

Here the μ is the same across all h decay channels, while the rates expected for each channel assumes the Higgs boson branching fraction predicted by the SM [5]. Exclusion limits are produced as described in Sec. 5.9.2 using this likelihood function in the profile likelihood ratio.

Theoretical uncertainties and the uncertainty on the integrated luminosity are assumed to be 100% correlated between the channels. Other uncertainties mentioned in Sec. 5.8 are unique to the $\mathrm{h} \to \gamma\gamma$ channel. The results presented here will primarily focus on the statistical combination with the $\mathrm{h} \to \tau\tau$ decay channel for the 2016 data set [29]. A combination between the $\mathrm{h} \to \gamma\gamma$ and $\mathrm{h} \to \mathrm{b\bar{b}}$ decay channels is completed for the 2015 data set [28]. Additionally, a combination of the the 2016 analysis results for the five Higgs boson decay channels: $\gamma\gamma$, $\tau\tau$, $\mathrm{b\bar{b}}$, ZZ, and WW is presented in Ref. [32].

5.10 Results

Although not used directly in making exclusion limits, it is useful to look at the number of events with $m_{\gamma\gamma}$ near the Higgs boson mass. The expected number of background events is estimated from the signal plus background fit shown in Fig. 5.25. These are compared with the number of observed events in the $m_{\gamma\gamma}$ range of 122–128 GeV in Table 5.7. An example event display of one of the six observed events in the high-$p_{\mathrm{T}}^{\mathrm{miss}}$ category is shown in Fig. 5.27.

As evident in Table 5.7, in the low-$p_{\mathrm{T}}^{\mathrm{miss}}$ category, there is a slight excess in

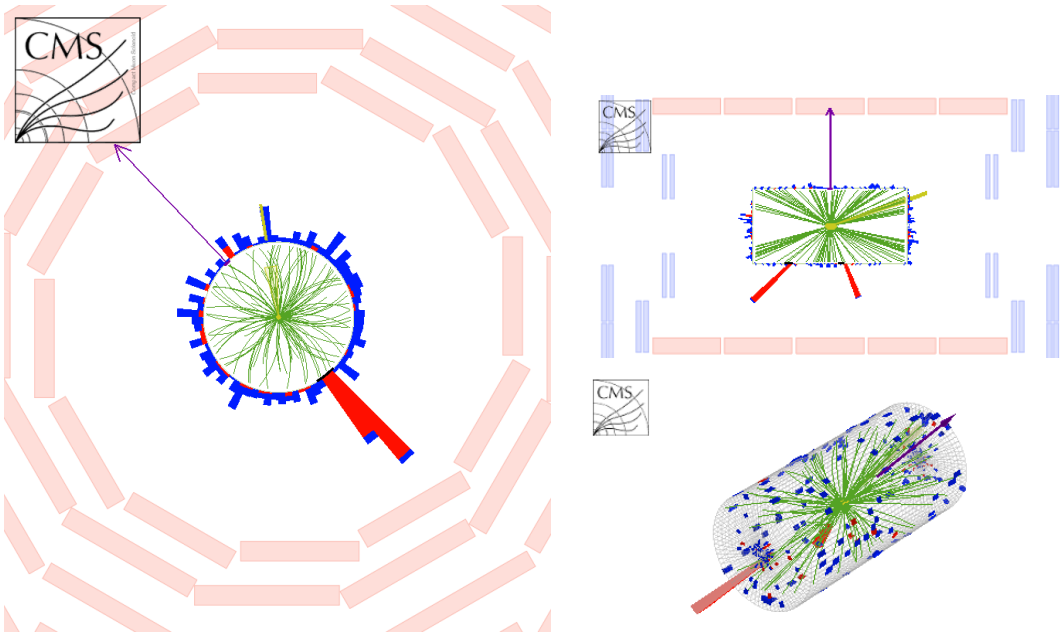

Figure 5.27: Event display for one event observed in the high-$p_{\mathrm{T}}^{\mathrm{miss}}$ signal region. ECAL (HCAL) energy deposits are shown in red (blue) and the $\vec{p}_{\mathrm{T}}^{\mathrm{miss}}$ is shown in purple.

Table 5.7: Expected background yields and observed numbers of events in the $m_{\gamma\gamma}$ range of 122–128 GeV are shown for the low- and high-$p_{\mathrm{T}}^{\mathrm{miss}}$ categories. The nonresonant background is estimated from the analytic function fit to data. The SM Higgs boson background is presented separately for the irreducible Vh production and for the other production modes. The statistical and systematic uncertainties are listed.

Expected background	Low-$p_{\mathrm{T}}^{\mathrm{miss}}$ category	High-$p_{\mathrm{T}}^{\mathrm{miss}}$ category
SM $\mathrm{h} \to \gamma\gamma$ (Vh)	2.9 ± 0.1 (stat) ± 0.2 (syst)	1.26 ± 0.05 (stat) ± 0.09 (syst)
SM $\mathrm{h} \to \gamma\gamma$ (ggh, $\mathrm{t\bar{t}h}$, VBF)	5.3 ± 0.3 (stat) ± 1.2 (syst)	0.11 ± 0.01 (stat) ± 0.01 (syst)
Nonresonant background	125 ± 11 (stat)	4.5 ± 2.1 (stat)
Total background	133 ± 11 (stat) ± 1 (syst)	5.9 ± 2.1 (stat) ± 0.1 (syst)
Observed events	159	6

the number of events observed around $m_{\gamma\gamma} = 125$ GeV. If the low-$p_{\mathrm{T}}^{\mathrm{miss}}$ category is taken alone, this excess has a local significance of 2.0 assuming that the SM Higgs boson significance is 1. The excess has negligible impact on the upper limits on the two benchmark signal models, because the limits are completely driven by the high-$p_{\mathrm{T}}^{\mathrm{miss}}$ category.

Expected signal yields as well as signal efficiencies in both the low- and high-$p_{\mathrm{T}}^{\mathrm{miss}}$ categories for select points of the benchmark signal models are shown in Table 5.8. The observed results are interpreted in the context of the Z′-2HDM and baryonic Z′ signal models in Sec. 5.10.1 and Sec. 5.10.2. A comparison with direct detection experiments is presented in Sec. 5.10.3.

Table 5.8: The expected signal yields and the product of acceptance and efficiency ($\mathrm{A}\epsilon$) for the two benchmark models. The Z′-2HDM signal is shown for the parameters $m_{\mathrm{A}} = 300$ GeV and $m_{\mathrm{Z}'} = 1000$ GeV. The baryonic Z′ signal assumes the parameters $m_{\mathrm{DM}} = 1$ GeV and $m_{\mathrm{Z}'} = 100$ GeV.

Signal	Low-$p_{\mathrm{T}}^{\mathrm{miss}}$	High-$p_{\mathrm{T}}^{\mathrm{miss}}$
Z′-2HDM		
Expected yield	0.1 ± 0.4	4.5 ± 0.6
$\mathrm{A}\epsilon$ [%]	0.1	42.6
Baryonic Z′		
Expected yield	14.7 ± 6.7	13.8 ± 6.4
$\mathrm{A}\epsilon$ [%]	6.4	6.0

5.10.1 Z′-2HDM interpretation

The results presented above are interpreted in the context of the Z′-2HDM benchmark, which is described earlier in Sec. 2.5.1. Fully-simulated samples are only available for select mass points of the signal model. An interpolation procedure is performed to extract smooth continuous limits.

The $m_{\gamma\gamma}$ distribution is not dependent on $m_{\mathrm{Z}'}$ or m_{A} and therefore the shape remains the same for all mass points of the Z′-2HDM signal. However, the number of events expected, which depends on the cross section and efficiency for the signal to pass all selection, can vary for each signal point. Specifically, because the signal mass points have different $p_{\mathrm{T}}^{\mathrm{miss}}$ distributions, they have different selection efficiencies. The efficiencies for the fully-simulated mass points are

shown in Fig. 5.28 in each of the $p_{\mathrm{T}}^{\mathrm{miss}}$ categories. For each signal, the number of events expected is given by $N_{events} = \sigma_{\mathrm{th}} \mathcal{L} \mathrm{A} \epsilon$.

In order to interpolate between the fully-simulated points, the two-dimensional efficiencies of Fig. 5.28 were fit with a first order polynomial function of the form: $p_0 + p_1 m_{\mathrm{Z}'} + p_2 m_{\mathrm{A}} + p_3 m_{\mathrm{Z}'} m_{\mathrm{A}}$ where $p_{0,1,2,3}$ are free parameters. The signal normalization that is actually used in the fit is given by the parameterized number of events expected for each signal point. Upper exclusion limits are extracted using the method detailed in Sec. 5.9.2. A comparison of the limits from the fully-simulated samples and the interpolated method are shown in Fig. 5.29. Agreement within one standard deviation between the methods is observed.

For the Z′-2HDM with $m_{\mathrm{A}} = 300\ \mathrm{GeV}$, the upper limits on the production cross section as a function of $m_{\mathrm{Z}'}$ are shown in Fig. 5.30. The two-dimensional upper limits on the signal significance ($\sigma_{95\%\ \mathrm{CL}}/\sigma_{\mathrm{th}}$) are shown in Fig. 5.31 (left). For the $m_{\mathrm{A}} = 300\ \mathrm{GeV}$ signals, the $\mathrm{h} \to \gamma\gamma$ channel excludes Z′ masses from 550 GeV to 860 GeV at 95% CL .

The statistical combination of the $\mathrm{h} \to \gamma\gamma$ decay channel with four other Higgs boson decay channels [32]: $\mathrm{h} \to \mathrm{b\bar{b}}$, $\mathrm{h} \to \tau\tau$, $\mathrm{h} \to \mathrm{WW}$, and $\mathrm{h} \to \mathrm{ZZ}$ improves the overall sensitivity of Mono-h searches. With this combination, Mono-h searches exclude much larger regions of phase space as shown in Fig. 5.31 (right). For the $m_{\mathrm{A}} = 300\ \mathrm{GeV}$ signals, the combined Mono-h analysis excludes Z′ masses from 550 GeV to 3100 GeV. Above 800 GeV, the sensitivity is entirely due to the $\mathrm{h} \to \mathrm{b\bar{b}}$ channel [30]. However, below this, the results are completely driven by the $\mathrm{h} \to \gamma\gamma$ channel. This is more evident in Fig. 5.32.

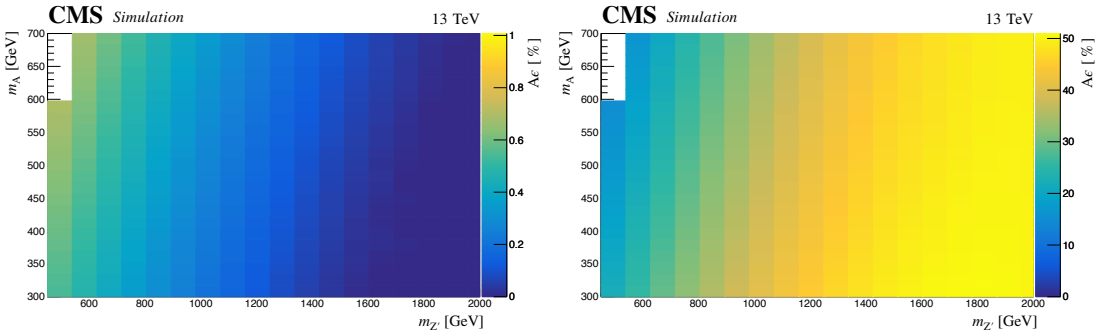

Figure 5.28: The $\mathrm{A}\epsilon$ for the Z′-2HDM fully-simulated samples in the low-$p_{\mathrm{T}}^{\mathrm{miss}}$ (left) and high-$p_{\mathrm{T}}^{\mathrm{miss}}$ (right) regions as a function of $m_{Z'}$ and m_{A}.

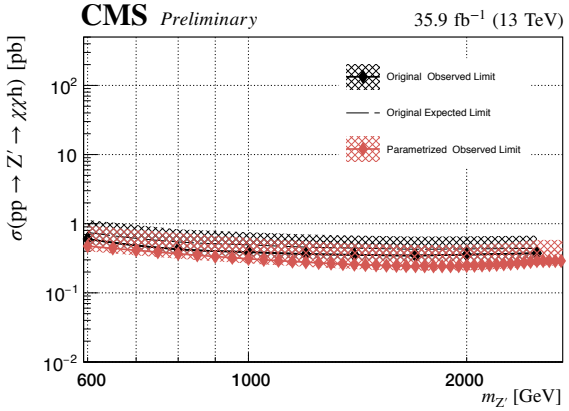

Figure 5.29: Comparison of the observed exclusion limits for the fully-simulated limits (black) and the interpolated limits (red) for the Z′-2HDM signal with $m_{\mathrm{A}} = 300$ GeV.

Finally, the combined Mono-h results are also interpreted in the two-dimensional plane of $m_{Z'}$ and $\tan\beta$. The ratio of vacuum expectation values $\tan\beta$ does not affect the kinematic distributions, therefore the results are reinterpreted to provide exclusion curves on this parameter as well. The 95% CL exclusion is shown in Fig. 5.33.

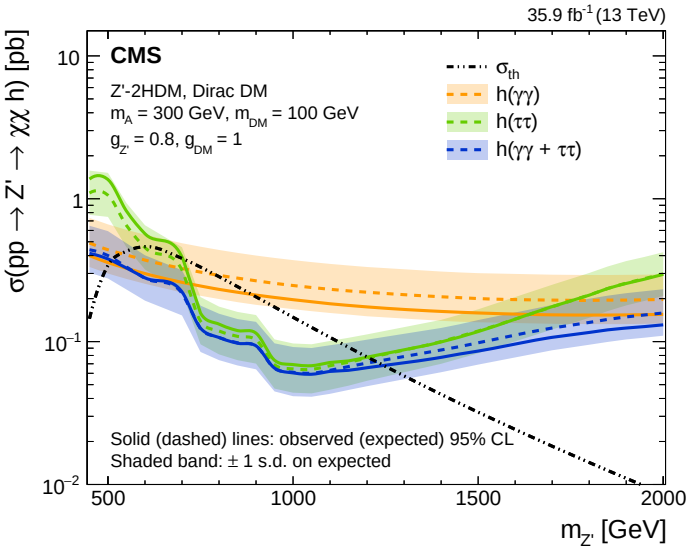

Figure 5.30: Expected and observed 95% CL upper limits on the Z′-2HDM cross section for dark matter associated production with a Higgs boson ($Z' \to \chi\chi h$) are shown. Limits are given for the $h \to \gamma\gamma$ channel (orange), $h \to \tau\tau$ channel (green), and their combined exclusion (blue).

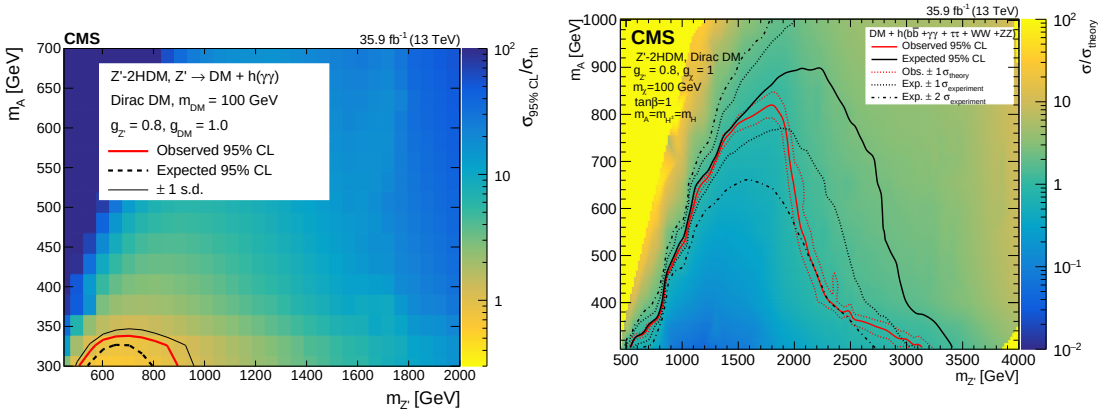

Figure 5.31: Observed 95% CL upper limits on the Z′-2HDM signal strength for the $h \to \gamma\gamma$ (left) and the combined Mono-h channels (right). The observed (expected) two-dimensional exclusion curves are shown with thick red (dashed black) lines. The plus and minus one standard deviation expected exclusion curves are also shown as thin black lines. The region below the lines is excluded.

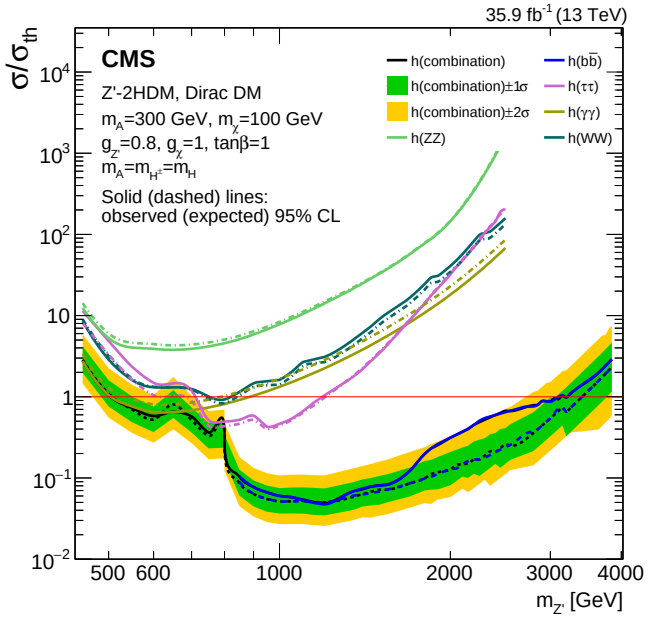

Figure 5.32: Observed and expected 95% CL upper limits on the Z′-2HDM signal strength as a function of $m_{Z'}$ for each analyzed Mono-h channel separately (the $\mathrm{h} \to \gamma\gamma$ channel is shown in olive green) and for their combined exclusion (black) [32].

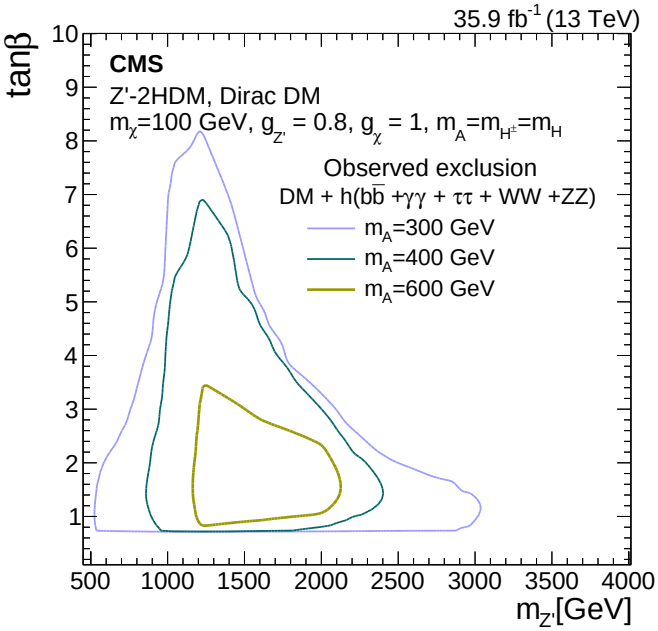

Figure 5.33: Observed 95% CL exclusion of the Z′-2HDM signal strength for the combined Mono-h results in the two-dimensional plane of $\tan\beta$ and $m_{Z'}$.

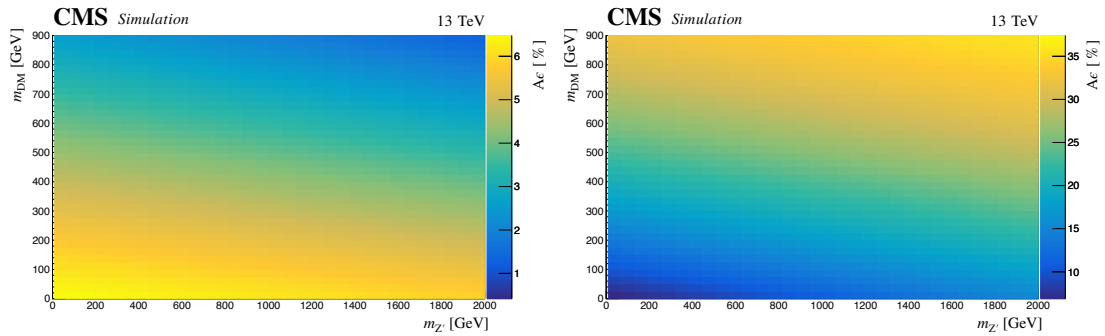

Figure 5.34: The $A\epsilon$ for the baryonic Z′ model in the low-p_T^{miss} (left) and high-p_T^{miss} (right) regions as a function of $m_{Z'}$ and m_{DM}.

5.10.2 Baryonic Z′ interpretation

The results of the search are also interpreted in the context of the baryonic Z′ model, described earlier in Sec. 2.5.2. Fully-simulated samples are only available for select mass points in the parameter space of the model, so smooth exclusion limits are achieved by interpolating between the masses. This is exactly the same procedure that is done for the interpolation in the Z′-2HDM interpretation. The efficiency is parameterized and used to scale the expected signal yield for each mass point. Resulting efficiency for the baryonic Z′ signal in the low- and high-p_T^{miss} categories is shown in Fig. 5.34.

Exclusion limits are then extracted for each signal mass point. For the baryonic Z′ model with $m_{DM} = 1$ GeV, upper limits on the production cross section as a function of $m_{Z'}$ are shown in Fig. 5.35. The two-dimensional upper limits on the signal significance are shown in Fig. 5.36 (left). For $m_{DM} = 1$ GeV, The $h \to \gamma\gamma$ channel alone excludes Z′ masses up to 574 GeV. The results for the statistical combination of $h \to \gamma\gamma$, $h \to \tau\tau$, $h \to b\bar{b}$, $h \to WW$, and $h \to ZZ$ are shown in Fig. 5.36 (right). The combined exclusion is primarily driven by the $h \to b\bar{b}$ sensitivity, however, again the $h \to \gamma\gamma$ channel offers added sensitivity

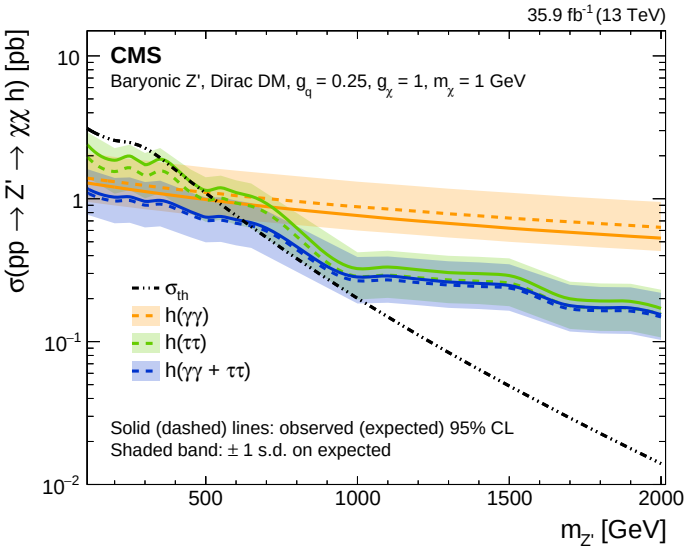

Figure 5.35: Expected and observed 95% CL upper limits on the baryonic Z′ cross section for dark matter associated production with a Higgs boson ($Z' \to \chi\chi h$) are shown. Limits are given for the $h \to \gamma\gamma$ channel (orange), $h \to \tau\tau$ channel (green), and their combined exclusion (blue).

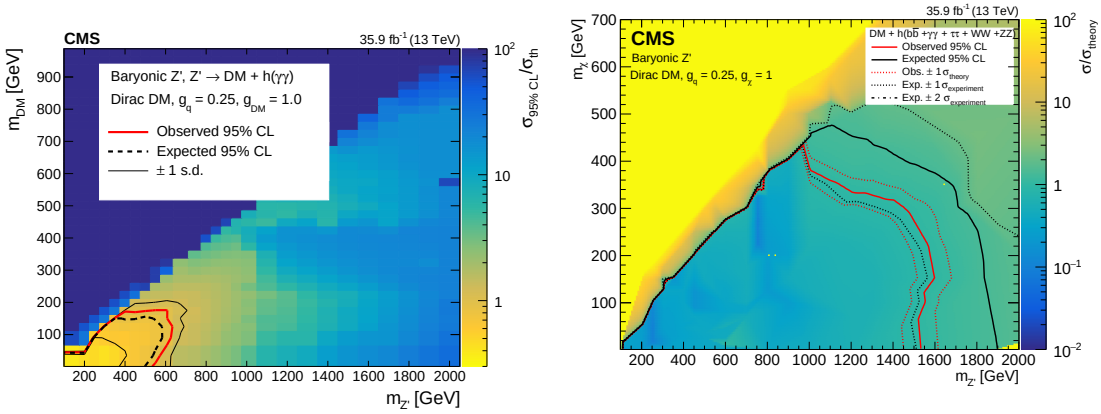

Figure 5.36: Observed 95% CL upper limits on the baryonic Z′ signal strength for the $h \to \gamma\gamma$ (left) and the combined Mono-h channels (right). The observed (expected) two-dimensional exclusion curves are shown with thick red (dashed black) lines. The plus and minus one standard deviation expected exclusion curves are also shown as thin black lines. The region below the lines is excluded.

in the low mass regions. This can be seen in Fig. 5.37. The combined Mono-h analyses, for $m_{\mathrm{DM}} = 1$ GeV exclude Z′ masses up to 1600 GeV at 95% CL.

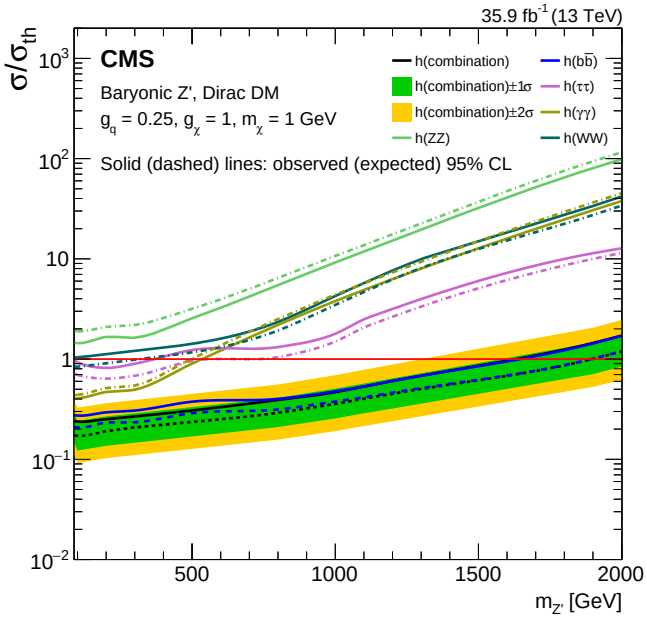

Figure 5.37: Expected and observed 95% CL upper limits on baryonic Z′ signal significance are shown for each Higgs boson decay channel ($\mathrm{h} \to \gamma\gamma$ in olive green) and their combined exclusion (black).

5.10.3 Comparison with direct detection results

In order to compare collider dark matter search results with direct detection experiments, the ATLAS-CMS Dark Matter Forum [16] proposed several s-channel simplified DM models. In this context, the upper limits on the baryonic Z′ model can be reinterpreted. In the model considered here, Dirac DM particles couple to a vector mediator, which in turn couples to the SM quarks. A single point in the parameter space of the model is determined by four variables: the DM particle mass m_{DM}, the mediator mass m_{med}, the mediator-DM coupling g_{DM}, and the universal mediator-quark coupling g_{q}. Based on the recommendations of Ref. [17], the couplings for this analysis are fixed to $g_{\mathrm{DM}} = 1.0$ and $g_{\mathrm{q}} = 0.25$.

The results for the baryonic Z′ are interpreted in the spin-independent (SI)

cross section σ^{SI} for DM scattering off of a nucleus. For a given point in the s-channel simplified model, the value of σ^{SI} is given by the equation [17]:

$$\sigma^{\mathrm{SI}} = \frac{f^2(g_{\mathrm{q}}) g_{\mathrm{DM}}^2 \mu_{\mathrm{nDM}}^2}{\pi m_{\mathrm{med}}^4}, \tag{5.10}$$

where μ_{nDM}^2 is the reduced mass of the DM-nucleon system and $f(g_{\mathrm{q}})$ is the mediator-nucleon coupling, which is dependent on g_{q}. For the vector-mediated case shown here, the mediator-nucleon coupling $f(g_{\mathrm{q}}) = 3g_{\mathrm{q}}$.

The resulting 90% CL limits on σ^{SI} are shown in Fig. 5.38. Also shown in the same plot are the exclusion limits from CDMSLite [91], LUX [92], XENON-1T [93, 94], PandaX-II [95, 96], CRESST-II [97], and CDEX-10 [98]. Beyond what is accessible in direct detection experiments, the $\mathrm{h} \to \gamma\gamma$ channel alone excludes dark matter masses between 1 and 2 GeV. The combined Mono-h limits are more stringent than those of the direct detection experiments for dark matter masses between 1 and 5 GeV.

5.11 Related ATLAS search

The ATLAS Collaboration also has a search for Mono-h in the $\mathrm{h} \to \gamma\gamma$ decay channel [27]. Although the details of the search strategy are different, the results are comparable to the analysis presented here. The analysis selects events that have two high momentum photons that pass a tight identification. Events with $m_{\gamma\gamma}$ in the range of 105 to 160 GeV are split into several categories based primarily on their $p_{\mathrm{T}\gamma\gamma}$ and $p_{\mathrm{T}}^{\mathrm{miss}}$ significance ($p_{\mathrm{T}}^{\mathrm{miss}}/\sqrt{\sum p_{\mathrm{T}}}$). Much like the analysis presented here, a maximum-likelihood fit to the $m_{\gamma\gamma}$ distribution in each category is employed to extract the signal and background estimates. The CMS

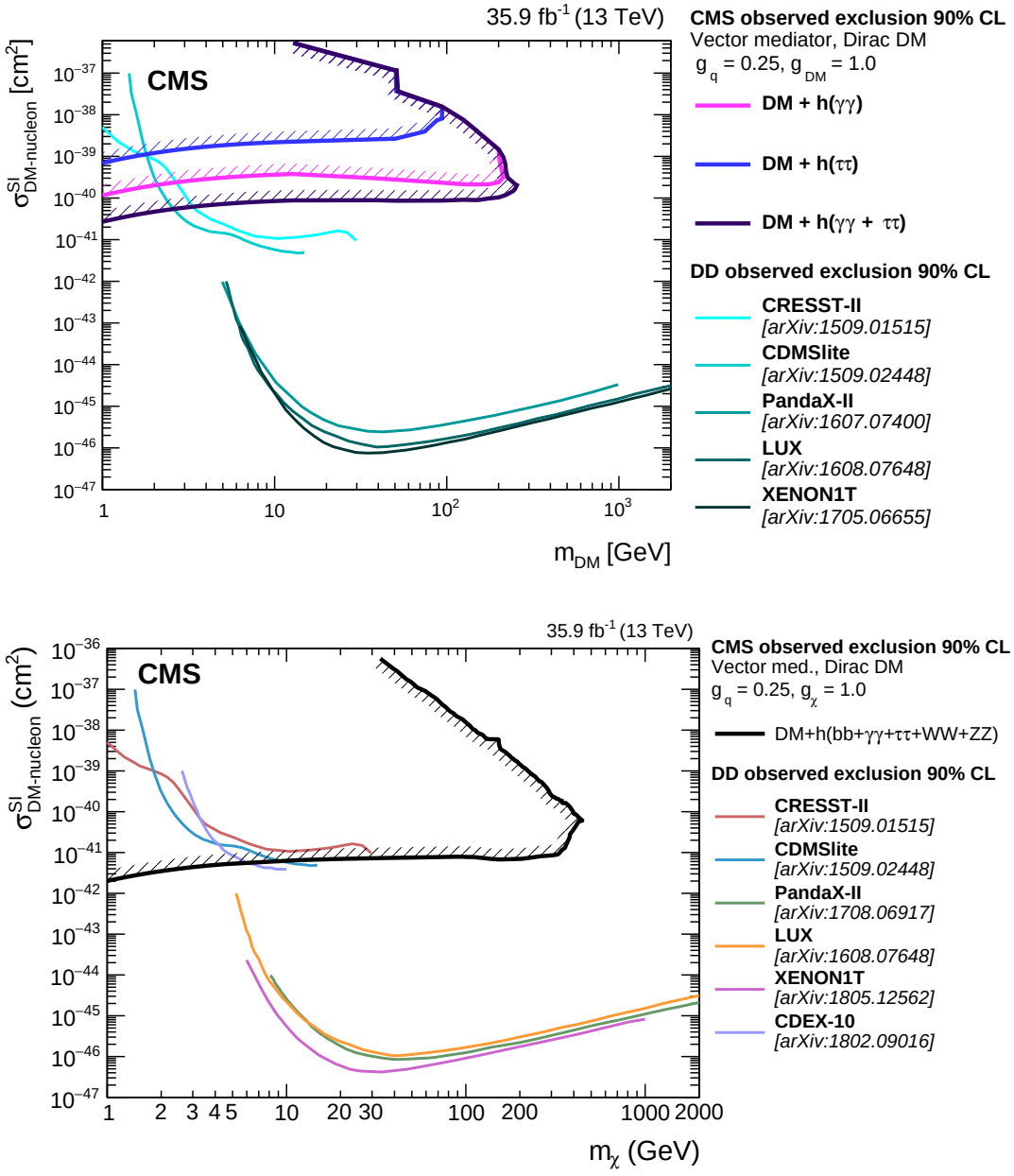

Figure 5.38: The 90% CL exclusion limits on the DM-nucleon SI scattering cross section as a function of m_{DM}. Results obtained in this analysis are compared with those from a selection of direct detection (DD) experiments. The latter exclude the regions above the curves. The exclusion limits for the $\mathrm{h} \to \gamma\gamma$ analysis (pink) are shown in the upper plot while the combined Mono-h results (black) are shown in the lower plot.

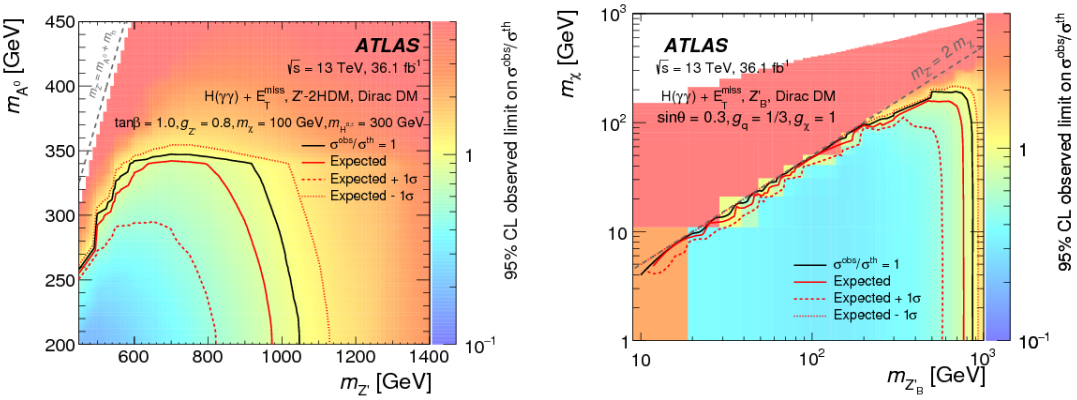

Figure 5.39: ATLAS expected and observed 95% CL exclusion limits on the predicted signal cross section for the Z′-2HDM (left) and baryonic Z′ (right) interpretations [27].

and ATLAS Mono-h searches in the $\mathrm{h} \to \gamma\gamma$ channel produce similar exclusions limits on DM production. In the Z′-2HDM interpretation, for a Z′ mass of 1000 GeV and a DM mass of 100 GeV, pseudoscalar A masses are excluded below 280 GeV. Additionally, for a DM mass of 1 GeV, baryonic Z′ masses are excluded up to 850 GeV. The ATLAS two-dimensional 95% CL exclusion limits for the Z′-2HDM and baryonic Z′ interpretations are shown in Fig. 5.39.

5.12 Summary

A search for dark matter particles produced in association with a Higgs boson is performed. The analysis focuses on the case where the Higgs boson decays to two photons, although statistical combinations with other decay channels is also done. The analysis is based on 35.9 fb^{-1} of $\sqrt{\mathrm{s}} = 13$ TeV pp collision data collected with the CMS detector during 2016. An alternative search strategy (presented in Appendix A) is performed on 2.2 fb^{-1} of data collected in 2015.

The analysis is performed by selecting pp collision events with two pho-

tons using a customized photon identification. After passing kinematic requirements, the remaining events are split into a low- and high-$p_{\mathrm{T}}^{\mathrm{miss}}$ category. The observed diphoton invariant mass is then fit with a signal plus background template. The signal strength extracted from the fit is used to set 95% CL exclusion limits on dark matter production for the two benchmark signal models.

For the Z′-two-Higgs-doublet model, with an intermediate pseudoscalar of mass $m_{\mathrm{A}} = 300\ \mathrm{GeV}$ and with dark matter mass $m_{\mathrm{DM}} = 100\ \mathrm{GeV}$, signals for Z′ masses from 550 GeV to 860 GeV are excluded with the $\mathrm{h} \to \gamma\gamma$ channel alone. Additionally, for the baryonic Z′ channel, with $m_{\mathrm{DM}} = 1\ \mathrm{GeV}$, the $\mathrm{h} \to \gamma\gamma$ channel excludes Z′ masses up to 574 GeV. Statistically combining the $\mathrm{h} \to \gamma\gamma$ results with searches performed with other Higgs boson decay channels is a powerful tool to enhance the search power of the results from any channel alone. This is exploited in the results presented here. The interpretation of the results include an extrapolation to limits on spin-independent cross section for dark matter-nucleon interaction, which facilitates comparison, albeit model-dependent, between the collider DM searches and direct detection experimental results.

CHAPTER 6

FUTURE CMS UPGRADES

The upgrade of the LHC to the High-Luminosity LHC (HL-LHC) is planned for 2025. It is designed to increase the peak luminosity to about $7.5 \times 10^{34}\,\mathrm{cm^{-2}\,s^{-1}}$ and aims to achieve an integrated luminosity of $3000\ \mathrm{fb}^{-1}$ [99]. This HL-LHC era will yield an average pileup between 140 and 200, as compared with the average of 27 pileup delivered by the current LHC (as shown earlier in Fig. 5.3). In order to maintain its sensitivity to physics searches, such as the Mono-h search just presented, in these denser collisions, the CMS detector will need to undergo several upgrades.

6.1 Upgrade plans for CMS

To handle this novel and challenging environment, and to deal with significant radiation damage from years of operation, the CMS detector will undergo several upgrades to its subdetectors, as detailed in Ref. [100]. In the so-called "Phase-II" upgrade, the endcaps of the calorimeters will be replaced with higher granularity detectors. In the forward region of the detector, additional muon chambers will be added to ensure needed redundancy in coverage. Additionally, the tracker detector will need to be completely replaced. Both the pixel and silicon strip detector are being redesigned based on knowledge of the current system to improve granularity by a factor of four [101]. A new minimum-ionizing particle timing detector layer, which would be located directly outside the tracker system, is also proposed [102] to improve vertexing in this challenging environment. Additionally, to mitigate the overwhelming number of particles produced during such high pileup scenarios, charged particle tracking

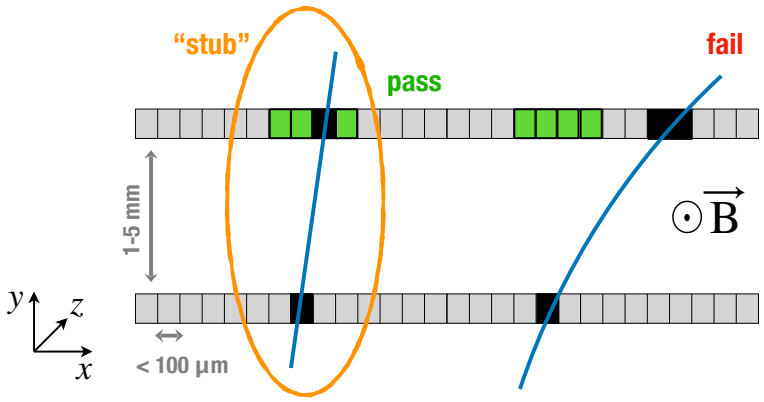

Figure 6.1: Correlated hits (stubs) in closely-spaced sensors enables rejection of low-p_{T} signals. The green shows the acceptance window where p_{T} is greater than 2 GeV.

will be added to the Level-1 (L1) trigger system. The following sections in this chapter will focus on a proposed L1 tracking implementation.

Although the inner (pixel) tracker will also be replaced, it is the outer tracker that will be read out for the L1 trigger. The added precision from the pixel detector is not needed and the pixel modules cannot be read out fast enough for L1. In contrast, the outer tracker will be designed with a unique feature to reduce the amount of data to be read out. The outer tracker will be composed of "p_{T} modules" that provide p_{T} discrimination at the level of the front-end electronics. By correlating signals in closely-spaced sensors, a coarse p_{T} measurement is available. Correlated hits ("stubs") with $p_{\mathrm{T}} > 2$ GeV are read out and sent to the L1 trigger. Figure 6.1 shows a sketch of the concept of these modules. Since most minimum-bias events have low p_{T} tracks, the use of stubs provides a data reduction by about a factor of 10 at the tracker front-end.

The upgraded tracker will be made of a cylindrical barrel portion and two endcap disks, with a layout as shown in Fig. 6.2. The outer tracker will consist

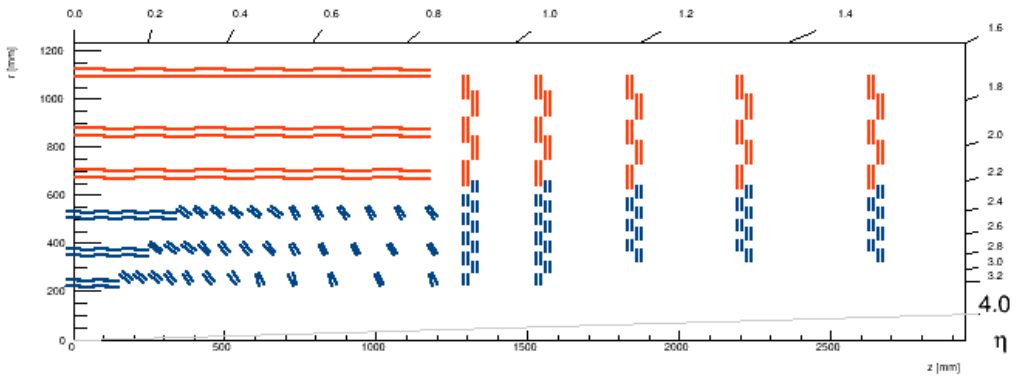

Figure 6.2: One quarter of the proposed tilted-barrel geometry for the Phase II outer tracker. The tracker consists of pixel layers (not shown) and an outer tracker of PS (blue) and 2S (red) modules.

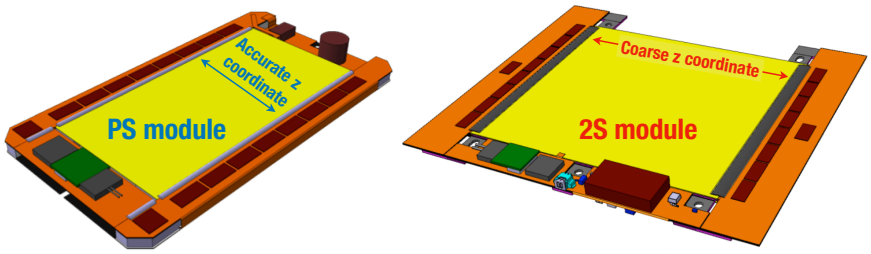

Figure 6.3: Sketches of the PS (left) and 2S (right) modules for the Phase II tracker.

of about 14,000 modules of two types of sensors: pixel-strip (PS) modules and strip-strip (2S) modules. The PS (2S) modules make up the inner (outer) regions of the detector as shown in blue (red) in Fig. 6.2. Sketches of the PS and 2S sensors are shown in Fig. 6.3. The PS sensors are made of a layer of pixels (with dimensions $1.55\,\text{mm} \times 100\mu\text{m}$) and a layer of silicon strips (of dimension $2.5\,\text{cm} \times 100\mu\text{m}$), thus providing accurate z coordinate measurements. The 2S sensors have two layers of silicon strips that are $5\,\text{cm} \times 90\mu\text{m}$, which yields a coarser z positioning.

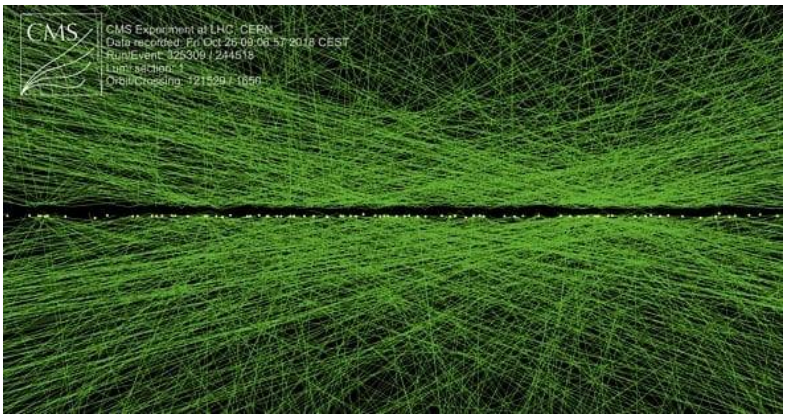

Figure 6.4: A 136 pileup event in CMS from a special run in 2017.

6.2 L1 tracking introduction

The HL-LHC will provide an extremely dense track environment, as shown in Fig. 6.4. At a pileup of 140, it is expected that there will be about 10,000 stubs with $p_{\mathrm{T}} > 2\ \mathrm{GeV}$ in the outer tracker. To maintain an optimal physics program at the HL-LHC, the aim is to keep trigger object thresholds as low as possible, ideally close to those achieved in the current CMS program. Using solely calorimeter and muon chamber information (as done in the current L1 trigger), p_{T} thresholds alone no longer provide sufficient discrimination between interesting and uninteresting physics events. Expected data rates at various thresholds for muon object triggers with and without charged particle tracking are shown in Fig. 6.5. It is clear that merely increasing the thresholds stops having discriminating power for the L1 trigger. Achieving low thresholds while keeping a manageable trigger rate necessitates including charged particle tracking at L1 (a "track-trigger").

Including particle tracks from the silicon tracker improves lepton identification and momentum measurements. Additionally, L1 tracking will provide track isolation and vertex identification for hadronic triggers. In the HL-LHC,

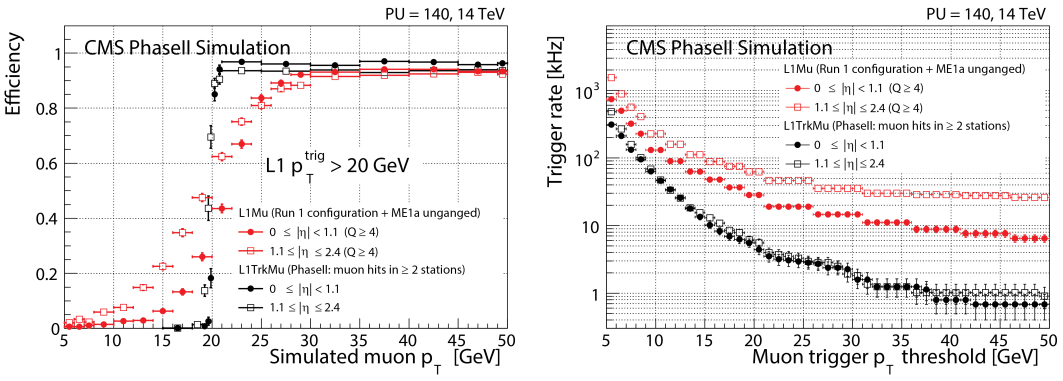

Figure 6.5: Metrics for evaluating muon trigger performance for standard muons (red) compared with muons including tracking (black). In the left plot, efficiency for muons to pass a 20 GeV threshold as a function of the muon p_{T} is shown. Trigger rate as a function of the trigger threshold is shown in the right plot.

vertices will have an average spacing of 1 mm at a pileup of 200. Therefore the z_0 resolution of the L1 tracking should be on this order to provide discrimination between vertices. Additional information about improvements to various triggers by including track information is shown in Refs. [100, 103].

Another demand on the L1 tracking system is the time budget [103]. The overall L1 latency is determined by the available buffer. For Phase II, the CMS detector, based on the size of the hardware buffers, will have 12 μs to make the L1 trigger decisions. Of this, 5 μs is allotted for the track-trigger, since the tracks will need to be correlated with other physics objects in time to make the trigger decision. Budgeting about 1 μs for the stubs to be read into the track-trigger system from the tracker front-end, this leaves 4 μs for the track finding algorithm.

Currently the fastest CMS track finding occurs on CPUs in the HLT, where the HLT decision is made in ≈ 175 ms [55]. Finding tracks in 4 μs is a completely new challenge. Recently, three approaches have been developed for finding

tracks in hardware for the Phase II detector. The rest of this chapter will focus on the tracklet approach [104–107] which is a road-search algorithm that runs on commercially available field-programmable gate array (FPGA) technology. A second approach, the TMTT approach [108], which also runs on an FPGA, uses a Hough transform and then a Kalman fit to find tracks. Finally, the third approach, the Associative Memory approach [109], is designed to hold thousands of track patterns for quick matching on a custom ASIC chip. Based on a review of demonstrators of the three approaches, a solely FPGA approach [110] is favored for the final system.

6.3 Tracklet approach

The tracklet approach uses a road-search algorithm to make charged particle tracks. An overview of the algorithm for this is given in Sec. 6.3.1. Emulation performance results are shown in Sec. 6.3.2. To meet the latency and throughput demands, the firmware implementation is finely partitioned. Section 6.3.3 details how this algorithm works in the hardware. Section 6.3.4 shows the setup and results of a demonstrator system and Sec. 6.3.5 details the latency of the approach. Finally, Sec. 6.3.6 gives some estimates on the needs of the final system and the ongoing prototyping of the hardware.

6.3.1 Algorithm

The tracklet algorithm, which is detailed below, is also depicted in Fig. 6.6.

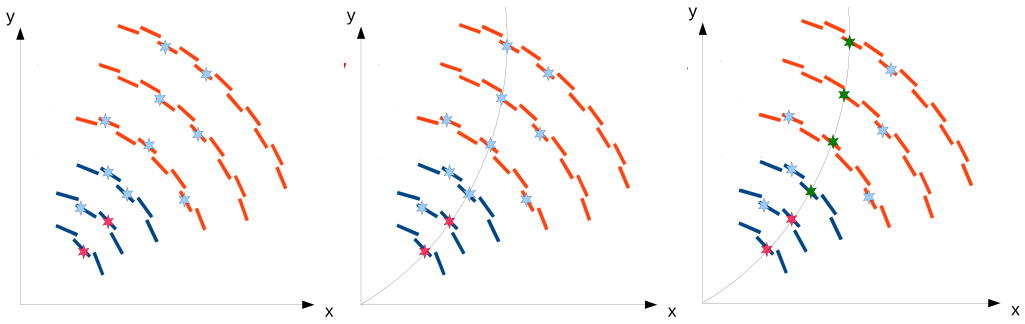

Figure 6.6: Sketch of the road-search algorithm: (left) pairs of stubs (red) in adjacent layers are combined to form a tracklet, (center) trajectory of the tracklet is projected to other layers, (right) stubs close to the projection (green) are selected as matches and the final track parameters are calculated using all associated stubs.

Seeding

The approach begins by forming track seeds (tracklets) from pairs of stubs in adjacent barrel layers or endcap disks. A tracklet is the algorithm's initial estimate of track parameters. A track in the x-y plane, sketched in Fig. 6.7, is a segment of a circle made by the two stubs in adjacent layers and the interaction point. A track, as mentioned before, is defined by the parameters: p_{T}, η, z_0, and the azimuth angle at the closest approach ϕ_0. Because of the assumption that the track originates from the interaction point, the impact parameter d_0 is not included here, but it can be included in the final fit [1].

For use in this algorithm, the track parameters of interest are ρ, t, z_0, and ϕ_0. The radius of curvature ρ is a proxy for the particle's momentum. Using the equations of the motion for a charged particle curving in a magnetic field B, the track parameter p_{T} is given by $p_{\mathrm{T}} = 0.3B\rho$. The parameter t is related to η by the relation $t = \frac{1}{2}(e^{\eta} - e^{-\eta}) = \sinh\eta$.

[1] A proposed extension to the tracklet algorithm allows for triplet seeds that do not rely on the interaction point. This allows for a non-zero d_0 and can be used to find displaced tracks [111, 112].

The calculations of the track parameters arise from the geometry of a helical trajectory. The exact helix solution for two points (r_1,ϕ_1,z_1) and (r_2,ϕ_2,z_2) is taken from the geometry of Fig. 6.7. The radius of curvature ρ of the track is given by:

$$\rho^{-1} = \frac{2}{\Delta}\sin(\phi_2 - \phi_1) \tag{6.1}$$

where $\Delta = \sqrt{r_1^2 + r_2^2 - 2r_1 r_2 \cos(\phi_2 - \phi_1)}$ is the distance between the two points in r-ϕ plane. The parameter t, the tangent of the dip angle ($\frac{\pi}{2}$ minus the angle of the trajectory with respect to the z axis), is evaluated by:

$$t = \frac{z_2 - z_1}{2\rho(\phi_2 - \phi_1)}. \tag{6.2}$$

The ϕ_0 track parameter is calculated by:

$$\phi_0 = \phi_1 - \sin^{-1}\frac{r_1}{2\rho}. \tag{6.3}$$

And finally, the z_0 parameter is calculated by:

$$z_0 = z_1 - t\rho\beta = z_1 - (z_2 - z_1)\frac{\phi_0 - \phi_1}{\phi_2 - \phi_1} \tag{6.4}$$

where the turning angle $\beta = 2\sin^{-1}\frac{r}{2\rho}$. In this way, the parameters ρ (proxy for p_{T}), t (proxy for η), z_0, and ϕ_0 are all accessible solely based on the geometric relations.

Some work is needed to simplify these calculations for quick processing on an FPGA. In the above calculations, anywhere sines or arcsines occur, they are approximated by Taylor expansions. In most cases, only the first term in the expansion is non-negligible. Additionally, the inversion of t to t^{-1}, which would be a resource-expensive operation, is instead stored in a look-up table (LUT) in the firmware. In a LUT, binned t values are used as a read address for a memory filled with their corresponding t^{-1} values.

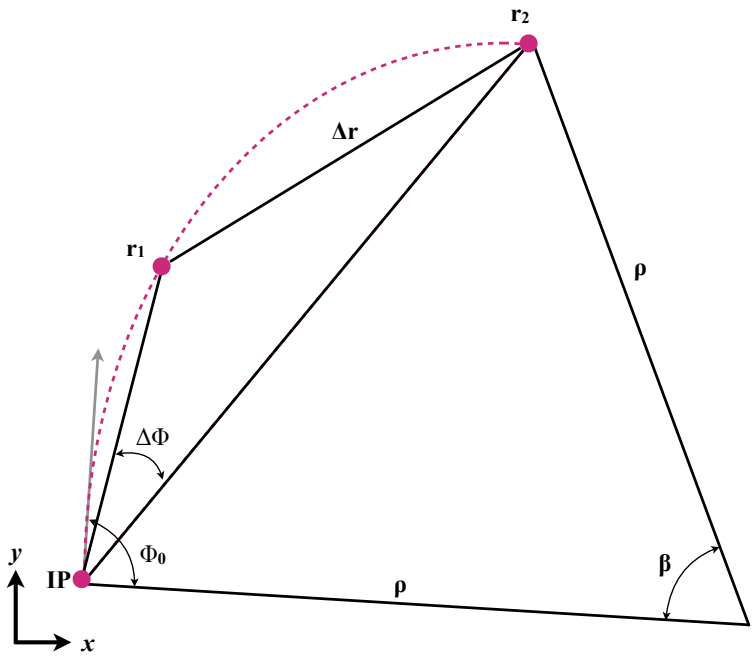

Figure 6.7: A track (pink dashed) in the x-y plane is assumed to be a segment of a circle originating from the interaction point (IP) and intersecting stubs at radii r_1 and r_2.

The above parameters uniquely define a tracklet for each pair of stubs. Candidate tracklets are rejected if they have $p_{\mathrm{T}} < 2$ GeV or do not fall within $|z_0| < 15$ cm. The tracklet already offers a good approximation of the final track parameters. This is shown in a comparison of the resolutions of the track parameters for the tracklet and final track in Fig. 6.8.

Seeding occurs for multiple combinations of layers to provide good coverage and redundancy over the entire η range of the of the detector as shown in Fig. 6.9. The algorithm is currently implemented for seeding pairs between layers 1+2, 3+4, 5+6, and between disks 1+2, and 3+4. Additionally, to recover track finding efficiency in the overlap region where a particle can pass through the barrel and disks, there are two overlap seedings: seeding from layer 1 and disk 1 and seeding from layer 2 and disk 1.

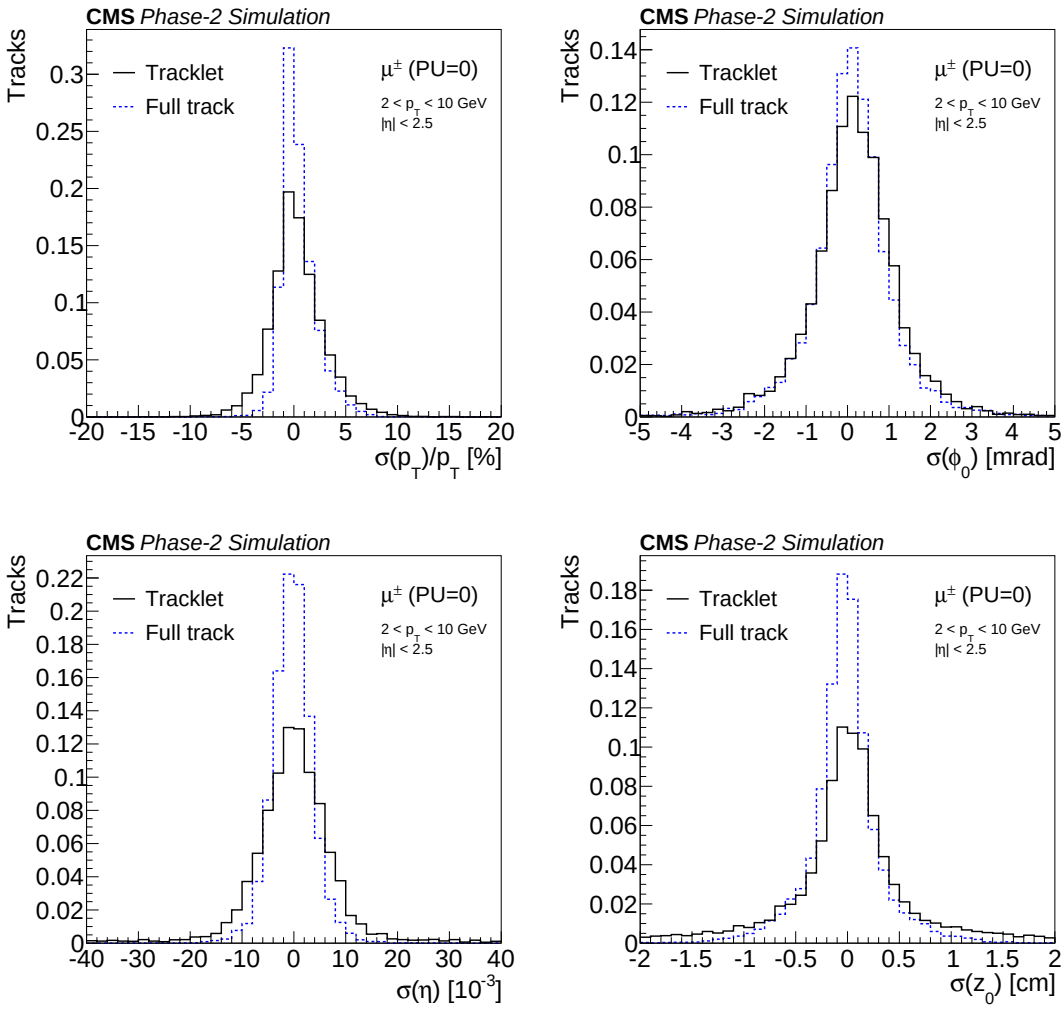

Figure 6.8: Resolution of the final track fit parameters (dashed blue) compared with tracklet parameters (solid black). Resolution comparisons are shown for p_{T} (upper left), ϕ_0 (upper right), η (lower left), and z_0 (lower right).

Match finding

Using the track parameters of the tracklet, the track is projected to other layers and disks. The track parameters are projected to an average radius (average z position) for each barrel layer (endcap disk). More precise values of the projec-

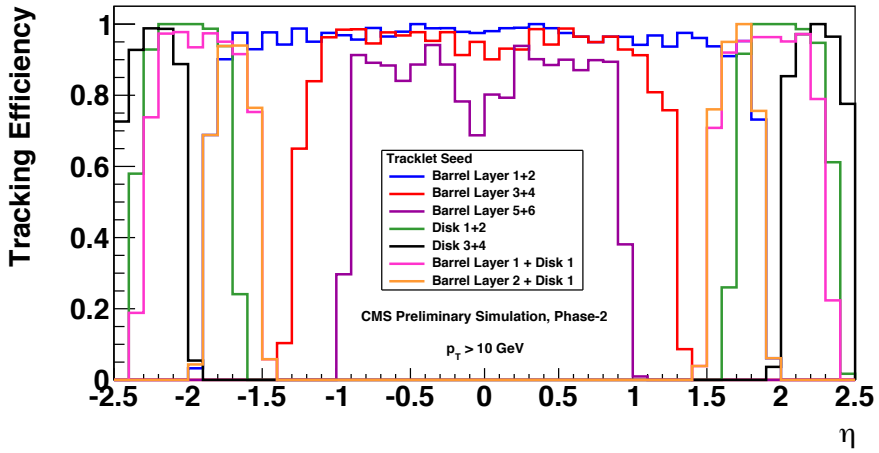

Figure 6.9: Efficiency for finding a single muon track for the seeding layer/disk combinations as a function of η [100].

tion's ϕ_{proj} and z_{proj} are then given by:

$$\begin{aligned} \phi_{proj} &= \bar{\phi}_{proj} + \Delta r \frac{\partial \phi}{\partial r} \\ z_{proj} &= \bar{z}_{proj} + \Delta r \frac{\partial z}{\partial r} \end{aligned} \tag{6.5}$$

where $\bar{\phi}_{proj}$ and $\bar{z}_{proj}$ are the projections to the nominal radius and Δr is the radial position with respect to the nominal radius. The derivatives $\frac{\partial \phi}{\partial r}$ and $\frac{\partial z}{\partial r}$, which define how much the ϕ are z position changes in the tracker layout, are evaluated for each layer/disk and used to correct the average position. For the disk region, the same calculations are done expect that z is replaced by r (and vice versa) in the equations above.

The projection of the track occurs both inwards and outwards (i.e. to and from the interaction point) simultaneously. Using predetermined search windows, the algorithm searches for stubs in these other layers that are consistent with the original track's parameters. Matched stubs, along with the difference between the projected tracklet's position and the stub position, are stored as a track candidate.

Track fitting

A linearized χ^2 fit is performed using all of the stubs in the candidate tracks, i.e. the stubs used to make the tracklet and the matched stubs are all used for the final fit. The measured ϕ and z (or r) positions of the track on the i layer (or disk) are labeled as f_i^m. Comparing the measured positions with the track projection $f_i(\vec{\eta})$ the χ^2 is defined as:

$$\chi^2 = \sum_{ij}(f_i(\vec{\eta}) - f_i^m)V_{ij}^{-1}(f_j(\vec{\eta}) - f_j^m) \tag{6.6}$$

where V_{ij} is the ij element of the diagonal matrix of the variances σ_{ij}^2. The projection $f_i(\vec{\eta})$ can be expanded around the seed parameters $\vec{\eta}$ giving $f_i(\vec{\eta}) = f_i(\bar{\eta}) + \Delta\vec{\eta}\frac{\partial f_i}{\partial \vec{\eta}}$. This expansion is substituted into the χ^2 equation. To find the best estimate of track parameters, the χ^2 is minimized.

From the minimized χ^2 equation, a linear expression is extracted for $\Delta\eta$ (how the track parameters should be updated given a set of residuals Δf^m with respect to the seed track). The value of $\Delta\eta$ is calculated by:

$$\Delta\eta = (D^{\mathrm{T}}V^{-1}D)^{-1}D^{\mathrm{T}}V^{-1}\Delta f^m \tag{6.7}$$

where $D_{ik} = \frac{\partial f_i}{\partial \eta_k}$. By precalculating $(D^{\mathrm{T}}V^{-1}D)^{-1}D^{\mathrm{T}}V^{-1}$ and storing this in a LUT, the expression for $\Delta\eta$ can be easily computed on an FPGA. The final track parameters are calculated by correcting the original tracklet parameters by $\Delta\eta$.

Seeding, as mentioned above, can occur multiple times per track in order to keep the track finding efficiency high. Duplicated tracks need to be removed from the final track collection. This is accomplished by comparing the found tracks in pairs, and comparing their number of individual and shared stubs. As shown in Fig. 6.10, the duplicate removal step ensures that for a single track

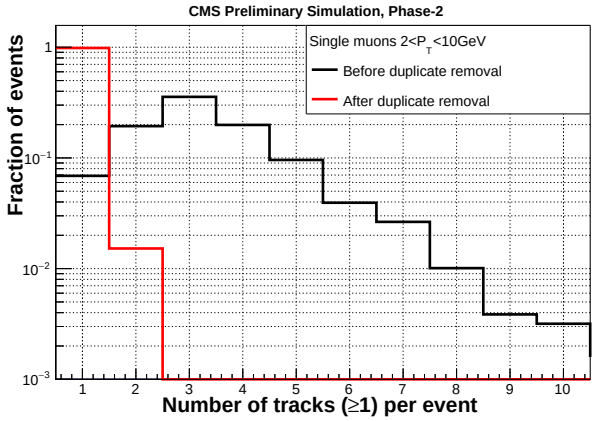

Figure 6.10: Number of tracks found per single muon event before (black) and after (red) the removal of duplicate tracks.

event a single track is found. This helps with the output track rate and is a necessary step in the tracklet algorithm.

6.3.2 Emulation performance results

Several metrics are important for evaluating the performance of the tracklet algorithm. The track finding efficiency and track parameter resolutions are of primary importance. These metrics need to be evaluated for various different physics events (e.g. muon and $\mathrm{t\bar{t}}$ events) and for several different pileup scenarios. These are evaluated for simulated events in an integer-based emulation of the algorithm. In the emulation, all calculations are done in integer quantities, as in the firmware implementation. Therefore, these studies provide an accurate estimate of the final system performance.

The efficiency for finding tracks for single lepton events as a function of p_{T} and η are shown in Fig. 6.11. As expected, the electron efficiency is slightly worse because of kinks in their tracks due to multiple scattering. Efficiency and

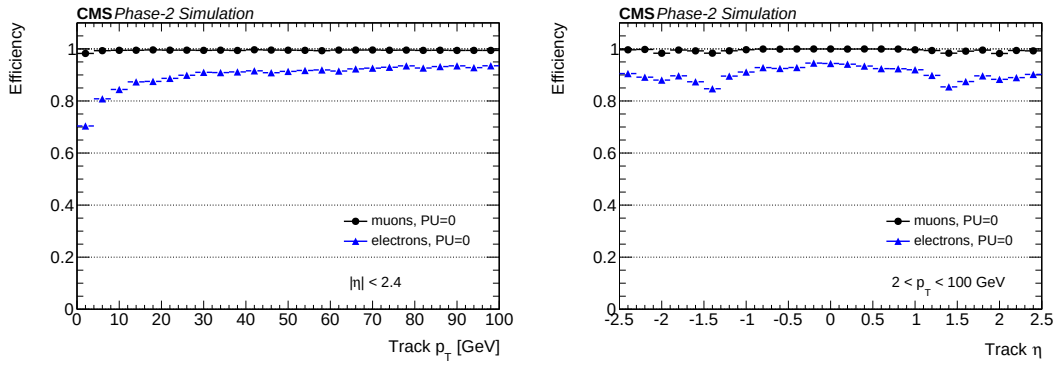

Figure 6.11: Track-finding efficiency for muons (black) and electrons (blue) without pileup as a function of p_{T} (left) and η (right).

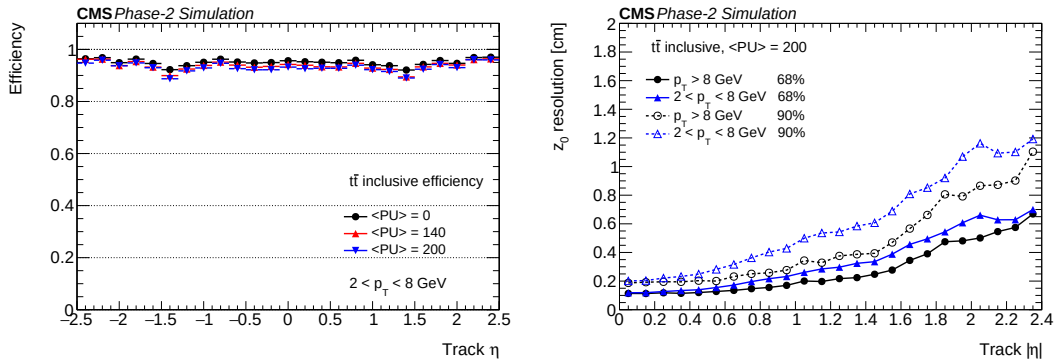

Figure 6.12: Efficiency (left) and z_0 resolution (right) for $\mathrm{t\bar{t}}$ events with pileup.

resolutions for denser events, eg. $\mathrm{t\bar{t}}$ events with pileup, are shown in Fig. 6.12. It is seen that efficiency remains high for the various pileup scenarios. The z_0 resolution is shown for a pileup of 200, the densest environment expected at the HL-LHC. In this case, the z_0 resolution is comparable to 1 mm, the average separation of vertices at 200 pileup, and therefore has a good enough resolution for the L1 trigger. Finally, since all output tracks will go into making the trigger decision, it is important to have a good understanding of the output rate. This can be seen in Fig. 6.10. For a single muon event, the tracklet approach finds exactly one track 99% of the time.

Since the algorithm operates at a fixed latency, there is only a fixed amount of time to continue to process the inputs for each step of the algorithm. Therefore,

events with many tracks in a single ϕ sector can be truncated during processing. In all of the performance plots, the results include the effect of truncation. However, the effects of truncation are small primarily because: (i) the algorithm is highly parallelized, as will be described in the following section, so seldom are there too many inputs that the algorithm does not have enough time to process these events, and (ii) different seeding combinations provide additional redundancy that can recover tracks that are lost.

These plots show that the tracklet algorithm has high track finding efficiency, while meeting the track parameter resolution needs and other demands of the L1 trigger. Additionally, several failure scenarios have been studied in detail and are presented in Ref. [113]. The loss of a full layer, for example, does not have a drastic effect on the tracklet algorithm because the seeding redundancy helps maintain a high performance even in this case.

6.3.3 Hardware Implementation

As was shown in Sec. 6.3.1, the tracklet algorithm involves only a few calculations. Derivatives (for example, how the track parameters change as a function of the matched stubs' residuals) are precomputed and stored in look-up tables for quick retrieval during running. Most of the challenges in this algorithm arise from the large amount of data coming in, which necessitates large partitioning of the data for effective parallel processing.

The main parallelization is the division of the detector into sectors in the r-ϕ plane. The current project uses nine ϕ sectors, to match with the DTC (read out) regions of the tracker. There is some data duplication on the boundaries of

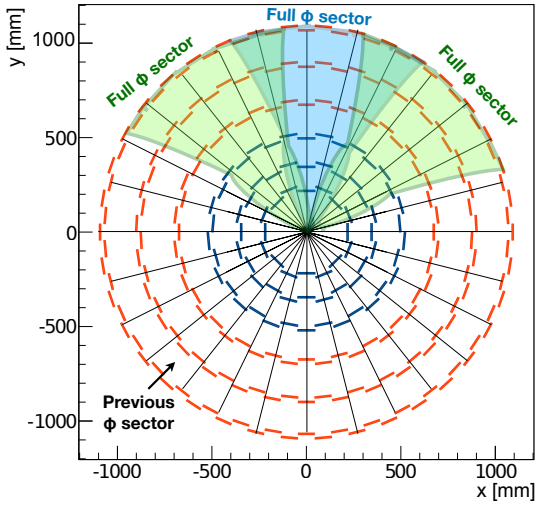

Figure 6.13: Sector boundaries in the r-ϕ plane. Three ϕ sectors, including the regions of duplication between them are shown in shaded blue and green.

these sectors, so that any $p_{\mathrm{T}} > 2$ GeV track will be located fully within a sector. This removes the need for neighboring sector communication. The hourglass-shaped sectors that have these data duplication regions are shown in Fig. 6.13. Further ϕ partitioning within the algorithm makes for more efficient processing and is described in more detail later.

To allow for more time to do the track finding, the whole nine ϕ sector system is replicated n times using a round-robin time-multiplexing approach. Each independent time-multiplexed system receives a new event every $n \times 25$ ns (n times the expected bunch spacing at the HL-LHC). The choice of n is determined by a balance of the needed processing power and the cost. Reasonable choices for the full system are $n = 12$ or $n = 18$. The current implementation of the firmware assumes $n = 12$, meaning a new event is received every 300 ns.

In order to implement the tracklet algorithm on an FPGA, the algorithm is setup as a series of processing steps [105, 106]. All processing steps follow a

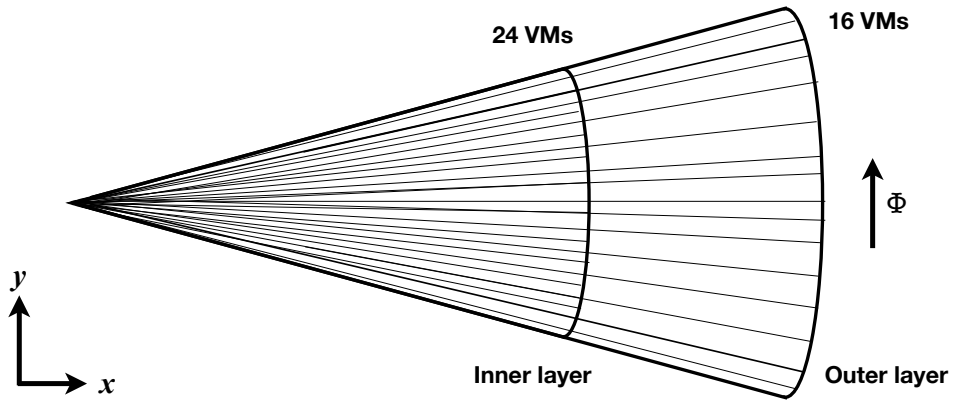

Figure 6.14: Sketch of the virtual module partitioning. Inner (outer) layers in the tracklet seed are split into 24 (16) VMs.

similar format where the input is read from memories filled by a previous step and the output is written to another set of memories. As soon as a new event arrives, the next step in the chain will start processing the previous event. This effectively pipelines the algorithm, so that at any time, each processing step is running on a different event. The following paragraphs describe more about each processing step (names in italics).

Stub organization dominate the first few steps of the algorithm. Incoming stubs are sorted by layer or disk in the *Layer Router*. The stubs are further subdivided into smaller units in ϕ and z ("virtual modules" or VMs) by the *VM Router*. Fig. 6.14 shows the VM partitioning of the system.

The largest combinatoric challenges occur at tracklet formation and match finding. With an average pileup of 140, there are about 80-180 stubs in each layer per ϕ sector. This would yield up to approximately 30,000 candidate tracklets per seeding combination. It is unfeasible and unnecessary to try all of these combinations since many will not make $p_{\mathrm{T}} > 2\ \mathrm{GeV}$ tracks. The VM partitioning, in addition to enabling parallelization of the processing for these steps, also

eliminates the need to try all stub pairs in the sector. These VMs are chosen such that a $p_{\mathrm{T}} > 2\ \mathrm{GeV}$ track could span only a limited set of valid VM combinations between consecutive layers. This reduces the combinations of stub pairs needed to be looped over to make tracklets.

Pairs of stubs are selected as candidate tracklets in the *Tracklet Engine*. Based on the VM partitioning, the number of possible tracklets per VM pair is reduced to 8 on average. Next, in the *Tracklet Calculator*, the tracklet parameters for each pair of stubs is calculated. From the tracklet parameters, projections to all other layers and disks are made. The *Projection Router* routes the projections based on which VM they project into on each layer.

In the *Match Engine*, the projections and stubs are matched by VM. As before, only certain VM combinations are consistent with $p_{\mathrm{T}} > 2\ \mathrm{GeV}$ tracks. The projection-stub difference in positions between the two are calculated in the *Match Calculator*. All stubs matching the trajectory (including the original tracklet stubs) are included in the χ^2 fit, and the final track parameters are extracted in the *Track Fit*. Finally duplicated tracks are removed during the *Duplicate Removal* module.

6.3.4 Hardware demonstrator

Since finding tracks in the dense environment of the HL-LHC is challenging, and because finding tracks in 4 μs is a completely new challenge, the CMS Collaboration requested that a hardware system be set up that can demonstrate the track finding algorithm is actually feasible within these constraints. The main goals of the demonstrator were to: (i) implement the full track finding algorithm

in firmware (ii) achieve bit-to-bit compatibility with integer emulation to make performance estimates, (iii) measure the track finding latency, and (iv) estimate the resource usage of the full project based on the implementation in current technology. All of these goals were achieved by the demonstrator system described in this section.

At the time of the demonstrator, the partitioning of the system was slightly different than the current implementation. The detector was split into 28 ϕ sectors ("original" sectors are also shown in Fig. 6.13). Because the of the finer detector partitioning, a lower time-multiplexing factor ($n = 6$) was achievable. However, the original sectors did not include any overlap between their nearest neighbor. A $p_{\mathrm{T}} > 2\ \mathrm{GeV}$ track would span at most two ϕ sectors, so communication between the original sector and its two nearest neighbors was necessary.

A system hardware demonstrator was set up for this full scale testing of the firmware implementation. The demonstrator test stand is one slice of the time-multiplexed system and it includes three ϕ sector processing boards: one for the central ϕ sector, and one for each of its nearest neighbors. One additional processing board has the duplicate function of sending stubs into the sector processors and receiving the final output tracks. A schematic of this set up is shown in Fig. 6.15.

This demonstrator system is made of four μTCA blades [114], called CTP7 boards [115]. The CTP7s were developed for the current CMS L1 trigger. Each board consists of a Xilinx Virtex-7 (XC7VX690T) FPGA [116] and a Xilinx Zynq-7000 system on chip [117] processor for configuration of the main FPGA and outside communication. An AMC13 [118] card provides a central clock distribution that synchronizes the CTP7 boards. An 8b/10b encoding and 10 Gbps

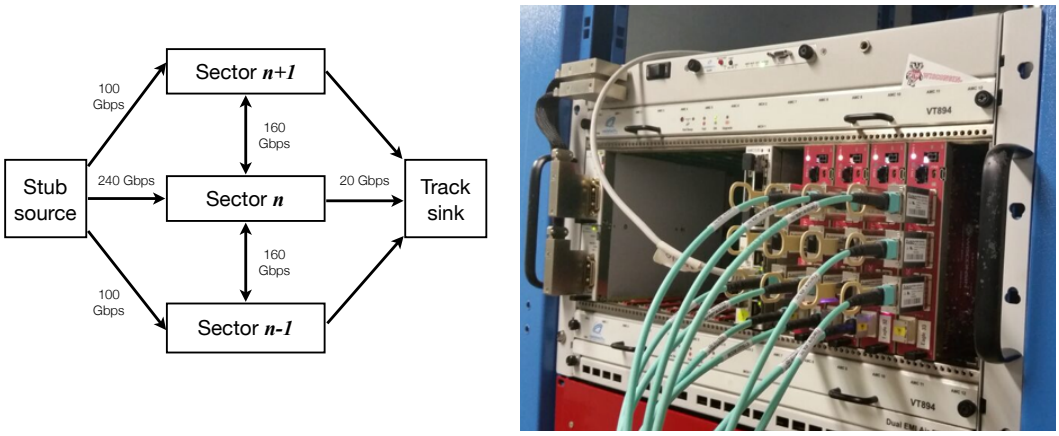

Figure 6.15: Overview (left) and image (right) of the tracklet demonstrator system. In the hardware, the stub source and track sink are one board. Estimated data transfer rates between each board are also shown on the schematic.

links are used for inter-board communication. Although the final system (discussed in more detail in Sec. 6.3.6) will use newer FPGA technology, this is a proxy for a slice of the final system.

The full tracklet algorithm, including all processing steps and transmission of data, is implemented in the firmware running on the demonstrator system. Two complete implementations – one for a half of the barrel ($+z$) and one for a quarter of the barrel plus the forward endcaps – were used to demonstrate the algorithm for the full η range of the CMS detector.

The demonstrator system achieved excellent agreement with the integer emulation as shown in Fig. 6.16. For single muon events, the firmware and emulation final tracks were in 100% agreement. Final tracks in dense $\mathrm{t\bar{t}}$ plus 200 pileup events agreed to better than 99%. These results instill confidence that the firmware is well-understood and behaving as expected. The integer emulation models well the firmware and can therefore be used to evaluate the performance of the system. The latency measured on the demonstrator system and projec-

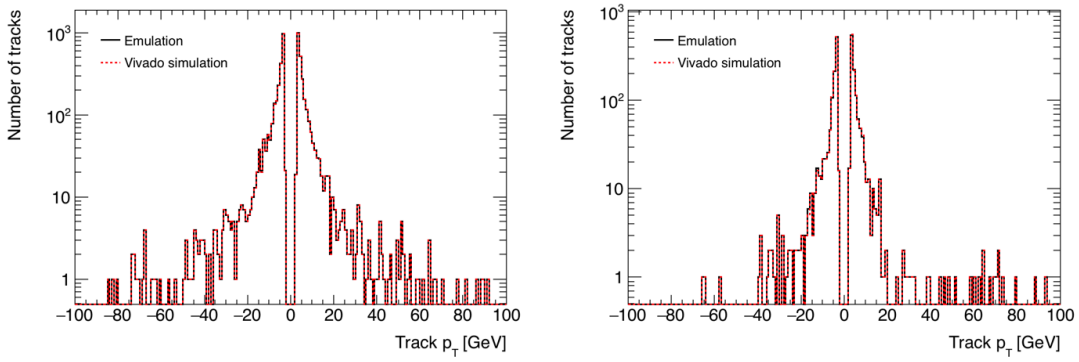

Figure 6.16: Comparison of the hardware (red) and emulation (black) track p_{T} in pileup 200 $\mathrm{t\bar{t}}$ events for the barrel (left) and forward region (right) implementations.

tions for a full system are detailed in Sec. 6.3.5 and Sec. 6.3.6, respectively. This hardware demonstrator system shows that the tracklet algorithm can be implemented and achieves necessary performance goals for the L1 track finding.

Since the time of this test stand, several updates and improvements to the tracklet algorithm have been implemented. The main updates since the demonstrator are:

- The virtual modules are reconfigured so that they cover the full length in z (r) for the barrel (endcaps) but are thinner in ϕ. This reduces the combinatorics in the Tracklet Engines and Match Engines and improves the track finding efficiency in dense jet environments. This has minimal effect on the resource usage of the algorithm.
- The ϕ sector definition is changed, and now includes hourglass-shaped areas of duplicated data to remove the need for neighbor sector communication (thus removing the associated latency). The larger sector requires more processing though, and the time-multiplexing factor has to at least double for each processing step (currently $n = 12$ instead of $n = 6$).

- The baseline CMS tracker detector geometry is also changed. It is expected to have tilted (in η) modules in the inner barrel (layers 1, 2, and 3) as shown earlier in Fig. 6.2. The tracklet algorithm underwent minor calculation adjustments to compensate for this change.

A future hardware demonstrator, using track finding board prototypes (discussed later) will include all of these changes.

6.3.5 System latency

Because each of the processing steps of the tracklet algorithm operates at a fixed latency, it is straight forward to model the overall latency of the system. Table 6.1 gives the breakdown of the latency per processing step.

The "step latency" refers to the time it takes from the first piece of data into each step to the first data out. It is the intrinsic overhead of the calculations of that processing step. In Table 6.1 it is listed in both clock cycles (CLK) and in nanoseconds, assuming that the FPGA is running at 240 MHz (the achieved clock speed of the demonstrator). The additional "processing time" is the time allotted for the step to output the remaining outputs before the next event starts. The length of the processing time is determined by the time-multiplexing factor $n \times 25$ ns. For the demonstrator system $n = 6$, so a new event arrives every 150 ns therefore each step finishes its previous bunch crossing processing at 150 ns.

Several processing steps also involve data transfer over links. For example, the stubs must be sent into the track finding system, and the final tracks must be sent out to the L1 correlator. In the demonstrator, neighbor sector communica-

Table 6.1: The latency model for the hardware system is shown. For each step, the processing time and latency is given. For steps involving data transfer, the link latency is given.

Step	Proc. time (ns)	Step latency (CLK)	Step latency (ns)	Link delay (ns)	Step total (ns)
Input link	0.0	1	4.2	316.7	320.8
Layer Router	150.0	1	4.2	—	154.2
VM Router	150.0	4	16.7	—	166.7
Tracklet Engine	150.0	5	20.8	—	170.8
Tracklet Calculation	150.0	43	179.2	—	329.2
Projection Transceiver	150.0	13	54.2	316.7	520.8
Projection Router	150.0	5	20.8	—	170.8
Match Engine	150.0	6	25.0	—	175.0
Match Calculator	150.0	16	66.7	—	216.7
Match Transceiver	150.0	12	50.0	316.7	516.7
Track Fit	150.0	26	108.3	—	258.3
Duplicate Removal	0.0	6	25.0	—	25.0
Output Link	0.0	1	4.2	316.7	320.8
Total	1500.0	139	579.2	1266.7	**3345.8**

tion is needed to send projections to neighbor ϕ sectors and send matched stubs back to the original sector. The streaming of the data is handled by a priority encoder so there is very little overhead. However, based on measurements of 8b/10b encoding on 10 Gbps links of the demonstrator system (which uses 15 m cables) there is a 316.7 ns delay between sending and receiving data. This adds an intrinsic latency of about 1 μs to the system ("link delay" in Table 6.1).

Taken all together, the overall latency of the project can be modeled. From Table 6.1 it is seen that the first track out for each event will take 3345.8 ns. The last track out, by design, will not appear beyond 150 ns after that.

By implementing the tracklet algorithm on the hardware demonstrator described before, the latency can be measured on a real system as well. The track source/sink board has a counter which starts when the data starts being sent out

of the system and finishes when the tracks start being received on the board. Based on this, the measured latency of the system is 800 clock cycles, which translates to 3333 ns. The measured latency agrees within three clock cycles or 0.4% with the modeled latency. The measured (and modeled) latency is already below the goal of 4 μs for L1 tracks.

Several modifications to the latency are expected based on updates to the project since the time of the demonstrator (updates mentioned in the previous section). The largest changes with respect to the latency are the removal of the Projection Transceiver and Match Transceiver steps and the increase in the time-multiplexing factor to compensate for the increased data rates in each sector. Additionally, the link latency will be reduced because of improved link speed and protocol. For example, 64b/66b rather than 8b/10b encoding is now possible. The expected latency of the tracklet algorithm with these changes is shown in Table 6.2. The expected latency is under 3 μs with these changes which is well within the latency budget available. The exact optimization of the algorithm in terms of the hourglass sector configuration is still under investigation.

6.3.6 Projections for the full system

The full L1 track system will look like the system shown in Fig. 6.17. Data will be read off the tracker by the DTC. The stubs will then be sent to the track finder system. There will be n time-multiplex (TMUX) copies of the track finding system. Each copy has a sector processing board per ϕ sector. The output tracks are sent to the trigger correlator where tracks are correlated with trigger objects from the calorimeters and muon systems. Optical links between the DTC and

Table 6.2: The estimated latency without sector-to-sector communication and with a time-multiplexing factor of 12. Same clock speed (240 MHz) as the demonstrator is assumed.

Step	Proc. time (ns)	Step latency (CLK)	Step latency (ns)	Link delay (ns)	Step total (ns)
Input link	0.0	1	4.2	150.0	154.2
VM Router	300.0	4	16.7	-	316.7
Tracklet Engine	300.0	5	20.8	-	320.8
Tracklet Calculation	300.0	43	179.2	-	479.2
Projection Router	300.0	5	20.8	-	320.8
Match Engine	300.0	6	25.0	-	325.0
Match Calculator	300.0	16	66.7	-	366.7
Track Fit	300.0	26	108.3	-	408.3
Duplicate Removal	0.0	6	25.0	-	25.0
Output Link	0.0	1	4.2	150.0	154.2
Total	2100.0	113	470.8	300.0	**2870.8**

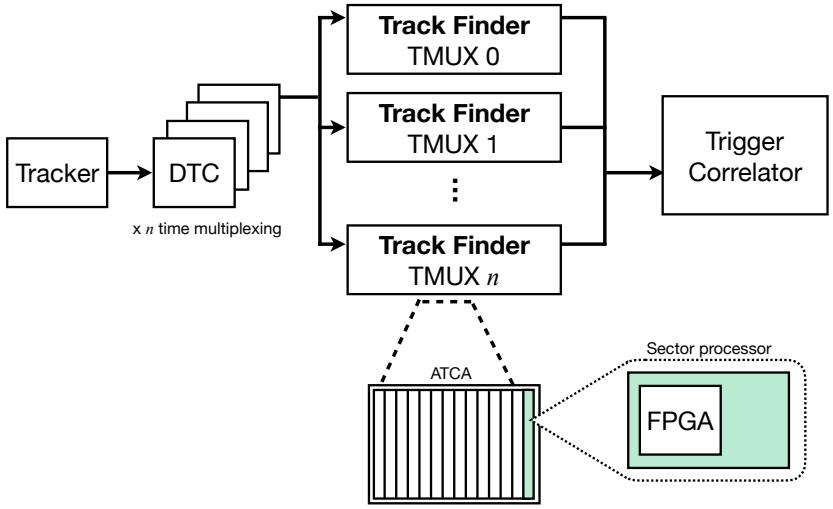

Figure 6.17: Sketch of the proposed L1 tracking system.

track finder boards need to be operated at 25 Gbps to be able to read all of the data from the outer tracker in time.

Prototypes of the sector processing boards are currently under design. The printed circuit board (PCB) will ultimately be an ATCA [119] blade with an

Table 6.3: The top line shows estimated FPGA resource needs for a full ϕ sector. The following lines show the fraction of the resource needs in a Virtex-7 and Virtex Ultrascale+ FPGAs.

	LUT Logic	LUT Memory	BRAM	DSP
Full sector	279733	151191	2721.5	1818
Virtex-7 690T	65%	87%	185%	51%
VU3P	32%	81%	85%	80%
VU5P	21%	53%	58%	52%
VU7P	16%	40%	42%	40%
VU9P	11%	27%	28%	27%
VU11P	10%	27%	29%	20%
VU13P	7%	20%	22%	15%

FGPA on a mezzanine card. The boards will have a system on chip processor that can be used for slow control and communication with the main FPGA. And the ATCA boards will have many high speed links (16 or 25 Gbps) to receive data from the DTC and send tracks to the trigger correlator. In each ATCA shelf, an AMC13 board (as described in the demonstrator system) will be used for clock distribution and communication with the LHC.

Based on the need for 25 Gbps links and based on resource estimates for the algorithm (shown in Table 6.3), the processing will need to happen on a Virtex Ultrascale+ FPGA [120]. The estimated resource utilization for a ϕ sector is based on the usage as reported by Xilinx's Vivado Design Suite for the demonstrator implementation of a half ϕ sector (the $+z$ region of a ϕ sector).

As a precursor to the prototype, a custom μTCA PCB was designed to start development on the firmware for Ultrascale FPGAs and to test the use of high-speed ($\geq$ 10 Gbps) links. A cartoon schematic of the so-called YUGE ("Your Ultrascale Gigabit Evaluation") board is shown in Fig. 6.18. Also shown is a photo of the YUGE board in the lab.

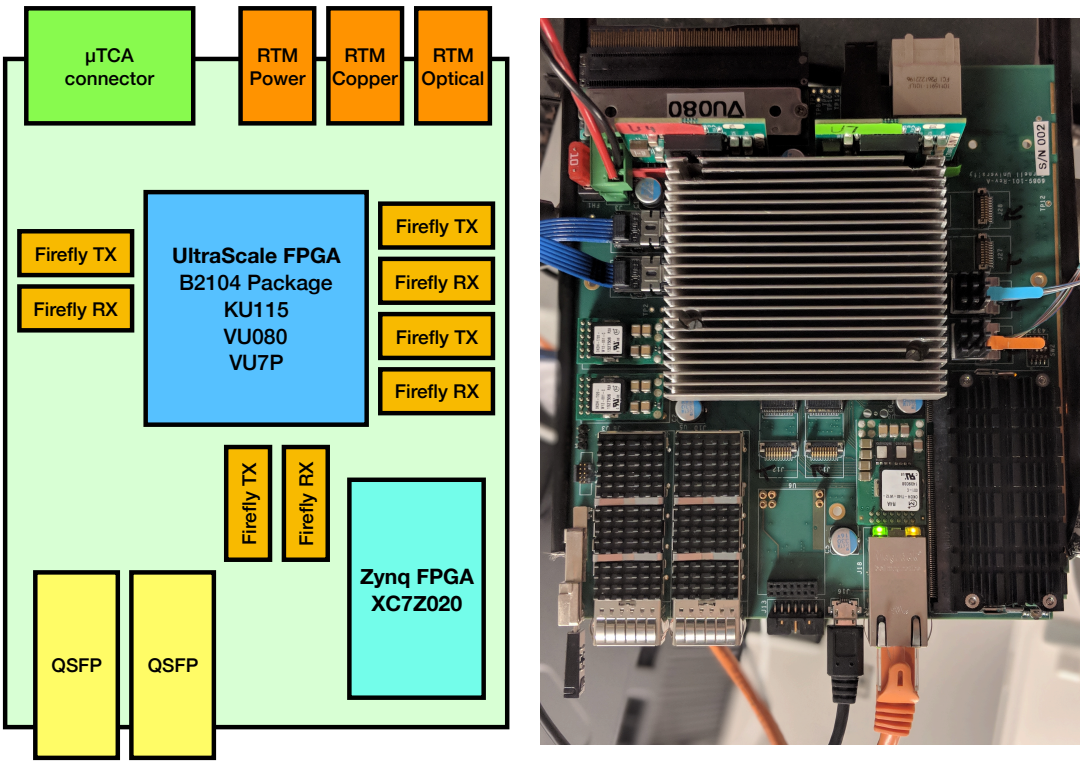

Figure 6.18: Sketch of YUGE components (left) and photo of the YUGE (right).

The YUGE has a ball-grid array that is pin-compatible with several FPGAs. Two YUGE boards have been stuffed with Kintex Ultrascale 115 (KU115) FPGAs. These FPGAs have enough resources to fit a full ϕ sector project, however they can only operate links at 16 Gbps. Two other YUGE boards have Virtex Ultrascale 080 (VU080) FPGAs, which do not enough resources for the full tracklet algorithm, but can run links at 25 Gbps. A comparison of the resources on each of these FPGAs is given in Table 6.4. Also shown are the resources of a Virtex Ultrascale+ 7 (VU7P) FPGA which is also pin-compatible, because it is a feasible chip for the final system (capable of operating links at 25 Gbps and has sufficient resources for the implementation of the algorithm). The VU7P is recently available for purchase.

Table 6.4: Number of links (and their speed) and other resources available on each FPGA that is or will be used on the YUGE board.

Device	Available links	DSP	BRAM (Mb)	DRAM (Mb)
KU115	64 @ 16.3 Gbps	5520	75.9	18.36
VU080	32 @ 16.3 Gbps, 32 @ 28.2 Gbps	672	50.0	3.96
VU7P	76 @ 28.2 Gbps	4560	50.6	24.10

Several other features of the YUGE board are notable. A preassembled Enclustra Mars ZX2 [121] is attached to the YUGE. The Enclustra module is composed of a Zynq 7020 [117] system on chip, which is a small FPGA and dual ARM processing cores (running CPUs). The Zynq provides the primary interface from the outside to the main FPGA. Additionally, the Enclustra module has 512 Mb of memory for the operating system and any applications running on the Zynq. Ethernet access is available for outside communication with the YUGE board. Also as a μTCA board, the YUGE has a black plane that can transmit data between boards in the same crate.

In order to test different commercial link options, there are several different link interfaces on the YUGE board. Firefly links [122] are available in both copper and optical link forms. Copper links are rated up to 28 Gbps the speed limit for the VU080 transceiver banks. Optical Firefly links can be run up to 14 Gbps. The Firefly transceivers on the PCB have 12 TX (output) and 12 RX (input) ports. This allows for highly parallelized data transmission. A second set of link transceivers on the YUGE board are QSFP transceivers [123]. These links are also available in copper or optical form and are capable of 28 Gbps transmission. QSFP transceivers have 4 TX and 4 RX ports. Additionally, data can be transmitted via the rear transmission module on the back edge of the PCB. This is a way to quickly communicate with other PCBs in the same crate.

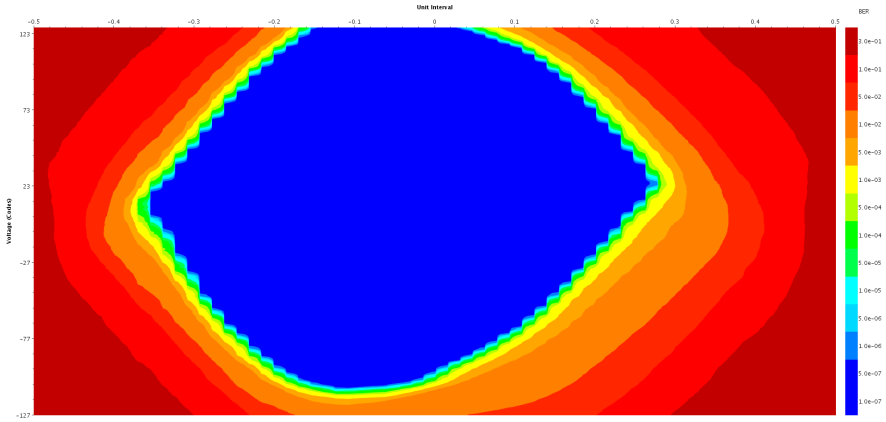

Figure 6.19: Example scan for a QSFP copper link running at 25 Gbps.

In order to evaluate the integrity of the different link options, bit error ratio tests were performed [124]. By sending known data sequences through the links many times, it is possible to evaluate the number of errors received during transmission. An eye-diagram is a plot of the number of errors as a function of unit time and voltage. The center of the eye-diagram is the nominal operation of the links, so an eye-diagram with a large open area means that the link has very low bit-flip errors during the majority of operation. An example eye-diagram for the YUGE board is shown for a copper QSFP link operating at 25 Gbps in Fig. 6.19. Eye-diagrams are used to choose optimal parameters for the transceivers, and prove that all on-board link options function well even at high speeds.

The YUGE board was the CMS experiment's first custom PCB to demonstrate 25 Gbps links are feasible. This is an important achievement for implementing high speed links. The ATCA prototype, that will be produced within the year, will make use of these links as well. The full system will be composed of around 170 track finding boards that each have high speed links to read incoming data quickly and Ultrascale+ FPGAs to do the majority of the processing. There is an ongoing effort in synchronizing the design between the

track finding and DTC boards. Mezzanine cards with the main FPGA allow for the flexibility of using the ATCA base for multiple PCBs in the final system.

6.4 Summary

The HL-LHC will have an average of 200 simultaneous pp collisions. In order to maintain physics performance while keeping data rates manageable, CMS will need charged particle tracking at the L1 trigger level. Tracking for this system will need to be completed on dedicated hardware within 4 μs.

The tracklet algorithm is a road-search approach to charged particle track finding and reconstruction that is implemented on commercially available FPGAs. Pairs of hits in adjacent layers are used to estimate initial track parameters. The track is projected to other layers of the tracker to look for matching hits. A χ^2 fit is used to correct the original estimate and extract the final track parameters. Partitioning in ϕ and time-multiplexing allow for efficient parallel processing to handle the combinatorics inherent in the HL-LHC environment.

Performance estimates for the tracklet algorithm are promising. The tracklet algorithm has high track finding efficiency for various different physics events and pileup scenarios. The resolution of the track parameters meets the demands of the L1 trigger. And it has been demonstrated that track finding is feasible in under 4 μs, thus meeting the latency demands on the system. Based on estimates from the current implementation of the tracklet algorithm, the final track finding system will be composed of Ultrascale+ FPGAs on ATCA boards. Optical links operating at 25 Gbps will transfer data from the tracker to the track-finder. Prototypes of these boards are expected this year.

CHAPTER 7

CONCLUSION

This thesis has presented the results of a search for dark matter particles produced in association with a Higgs boson decaying to two photons. The analysis uses proton-proton collision data collected at a center-of-mass energy of 13 TeV at the CMS detector at the CERN Large Hadron Collider. The data taken in 2015 and 2016 correspond to an integrated luminosity of 2.2 and 35.9 fb^{-1}.

Selected collision events with two photons are split into categories based on their transverse momentum imbalance. A maximum-likelihood fit to the diphoton invariant mass is used to extract the signal significance and place 95% confidence level exclusion limits. For a Z′-two-Higgs-doublet-model, signals with a pseudoscalar $m_{\mathrm{A}} = 300\ \mathrm{GeV}$ and with dark matter mass at or below 100 GeV are excluded for Z′ masses from 550 to 860 GeV. For a baryonic Z′ signal with $m_{\mathrm{DM}} = 1\ \mathrm{GeV}$ this search excludes Z′ masses up to 574 GeV. These results are also extrapolated to exclusion limits on spin-independent cross section for dark matter-nucleon interaction which are more stringent than direct detection experiments' for dark matter masses between 1 and 2 GeV.

An FPGA-based proposal for charged particle track reconstruction is also presented. To cope with the high pileup environment at the High-Luminosity LHC, tracking will need to be included at the hardware trigger level. The tracklet approach is a road-search algorithm that utilizes massive data partitioning to accomplish track finding and reconstruction in under 4 μs. The performance of a hardware demonstrator of the tracklet system convinced the CMS experiment to pursue an all FPGA (rather than ASIC) approach for the final system, and the prototype hardware is being developed.

APPENDIX A

ALTERNATIVE MONO-H SEARCH APPROACH

This section briefly summarizes the Mono-h analysis approach that was preformed on the 2015 data set. It is useful as a discussion of an alternative background estimation method. As mentioned earlier, the trigger was almost identical in 2015 and 2016, and most of the photon identification and event selection criteria are similar to that of the 2016 analysis. The specific details of the 2015 analysis can be found in Ref. [28] with some additional information about selection detailed in Ref. [78].

For this search, a "cut-and-count" method was chosen that uses an "ABCD" estimation of the background. In the case of this analysis, a signal region (D) is defined as the region with events that have $120\ \mathrm{GeV} < m_{\gamma\gamma} < 130\ \mathrm{GeV}$ and $p_{\mathrm{T}}^{\mathrm{miss}}$ above the threshold of 105 GeV. The signal-free control regions are then used to estimate the nonresonant background in the signal region. The regions can be seen in the illustration in Fig. A.1. The resonant background estimation is taken from simulation, as done in the 2016 analysis.

Provided the two variables used to setup the ABCD regions are uncorrelated (they were to less than 10%), then the number of background events in the signal region can be estimated from the number of events in the sidebands by $N_D = \alpha N_A$ where $\alpha = N_C/N_B$. To make this procedure more robust, the transfer factor α was derived from a fit to the $m_{\gamma\gamma}$ distribution in the sideband region:

$$\alpha = \frac{\int_C f(m_{\gamma\gamma})\,\mathrm{d}m_{\gamma\gamma}}{\int_B f(m_{\gamma\gamma})\,\mathrm{d}m_{\gamma\gamma}}. \tag{A.1}$$

Several analytic functions were fit to the observed $m_{\gamma\gamma}$ distribution in the low-$p_{\mathrm{T}}^{\mathrm{miss}}$ region. A power law function was chosen as the final estimate based

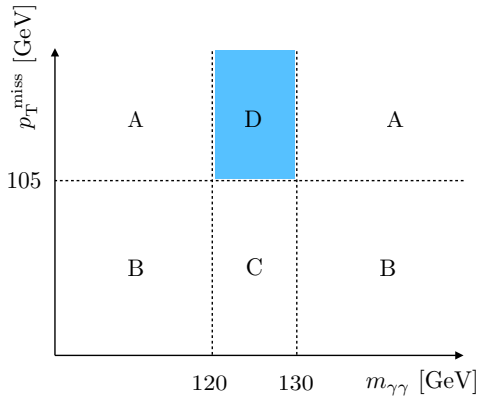

Figure A.1: Sketch of the ABCD regions in the 2015 analysis. The D region (shown in blue) is the signal region. The A, B, and C regions are used to extract the nonresonant background contribution to D.

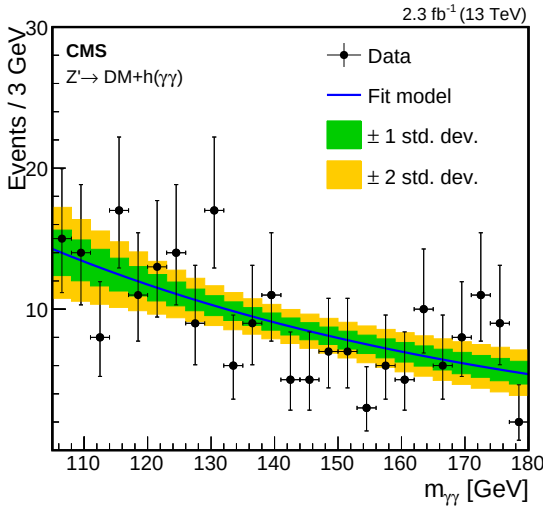

Figure A.2: Fit to the $m_{\gamma\gamma}$ distribution in the low-p_T^{miss} control region in data collected at CMS in 2015. The fit is used to evaluate the transfer factor α.

on a bias study similar to that of the 2016 analysis (described in Sec. 5.7.2). Within the uncertainties, α is independent of the p_T^{miss} threshold and is consistent between data and simulation. The fit in the low-p_T^{miss} region of the $m_{\gamma\gamma}$ distribution of the 2015 data set is shown in Fig. A.2. This fit yielded a transfer factor $\alpha = 0.190 \pm 0.035$ (stat).

In the 2015 data set, there were two events observed in the $m_{\gamma\gamma}$ sidebands

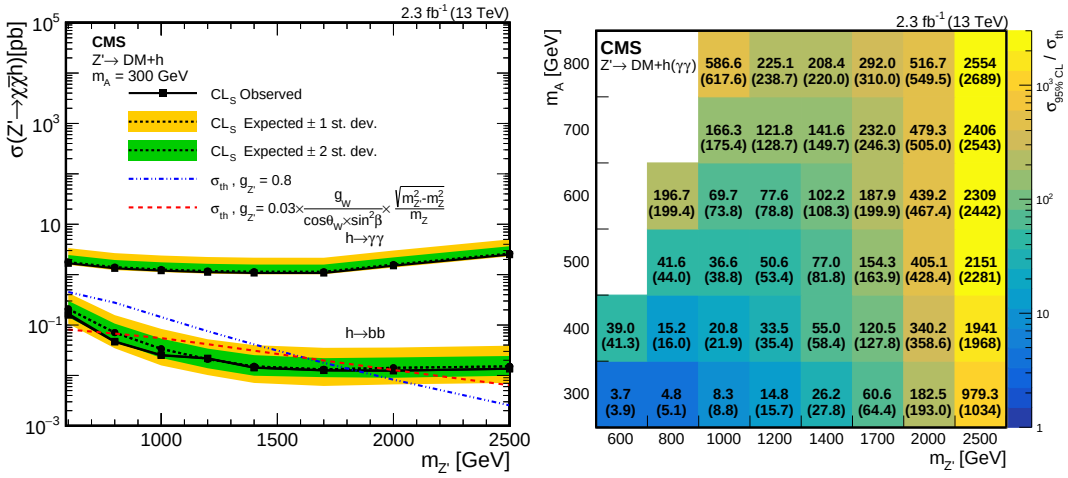

Figure A.3: Upper limits on Z′-2HDM cross section (left) and signal significance (right) extracted from the results of the ABCD method with the 2015 data set [28].

with $p_{\mathrm{T}}^{\mathrm{miss}} > 105$ GeV. Based on this, it was expected that there would be $0.38 \pm 0.08\,(\mathrm{stat})$ nonresonant background events in the signal region. Zero events were observed in the signal region. Therefore upper limits were made on the Z′-2HDM cross section, as shown in Fig. A.3.

This method has comparable sensitivity to dark matter signals as that of the fit method used in the 2016 analysis. This can be seen in the comparison of the exclusion limits shown in Fig. A.4. However, the 2015 data set was so statistically limited, that there were not enough events to preform a fit of the $m_{\gamma\gamma}$ distribution in the high-$p_{\mathrm{T}}^{\mathrm{miss}}$ region so this "cut-and-count" approach was chosen instead. The increase in the statistical power of the 2016 data set allowed the use of the fit to the $m_{\gamma\gamma}$ distribution. The use of the full fit also allows the low-$p_{\mathrm{T}}^{\mathrm{miss}}$ region to be used as a signal region, making the approach more model independent. However, the search strategy detailed in this Appendix is very effective for probing specific models.

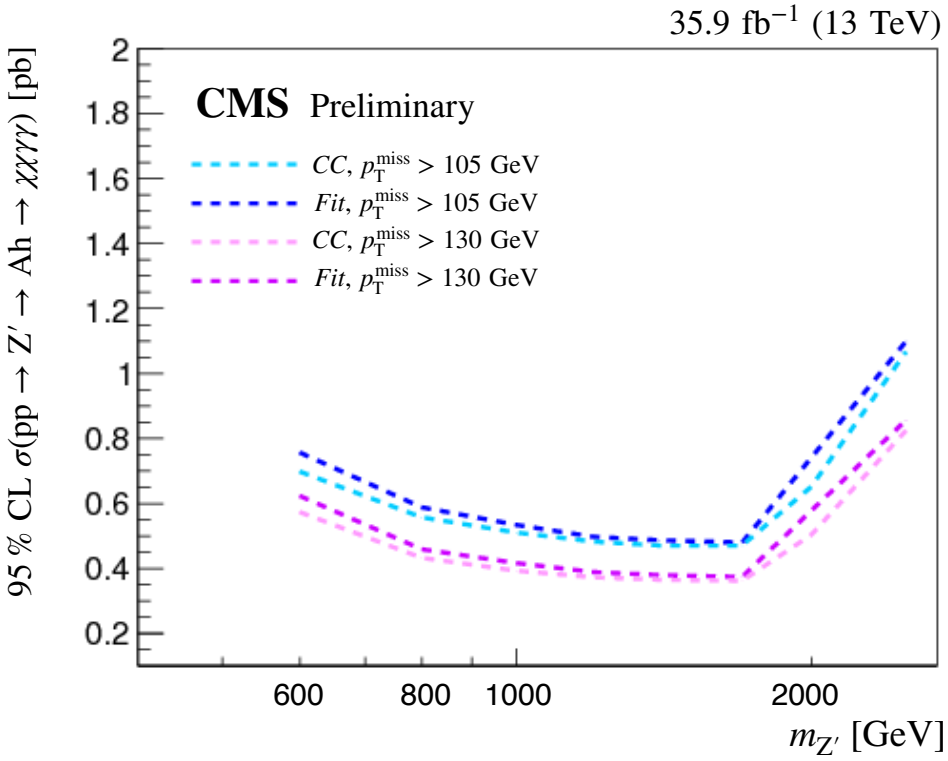

Figure A.4: Comparison of the expected 95% CL exclusion limits with the 2016 data set for the Z′-2HDM signal between the "cut-and-count" (CC) and fit methods. Limits are shown for the p_T^{miss} thresholds of 105 GeV (blue) and 130 GeV (pink) which correspond to the 2015 and 2016 analysis thresholds, respectively.

BIBLIOGRAPHY

[1] Particle Data Group, M. Tanabashi et al., "Review of particle physics", *Phys. Rev. D* **98** (2018) 030001, doi:10.1103/PhysRevD.98.030001.

[2] ATLAS Collaboration, "Observation of a new particle in the search for the standard model Higgs boson with the ATLAS detector at the LHC", *Phys. Lett. B* **716** (2012) 1, doi:10.1016/j.physletb.2012.08.020, arXiv:1207.7214.

[3] CMS Collaboration, "Observation of a new boson at a mass of 125 GeV with the CMS experiment at the LHC", *Phys. Lett. B* **716** (2012) 30, doi:10.1016/j.physletb.2012.08.021, arXiv:1207.7235.

[4] P. Langacker, "The Standard Model and Beyond". CRC Press, 2010. ISBN 978-1-4200-7906-7.

[5] LHC Higgs Cross Section Working Group, D. de Florian et al., "Handbook of LHC Higgs cross sections: 4. Deciphering the nature of the Higgs sector", doi:10.23731/CYRM-2017-002, arXiv:1610.07922.

[6] G. Bertone, D. Hooper, and J. Silk, "Particle dark matter: Evidence, candidates and constraints", *Phys. Rep.* **405** (2005) 279, doi:10.1016/j.physrep.2004.08.031, arXiv:hep-ph/0404175.

[7] D. Clowe et al., "A direct empirical proof of the existence of dark matter", *Astrophys. J. Lett.* **648** (2006) L109, doi:10.1086/508162, arXiv:astro-ph/0608407.

[8] M. Klasen, M. Pohl, and G. Sigl, "Indirect and direct search for dark matter", *Prog. Part. Nuc. Phys.* **85** (2015) 1, doi:10.1016/j.ppnp.2015.07.001, arXiv:1507.03800.

[9] Planck Collaboration, "Planck 2018 results. VI. Cosmological parameters", (2018). arXiv:1807.06209.

[10] K. G. Begeman, A. H. Broeils, and R. H. Sanders, "Extended rotation curves of spiral galaxies: dark haloes and modified dynamics", *MNRAS* **249** (1991) 523, doi:10.1093/mnras/249.3.523.

[11] G. Jungman, M. Kamionkowski, and K. Griest, "Supersymmetric dark matter", *Phys. Rep.* **267** (1996) 195, doi:10.1016/0370-1573(95)00058-5, arXiv:hep-ph/9506380.

[12] T. M. Undagoitia and L. Rauch, "Dark matter direct-detection experiments", *J. Phys. G* **43** (2015) 013001, doi:10.1088/0954-3899/43/1/013001, arXiv:1509.08767.

[13] CMS Collaboration, "CMS exotica summary plots for 13 TeV data". https://twiki.cern.ch/twiki/bin/view/CMSPublic/SummaryPlotsEXO13TeV.

[14] ATLAS Collaboration, "Summary plots from the ATLAS exotic physics group". https://atlas.web.cern.ch/Atlas/GROUPS/PHYSICS/CombinedSummaryPlots/EXOTICS/index.html.

[15] ATLAS Collaboration, "Constraints on mediator-based dark matter and scalar dark energy models using $\sqrt{s}$ = 13 TeV pp collision data collected by the ATLAS detector", *Submitted to JHEP* (2019) arXiv:1903.01400.

[16] D. Abercrombie et al., "Dark matter benchmark models for early LHC Run-2 searches: Report of the ATLAS/CMS Dark Matter Forum", (2015). arXiv:1507.00966.

[17] A. Boveia et al., "Recommendations on presenting LHC searches for missing transverse energy signals using simplified s-channel models of dark matter", (2016). arXiv:1603.04156.

[18] L. Carpenter et al., "Mono-Higgs-boson: A new collider probe of dark matter", *Phys. Rev. D* **89** (2014) 075017, doi:10.1103/PhysRevD.89.075017, arXiv:1312.2592.

[19] A. Berlin, T. Lin, and L. Wang, "Mono-Higgs detection of dark matter at the LHC", *JHEP* **6** (2014) 78, doi:10.1007/JHEP06(2014)078, arXiv:1402.7074.

[20] A. A. Petrov and W. Shepherd, "Searching for dark matter at LHC with mono-Higgs production", *Phys. Lett. B* **730** (2014) 178, doi:10.1016/j.physletb.2014.01.051, arXiv:1311.1511.

[21] ATLAS Collaboration, "Constraints on new phenomena via Higgs boson couplings and invisible decays with the ATLAS detector", *JHEP* **11** (2015) 206, doi:10.1007/JHEP11(2015)206, arXiv:1509.00672.

[22] CMS Collaboration, "Searches for invisible decays of the Higgs boson in pp collisions at $\sqrt{s} = 7$, 8, and 13 TeV", *JHEP* **02** (2017) 135, doi:10.1007/JHEP02(2017)135, arXiv:1610.09218.

[23] ATLAS Collaboration, "Search for dark matter produced in association with a Higgs boson decaying to two bottom quarks in pp collisions at $\sqrt{s} = 8$ TeV with the ATLAS detector", *Phys. Rev. D* **93** (2016) 072007, doi:10.1103/PhysRevD.93.072007, arXiv:1510.06218.

[24] ATLAS Collaboration, "Search for dark matter in events with missing transverse momentum and a Higgs boson decaying to two photons in pp collisions at $\sqrt{s} = 8$ TeV with the ATLAS detector", *Phys. Rev. Lett.* **115** (2015) 131801, doi:10.1103/PhysRevLett.115.131801, arXiv:1506.01081.

[25] ATLAS Collaboration, "Search for dark matter in association with a Higgs boson decaying to b-quarks in pp collisions at $\sqrt{s} = 13$ TeV with the ATLAS detector", *Phys. Lett. B* **765** (2017) 11, doi:10.1016/j.physletb.2016.11.035, arXiv:1609.04572.

[26] ATLAS Collaboration, "Search for dark matter produced in association with a Higgs boson decaying to $\mathrm{b\bar{b}}$ using 36 fb^{-1} of pp collisions at $\sqrt{s} = 13$ TeV with the ATLAS detector", *Phys. Rev. Lett.* **119** (2017) 181804, doi:10.1103/PhysRevLett.119.181804, arXiv:1707.01302.

[27] ATLAS Collaboration, "Search for dark matter in association with a Higgs boson decaying to two photons at $\sqrt{s} = 13$ TeV with the ATLAS detector", *Phys. Rev. D* **96** (2017) 112004, doi:10.1103/PhysRevD.96.112004, arXiv:1706.03948.

[28] CMS Collaboration, "Search for associated production of dark matter with a Higgs boson decaying to $\mathrm{b\bar{b}}$ or $\gamma\gamma$ at $\sqrt{s} = 13$ TeV", *JHEP* **10** (2017) 180, doi:10.1007/JHEP10(2017)180, arXiv:1703.05236.

[29] CMS Collaboration, "Search for dark matter produced in association with a Higgs boson decaying to $\gamma\gamma$ or $\tau^+\tau^-$ at $\sqrt{s} = 13$ TeV", *JHEP* **09** (2018) 046, doi:10.1007/JHEP09(2018)046, arXiv:1806.04771.

[30] CMS Collaboration, "Search for heavy resonances decaying into a vector boson and a Higgs boson in final states with charged leptons, neutrinos, and b quarks at $\sqrt{s} = 13$ TeV", *JHEP* **11** (2018) 172, doi:10.1007/JHEP11(2018)172, arXiv:1807.02826.

[31] CMS Collaboration, "Search for dark matter produced in association with a Higgs boson decaying to a pair of bottom quarks in proton-proton collisions at $\sqrt{s} = 13$ TeV", *Submitted to EPJC* (2018) arXiv:1811.06562.

[32] CMS Collaboration, "Search for dark matter particles produced in association with the Higgs boson in proton-proton collisions at $\sqrt{s}$ = 13 TeV", CMS Physics Analysis Summary CMS-PAS-EXO-18-011, 2019.

[33] J. Alwall et al., "The automated computation of tree-level and next-to-leading order differential cross sections, and their matching to parton shower simulations", *JHEP* **07** (2014) 079, doi:10.1007/JHEP07(2014)079, arXiv:1405.0301.

[34] T. Sjöstrand et al., "An introduction to PYTHIA 8.2", *Comput. Phys. Commun.* **191** (2015) 159, doi:10.1016/j.cpc.2015.01.024, arXiv:1410.3012.

[35] G. C. Branco et al., "Theory and phenomenology of two-Higgs-doublet models", *Phys. Rep.* **516** (2012) 1, doi:10.1016/j.physrep.2012.02.002, arXiv:1106.0034.

[36] N. Craig, J. Galloway, and S. Thomas, "Searching for signs of the second Higgs doublet", (2013). arXiv:1305.2424.

[37] CLEO Collaboration, "Improved measurement of $\mathcal{B}(\mathrm{b} \to \mathrm{s}\gamma)$", *Proceedings of ICHEP '98* **1** (1998) 1057.

[38] P. F. Perez and M. B. Wise, "Baryon and lepton number as local gauge symmetries", *Phys. Rev. D* **82** (2010) 011901, doi:10.1103/PhysRevD.82.011901, arXiv:1002.1754. [Erratum: doi:10.1103/PhysRevD.82.079901].

[39] L. Evans and P. Bryant, "LHC machine", *JINST* **3** (2008) S08001, doi:10.1088/1748-0221/3/08/S08001.

[40] H. Wiedemann, "Introduction to Accelerator Physics". Springer Cham, 2015. doi:10.1007/978-3-319-18317-6, ISBN 978-3-319-18317-6.

[41] CMS Collaboration, "CMS Luminosity - public results". https://twiki.cern.ch/twiki/bin/view/CMSPublic/LumiPublicResults.

[42] ALICE Collaboration, "The ALICE experiment at the CERN LHC", *JINST* **3** (2008) S08002, doi:10.1088/1748-0221/3/08/S08002.

[43] ATLAS Collaboration, "The ATLAS experiment at the CERN Large Hadron Collider", *JINST* **3** (2008) S08003, doi:10.1088/1748-0221/3/08/S08003.

[44] CMS Collaboration, "The CMS experiment at the CERN LHC", *JINST* **3** (2008) S08004, doi:10.1088/1748-0221/3/08/S08004.

[45] LHCb Collaboration, "The LHCb detector at the LHC", *JINST* **3** (2008) S08005, doi:10.1088/1748-0221/3/08/S08005.

[46] J.-L. Caron, "Cross section of LHC dipole", (1998).

[47] J.-P. Burnet, "Putting it into practice", doi:10.5170/CERN-2015-003.445, arXiv:1607.01596.

[48] CMS Collaboration, "Precise mapping of the magnetic field in the CMS barrel yoke using cosmic rays", *JINST* **5** (2010) T03021, doi:10.1088/1748-0221/5/03/T03021, arXiv:0910.5530.

[49] CMS Collaboration, "The CMS tracker : addendum to the technical design report", Technical Report CERN-LHCC-2000-016. CMS-TDR-5-add-1, 2000.

[50] M. Hoch, "CMS pixel detector", (2014).

[51] CMS Collaboration, "The CMS electromagnetic calorimeter project : Technical design report", Technical Report CERN-LHCC-97-033. CMS-TDR-4, 1997.

[52] CMS Collaboration, "The CMS hadron calorimeter project : Technical design report", Technical Report CERN-LHCC-97-031. CMS-TDR-2, 1997.

[53] CMS Collaboration, "The CMS muon project : Technical design report", Technical Report CERN-LHCC-97-032. CMS-TDR-3, 1997.

[54] CMS Collaboration, "Performance of CMS muon reconstruction in pp collision events at $\sqrt{s}$ = 7 TeV", *JINST* **7** (2012) P10002, doi:10.1088/1748-0221/7/10/P10002, arXiv:1206.4071.

[55] CMS Collaboration, "The CMS trigger system", *JINST* **12** (2017) P01020, doi:10.1088/1748-0221/12/01/P01020, arXiv:1609.02366.

[56] GEANT4 Collaboration, "GEANT4—a simulation toolkit", *Nucl. Instrum. Meth. A* **506** (2003) 250, doi:10.1016/S0168-9002(03)01368-8.

[57] CMS Collaboration, "Particle-flow reconstruction and global event description with the CMS detector", *JINST* **12** (2017) P10003, doi:10.1088/1748-0221/12/10/P10003, arXiv:1706.04965.

[58] CMS Collaboration, "Description and performance of track and primary-vertex reconstruction with the CMS tracker", *JINST* **9** (2014) P10009, doi:10.1088/1748-0221/9/10/P10009, arXiv:1405.6569.

[59] Frühwirth, R., "Application of Kalman filtering to track and vertex fitting", *Nucl. Instrum. Meth. A* **262** (1987) 444, doi:10.1016/0168-9002(87)90887-4.

[60] P. Billoir, "Progressive track recognition with a Kalman-like fitting procedure", *Comp. Phys. Comm.* **57** (1989) 390, doi:10.1016/0010-4655(89)90249-X.

[61] P. Billoir and S. Qian, "Simultaneous pattern recognition and track fitting by the Kalman filtering method", *Nucl. Instrum. Meth. A* **294** (1990) 219, doi:10.1016/0168-9002(90)91835-Y.

[62] A. Strandlie and W. Wittek, "Propagation of covariance matrices of track parameters in homogeneous magnetic fields in CMS", CMS Note CMS-NOTE-2006-01, 2006.

[63] CMS Collaboration, "Measurements of Higgs boson properties in the diphoton decay channel in proton-proton collisions at $\sqrt{s} = 13$ TeV", *JHEP* **11** (2018) 185, doi:10.1007/JHEP11(2018)185, arXiv:1804.02716.

[64] CMS Collaboration, "Performance of photon reconstruction and identification with the CMS detector in proton-proton collisions at $\sqrt{s} = 8$ TeV", *JINST* **10** (2015) P08010, doi:10.1088/1748-0221/10/08/P08010, arXiv:1502.02702.

[65] CMS Collaboration, "Energy calibration and resolution of the CMS electromagnetic calorimeter in pp collisions at $\sqrt{s} = 7$ TeV", *JINST* **8** (2013) P09009, doi:10.1088/1748-0221/8/09/P09009, arXiv:1306.2016.

[66] CMS Collaboration, "Electron and photon performance in CMS with the full 2016 data sample", CMS Detector Performance Summary CMS-DP-2017-004, 2017.

[67] M. Cacciari and G. P. Salam, "Pileup subtraction using jet areas", *Phys. Lett. B* **659** (2007) 119, doi:10.1016/j.physletb.2007.09.077, arXiv:0707.1378.

[68] M. Cacciari, G. P. Salam, and G. Soyez, "The anti-k_{T} jet clustering algorithm", *JHEP* **04** (2008) 063, doi:10.1088/1126-6708/2008/04/063, arXiv:0802.1189.

[69] M. Cacciari, G. P. Salam, and G. Soyez, "FastJet user manual", *Eur. Phys. J. C* **72** (2012) 1896, doi:10.1140/epjc/s10052-012-1896-2, arXiv:1111.6097.

[70] CMS Collaboration, "Jet energy scale and resolution in the CMS experiment in pp collisions at 8 TeV", *JINST* **12** (2017) P02014, doi:10.1088/1748-0221/12/02/P02014, arXiv:1607.03663.

[71] CMS Collaboration, "Jet algorithms performance in 13 TeV data", CMS Physics Analysis Summary CMS-PAS-JME-16-003, 2017.

[72] CMS Collaboration, "Performance of missing transverse momentum reconstruction in proton-proton collisions at $\sqrt{s} = 13$ TeV using the CMS detector", *Submitted to JINST* (2019) arXiv:1903.06078.

[73] CMS Collaboration, "Event generator tunes obtained from underlying event and multiparton scattering measurements", *Eur. Phys. J. C* **76** (2016) 155, doi:10.1140/epjc/s10052-016-3988-x, arXiv:1512.00815.

[74] NNPDF Collaboration, "Parton distributions for the LHC run II", *JHEP* **04** (2015) 040, doi:10.1007/JHEP04(2015)040, arXiv:1410.8849.

[75] LHC Higgs Cross Section Working Group, S. Heinemeyer et al., "Handbook of LHC Higgs cross sections: 3. Higgs properties: report of the LHC Higgs cross section working group", CERN Report CERN-2013-004, 2013. doi:10.5170/CERN-2013-004, arXiv:1307.1347.

[76] T. Gleisberg et al., "Event generation with SHERPA 1.1", *JHEP* **02** (2009) 007, doi:10.1088/1126-6708/2009/02/007, arXiv:0811.4622.

[77] CMS Collaboration, "Search for dark matter produced in association with a Higgs boson decaying to two photons", CMS Physics Analysis Summary CMS-PAS-EXO-16-054, 2017.

[78] CMS Collaboration, "Search for dark matter produced in association with a Higgs boson decaying to two photons", CMS Physics Analysis Summary CMS-PAS-EXO-16-011, 2016.

[79] CMS Collaboration, "Measurements of inclusive W and Z cross sections in pp collisions at $\sqrt{s} = 7$ TeV", *JHEP* **01** (2011) 080, doi:10.1007/JHEP01(2011)080, arXiv:1012.2466.

[80] CMS Collaboration, "HIG PAG DPS plots for presentations before Moriond 2016". https://twiki.cern.ch/twiki/bin/view/CMSPublic/HigPagDec2015#Trigger.

[81] G. Punzi, "Sensitivity of searches for new signals and its optimization", (2003). arXiv:physics/0308063.

[82] CMS Collaboration, "Search for dijet resonances in proton-proton collisions at $\sqrt{s} = 13$ TeV and constraints on dark matter and other models", *Phys. Lett. B* **769** (2017) 520, doi:10.1016/j.physletb.2017.02.012, arXiv:1611.03568.

[83] CMS Collaboration, "Search for high-mass diphoton resonances in proton-proton collisions at 13 TeV and combination with 8 TeV search", *Phys. Lett. B* **767** (2017) 147, doi:10.1016/j.physletb.2017.01.027, arXiv:1609.02507.

[84] J. Butterworth et al., "PDF4LHC recommendations for LHC Run II", *J. Phys. G* **43** (2016) 023001, doi:10.1088/0954-3899/43/2/023001, arXiv:1510.03865.

[85] CMS Collaboration, "Measurement of inclusive and differential Higgs boson production cross sections in the diphoton decay channel in proton-proton collisions at $\sqrt{s}$ = 13 TeV", *JHEP* **01** (2019) 183, doi:10.1007/JHEP01(2019)183, arXiv:1807.03825.

[86] CMS Collaboration, "CMS luminosity measurements for the 2016 data taking period", CMS Physics Analysis Summary CMS-PAS-LUM-17-001, 2017.

[87] ATLAS and CMS Collaborations, and the LHC Higgs Combination Group, "Procedure for the LHC Higgs boson search combination in Summer 2011", Technical Report CMS-NOTE-2011-005, ATL-PHYS-PUB-2011-11, 2011.

[88] T. Junk, "Confidence level computation for combining searches with small statistics", *Nucl. Instrum. Meth. A* **434** (1999) 435, doi:10.1016/S0168-9002(99)00498-2, arXiv:hep-ex/9902006.

[89] A. L. Read, "Presentation of search results: the CL_s technique", *J. Phys. G* **28** (2002) 2693, doi:10.1088/0954-3899/28/10/313.

[90] G. Cowan, K. Cranmer, E. Gross, and O. Vitells, "Asymptotic formulae for likelihood-based tests of new physics", *Eur. Phys. J. C* **71** (2011) 1554, doi:10.1140/epjc/s10052-011-1554-0, arXiv:1007.1727. [Erratum: doi:10.1140/epjc/s10052-013-2501-z].

[91] SuperCDMS Collaboration, "New results from the search for low-mass weakly interacting massive particles with the CDMS Low Ionization Threshold Experiment", *Phys. Rev. Lett.* **116** (2016) 071301, doi:10.1103/PhysRevLett.116.071301, arXiv:1509.02448.

[92] LUX Collaboration, "Results from a search for dark matter in the complete LUX exposure", *Phys. Rev. Lett.* **118** (2017) 021303, doi:10.1103/PhysRevLett.118.021303, arXiv:1608.07648.

[93] XENON Collaboration, "First dark matter search results from the XENON1T experiment", *Phys. Rev. Lett.* **119** (2017) 181301, doi:10.1103/PhysRevLett.119.181301, arXiv:1705.06655.

[94] XENON Collaboration, "Dark matter search results from a one ton-year exposure of XENON1T", *Phys. Rev. Lett.* **121** (2018) 111302, doi:10.1103/PhysRevLett.121.111302, arXiv:1805.12562.

[95] PandaX-II Collaboration, "Dark matter results from first 98.7 days of data from the PandaX-II experiment", *Phys. Rev. Lett.* **117** (2016) 121303, doi:10.1103/PhysRevLett.117.121303, arXiv:1607.07400.

[96] PandaX-II Collaboration, "Dark matter results from 54-ton-day exposure of PandaX-II experiment", *Phys. Rev. Lett.* **119** (2017) 181302, doi:10.1103/PhysRevLett.119.181302, arXiv:1708.06917.

[97] CRESST-II Collaboration, "Results on light dark matter particles with a low-threshold CRESST-II detector", *Eur. Phys. J. C* **76** (2016) 25, doi:10.1140/epjc/s10052-016-3877-3, arXiv:1509.01515.

[98] CDEX Collaboration, "Limits on light weakly interacting massive particles from the first 102.8 kg $\times$ day data of the CDEX-10 experiment", *Phys. Rev. Lett.* **120** (2018) 241301, doi:10.1103/PhysRevLett.120.241301, arXiv:1802.09016.

[99] G. Apollinari et al., eds., "High-Luminosity Large Hadron Collider (HL-LHC) Technical Design Report V. 0.1", volume 4/2017 of *CERN Yellow Reports: Monographs*. CERN, 2017. CERN-2017-007-M. doi:10.23731/CYRM-2017-004.

[100] CMS Collaboration, "Technical proposal for the Phase-II upgrade of the CMS detector", Technical Report CERN-LHCC-2015-010. LHCC-P-008. CMS-TDR-15-02, 2015.

[101] CMS Collaboration, "The Phase-2 upgrade of the CMS tracker", Technical Report CERN-LHCC-2017-009. CMS-TDR-014, 2017.

[102] CMS Collaboration, "Technical proposal for a MIP timing detector in the CMS experiment Phase 2 upgrade", Technical Report CERN-LHCC-2017-027. LHCC-P-009, 2017.

[103] CMS Collaboration, "The Phase-2 upgrade of the CMS L1 trigger: Interim technical design report", Technical Report CERN-LHCC-2017-013. CMS-TDR-017, 2017.

[104] E. Bartz et al., "FPGA-based tracklet approach to level-1 track finding at CMS for the HL-LHC", *EPJ Web Conf.* **150** (2017) 00016, doi:10.1051/epjconf/201715000016, arXiv:1706.09225.

[105] E. Bartz et al., "FPGA-based real-time charged particle trajectory reconstruction at the Large Hadron Collider", *FCCM* (2017) 64, doi:10.1109/FCCM.2017.27.

[106] J. Chaves, "Implementation of FPGA-based level-1 tracking at CMS for the HL-LHC", *JINST* **9** (2014) C10038, doi:10.1088/1748-0221/9/10/C10038.

[107] L. Skinnari et al., "FPGA-based approach to level-1 track finding at CMS for the HL-LHC", *EPJ Web Conf.* **127** (2016) 00017, doi:10.1051/epjconf/201612700017.

[108] R. Aggleton et al., "An FPGA based track finder for the L1 trigger of the CMS experiment at the High Luminosity LHC", *JINST* **12** (2017) P12019, doi:10.1088/1748-0221/12/12/P12019.

[109] G. Fedi et al., "Associative memory pattern matching for the L1 track trigger of CMS at the HL-LHC", *EPJ Web Conf.* **127** (2016) 00008, doi:10.1051/epjconf/201612700008.

[110] Z. Tao et al., "Level-1 track finding with an all-FPGA system at CMS for the HL-LHC", *Submitted to EPJ Web Conf.* (2019) arXiv:1901.03745.

[111] CMS Collaboration, "First level track jet trigger for displaced jets at High Luminosity LHC", CMS Physics Analysis Summary CMS-PAS-FTR-18-018, 2018.

[112] Y. Gershtein, "CMS hardware track trigger: New opportunities for long-lived particle searches at the HL-LHC", *Phys. Rev. D* **96** (2017) 035027, doi:10.1103/PhysRevD.96.035027, arXiv:1705.04321.

[113] CMS Collaboration, "CMS Phase II upgrade scope document", Technical Report CERN-LHCC-2015-019. LHCC-G-165, 2015.

[114] PICMG, "MicroTCA overview". https://www.picmg.org/openstandards/microtca.

[115] A. Svetek et al., "The Calorimeter Trigger Processor Card: the next generation of high speed algorithmic data processing at CMS", *JINST* **11** (2016) C02011, doi:10.1088/1748-0221/11/02/C02011.

[116] Xilinx, "7 Series FPGAs data sheet: overview, DS180 (v2.6)". https://www.xilinx.com/support/documentation/data_sheets/ds180_7Series_Overview.pdf, 2018.

[117] Xilinx, "Zynq-7000 SoC data sheet: overview, DS190 (v1.11.1)". https://www.xilinx.com/support/documentation/data_sheets/ds190-Zynq-7000-Overview.pdf, 2018.

[118] Boston University, "AMC13". http://www.amc13.info.

[119] PICMG, "AdvancedTCA overview". https://www.picmg.org/openstandards/advancedtca.

[120] Xilinx, "UltraScale architecture and product data sheet: overview, DS890 (v3.7)". https://www.xilinx.com/support/documentation/data_sheets/ds890-ultrascale-overview.pdf, 2019.

[121] Enclustra, "Mars ZX2". https://www.enclustra.com/en/products/system-on-chip-modules/mars-zx2/.

[122] Samtec, "Firefly application design guide". http://suddendocs.samtec.com/ebrochures/firefly-brochure.pdf, 2019.

[123] SFF Committee, "SFF-8679 Specification for QSFP28 4X base electrical specification (v1.7)". https://doc.xdevs.com/doc/Seagate/SFF-8679.PDF, 2014.

[124] Xilinx, "In-System IBERT PG246 v1.0". https://www.xilinx.com/support/documentation/ip_documentation/in_system_ibert/v1_0/pg246-in-system-ibert.pdf, 2017.